**UQAC**

Université du Québec
à Chicoutimi

**The use of trace elements in pyrite and carbonates as a petrogenetic and**

**exploration tool for carbonate-bearing Archean VMS: example from B26, Abitibi,**

**Canada**

**Contenu en éléments traces dans les pyrites et les carbonates comme outil**

**pétrogénétique et d'exploration pour les SMV archéens à carbonates : exemple de**

**B26, Abitibi, Canada**

**Par**

**Rémi Naulot**

**Sous la direction de Sarah Dare et Dominique Genna**

**Mémoire présenté à l'Université du Québec à Chicoutimi en vue de l'obtention du grade de**

**Maitre ès sciences appliquées (MSc. A.) en Géologie et Génie Géologique**

Québec, Canada

**RÉSUMÉ**

Les gisements de sulfures massifs volcanogènes (SMV) sont des gisements polymétalliques représentant une source importante de métaux précieux (Au, Ag) et stratégiques (Cu, Zn, Pb). Ils présentent un large halo d'altération, composé dans certains cas de chlorite-séricite (SMV de type-Noranda), dont la zonalité est couramment utilisée comme outil d'exploration. Dans certains cas, une carbonatation s'ajoute à cet assemblage d'altération classique (SMV de type-Mattabi), mais l'origine de ces carbonates est encore débattue et le potentiel de leur signature chimique comme vecteur d'exploration sont actuellement inconnus. Le gîte B26, situé dans le camp minier de Selbaie (ceinture de roches vertes de l'Abitibi, Québec, Canada) est un exemple de SMV de type-Mattabi. La minéralisation y est spatialement associée à une altération carbonatée stratoïde étendue dans des tufs rhyolitiques et métamorphisés au faciès des schistes verts. L'altération carbonatée est continue sur plusieurs kilomètres et suit des unités volcanoclastiques felsiques poreuses. Cette étude s'est concentrée sur deux transects : B26 et ses environs (<1km), et B26 Ouest, 3 à 6km à l'ouest, dans la continuité des unités felsiques mais sans indices majeurs découverts.

Les observations texturales, la lithogéochimie et la chimie minérale des carbonates, de la pyrite et de la sphalérite ont été étudiés, dans un premier temps, afin de mieux comprendre l'origine et la formation de l'altération carbonatée stratoïde à B26. Dans un second temps, cette étude a démontré le potentiel de la chimie minérale combinée de ces trois phases minérales, et en particulier leur contenu en éléments traces, en tant qu'outil d'exploration pour les gisements de SMV de type-Mattabi. Un échantillonnage systématique du toit de la minéralisation, unité la plus intensément carbonatée, a été réalisé pour 1) caractériser l'altération en carbonates, 2) déterminer sa relation avec la minéralisation de B26 et 3) documenter l'évolution de la signature géochimique des différents minéraux présents dans les unités carbonatées en fonction de la distance aux minéralisations.

La lithogéochimie a été utilisée pour documenter les zonalités présentes dans le halo d'altération carbonaté. Le mur de la minéralisation, dominé par la séricite et la chlorite, est intensivement lessivé. La carbonatation est importante dans le toit, le long des unités les plus poreuses, et continue sur plus de 10 km. L'altération carbonatée est typique des gisements de SMV de type Mattabi, avec de la sidérite près des zones minéralisées, entouré par un halo d'ankérite proximale et de calcite distale. Les carbonates sont systématiquement associés à d'autres minéraux d'altération typiques des SMV (chlorite-séricite-pyrite).

La chimie minérale sur les carbonates a aussi été utilisée comme outil pétrogénétique pour contraindre l'origine des fluides impliqués dans la formation de l'altération en carbonates. Les spectres d'éléments de terres rares (ETR) et Y permettent de distinguer trois types de carbonates (types 1, 2 et 3). Les carbonates de type 1 sont caractérisés par une anomalie négative en Eu et sont situés près des minéralisations. Cette signature est inhabituelle pour les SMV, cependant, elle a déjà été observée dans des fluides magmatiques, des caldeiras subaériennes et des évents hydrothermaux subaériens. Elle a donc été interprétée comme étant le reflet d'une contribution de fluides hydrothermaux-magmatiques liés au dégazage d'une intrusion synvolcanique sous-jacente. Les carbonates de type 2 présentent une anomalie positive en Eu et sont les plus abondants à B26, présents dans les zones à Zn secondaires de B26 et dans les unités carbonatées proximales et intermédiaires. Cette signature a déjà été documentée dans d'autres gisements SMV et a été associée aux fluides hydrothermaux classiques de gisements SMV (c'est-à-dire à de l'eau de mer modifiée). Enfin, les carbonates de type 3 présentent un spectre d'ETR+Y concave, avec un appauvrissement en terres rares légères et une anomalie positive en La. Ils sont particulièrement présents dans le transect B26 Ouest. Le profil concave ressemble à celui des carbonates formés au

cours de la diagenèse, dans les pores des tufs volcaniques saturés d'eau de mer, avec peu d'influence volcanogène.

Les éléments traces de la pyrite ont également été utilisés comme outil pétrogénétique pour confirmer l'origine volcanogène des unités carbonatées à B26 et diagénétique du transect B26 Ouest. La pyrite présente dans la minéralisation est systématiquement enrichie en Co, Se, Ag, Tl, et les concentrations en ces éléments diminuent progressivement en s'éloignant des minéralisations, mettant en avant plusieurs vecteurs potentiels. La combinaison de la chimie minérale des carbonates et de la pyrite montre que les unités altérées en carbonates présentent une signature volcanogène continue tout au long du transect B26. Ces carbonates volcanogènes ont été formés par le dégazage de l'intrusion synvolcanique de Brouillan, par l'exsolution de fluides riches en $CO_2$ s'écoulant à travers les structures synvolcaniques actives et le long des unités volcanoclastiques poreuses, formant une altération carbonatée stratoïde de type Mattabi. Sur le transect B26 Ouest, la présence de carbonates de type 3 (diagenétiques) combinés à des pyrites riches en Mn et en V suggère une domination de l'eau de mer dans la formation des altérations en carbonates, avec une composante hydrothermale mineure. Les carbonates se sont formés à partir de l'eau de mer piégée dans les pores des unités volcanoclastiques. Cette étude montre que la chimie minérale et l'étude des éléments traces des carbonates et de la pyrite est un outil puissant pour aider à déterminer l'origine de l'altération des carbonates dans les gisements de SMV et peut être utilisée pour l'exploration de ces gisements.

# ABSTRACT

Volcanogenic massive sulfide deposits (VMS) are major polymetallic deposits, and important sources of precious (Au, Ag) and strategic metals (Cu, Zn, Pb). They display a wide alteration halo, composed of chlorite-sericite (Noranda-type deposits), which zoning is commonly used in exploration. In some cases, some VMS also display a carbonatation in addition to this classic assemblage   (i.e. Mattabi-type deposits) but the origin of the carbonates is still debated, and whether carbonate trace elements chemistry can be used in exploration, is currently unknown. The B26 prospect in the Selbaie mining camp (Abitibi greenstone belt, Québec, Canada) is an example of Mattabi-type VMS. Mineralization is spatially associated with widespread stratabound carbonate alteration hosted in rhyolitic tuffs and metamorphosed to greenschist facies. The carbonate alteration is continuous over several kilometers following preferentially porous felsic volcaniclastic units. This study focused on two transects: B26 and its surrounding area (<1km), and B26 West, 3 to 6km West along the same felsic units but with no major discovered showings.

Textural observations, lithogeochemistry and in situ trace element chemistry of carbonates, pyrite, and sphalerite were studied, in one hand, in order to better understand the formation of the semi-conformable carbonate alteration at B26. In the other hand, the potential of combining mineral chemistry of these three species as an exploration tool for Mattabi-type VMS deposits was discussed. Systematic sampling of the carbonated hanging-wall was carried out to 1) characterize the carbonate alteration, 2) determine its relationship with the VMS mineralization, and 3) document the evolution of the geochemical signature of the minerals present within the carbonate-altered units with distance to B26.

Lithogeochemistry was used to document the zonation in the carbonate alteration halo. The footwall, dominated by sericite and chlorite, is intensively leached. Carbonatation is important in the hanging-wall along the most porous units, and continuous over 10km along strike. The carbonate alteration is typical of Mattabi-type VMS deposits with siderite in and around the mineralized zones, surrounded by proximal ankerite and distal calcite. Carbonates are systematically associated with other typical VMS alteration minerals (chlorite-sericite-pyrite).

Trace element geochemistry of carbonate was also developed as a petrogenetic tool to constrain the origin of the fluids involved in the formation of the carbonate alteration. The rare earth elements (REE) and Y patterns differentiate three types of carbonates (Type 1, 2 and 3). Type 1 carbonates are characterized by a negative Eu anomaly and are located within the mineralized ore shell. This signature is unusual for VMS environments, but it was documented in magmatic fluids and subaerial calderas and hydrothermal vents. Thus, it was interpreted to reflect a hydrothermal-magmatic fluid contribution related to the degassing of the underlying subvolcanic intrusion. Type 2 carbonates display a positive Eu anomaly and are the most abundant in B26 upper mineralization and proximal to intermediate carbonate-altered units. This REE signature has already been documented in other VMS deposits and was related to VMS hydrothermal fluids (i.e. modified seawater). Lastly, type 3 carbonates have a concave REE+Y pattern, with a depletion of light rare earth elements (LREE) and positive La anomaly. They are mostly found in the B26 West transect. The concave pattern resembles that of interstitial carbonates formed during diagenesis, thus formed in the pores of volcanic tuffs saturated with seawater distal from the VMS system.

Pyrite trace elements was also used as a petrogenetic tool to confirm the origin of the carbonate-altered units as volcanogenic for B26 transect and dominantly diagenetic for B26 West. Pyrite from the mineralization is systematically enriched in Co, Se, Ag, Tl and their progressive decrease in pyrite,

from the carbonate-altered units with distance, highlights several potential vectoring tools using pyrite. The combination of carbonate and pyrite trace elements shows that there is a continuous volcanogenic signature of the carbonate-altered units all along the B26 transect. These volcanogenic carbonates were formed by the degassing of the underlying Brouillan Intrusive Complex, with $CO_2$-rich fluids flowing through active synvolcanic structures and along the most porous units, forming Mattabi-type stratabound carbonate alteration. On the B26 West transect, the presence of type 3 (diagenetic) carbonates combined with Mn and V-rich pyrite suggests that seawater was dominant during the formation of carbonate-altered units. The hydrothermal fluid, if present, was highly diluted. Carbonates formed from trapped seawater in the pores of the volcaniclastic units. This study shows that trace elements in carbonate and pyrite are a powerful tool to help determine the origin of carbonate alteration of VMS deposits and can be used for exploration for these deposits.

# TABLE OF CONTENT

# LIST OF FIGURES

.

# LIST OF ANNEXES

**S1** : Location and description of samples

**S2**: Analytical protocols of lithogeochemical analyses with corresponding limits of detection

**S3** : QA-QC of whole-rock geochemistry (CDN ME-1414; OREAS 920)

**S4** : QA-QC of carbonate by LA-ICP-MS (MACS3; NIST 610; GSE; G Probe 4; NIST 616)

**S5** : Comparison of carbonate major elements using LA-ICP-MS (this study) and electron microprobe (Lafrance, 2003) from Normétal

**S6** : QA-QC of pyrite by LA-ICP-MS (MASS 1; GSE; UQAC FeS1; UQAC FeS5)

**S7** : QA-QC of sphalerite by LA-ICP-MS (MASS 1; GSE; UQAC FeS1; UQAC FeS5)

**S8** : Whole-rock geochemical data

**S9** : LA-ICP-MS analyses of carbonate

**S10** : LA-ICP-MS analyses of pyrite

**S11** : LA-ICP-MS analyses of sphalerite from B26 and temperature calculations

**S12** : Pearson Correlation matrix for whole-rock geochemistry and normative carbonate

# LIST OF ABBREVIATIONS

ASP: Archean Sedimentary Pyrite

Cb: Carbonate

Ccp: Chalcopyrite

CCPI: Chlorite-Carbonate-Pyrite Index

CDI: Carbonate Discrimination Index

Chl: Chlorite

CN: Chondrite-normalized

CONSOREM: Consortium de recherche en exploration minérale

CSI: Carbonate saturation Index

FW: Footwall

GGIMFis: Ga, Ge, In, Mn, Fe in sphalerite

Gn: Galena

HW: Hanging-wall

HREE: Heavy Rare Earth Elements

ICP-AES: induced-coupled plasma atomic emission spectroscopy

LabMaTer: Laboratoire des matériaux terrestres

LA-ICP-MS: Laser-ablation induced-coupled plasma mass spectrometry

LOD: Limit of Detection

LOI: Loss on ignition

LREE: Light Rare Earth Elements

Mgt: Magnetite

PAAS: Post-Archean Australian Shale

Po: Pyrrhotite

Py: Pyrite

QA-QC: Quality Assurance-Quality Control

QFP: Quartz-Feldspar porphyry

Qz: Quartz

REE: Rare-Earth Elements

Ser: Sericite

SIGEOM: Système d'information géominière du Québec

Sp: Sphalerite

SOQUEM: Société québécoise d'exploration minière

T°: Temperature

UQAC: Université du Québec à Chicoutimi

UQAM: Université du Québec à Montréal

VMS: Volcanogenic Massive Sulfide

µXRF: Micro X-ray fluorescence

# REMERCIEMENTS

# AVANT-PROPOS

Le secteur de Selbaie fait l'objet de travaux d'exploration depuis les années 1970 avec la découverte de la caldeira de Selbaie par anomalie magnétique, puis du gisement Les Mines Selbaie qui fut en exploitation jusqu'au début des années 2000. L'épaisse couche de mort-terrain rend l'exploration particulièrement compliquée dans la région. Actuellement, la seule autre minéralisation majeure connue dans le secteur est le gîte de B26, découvert puis travaillé par SOQUEM (Société Québécoise d'exploration minière). D'autres indices de métaux de base, mineurs et peu travaillés avant cette étude, sont aussi connus principalement le long de l'horizon de B26 (B26 Ouest, Des Rivières), et de Selbaie (Zones Argent 1, 2 et 3, Selbaie Ouest, Detour-Selbaie), confirmant le potentiel de la caldeira de Selbaie pour ce type de minéralisations. Le gîte de B26 a été décrit en détail lors de la maitrise de Quentin Fayard qui a mis en évidence la présence d'unités fortement carbonatées et notamment des brèches à carbonates de fer présentes à B26, mais aussi dans le reste du camp de Selbaie (Fayard, 2020; Fayard et al., 2020a, b). Dans le but de développer de nouveaux vecteurs d'exploration, SOQUEM a proposé un stage de recherche à l'été 2021, en collaboration avec Dominique Genna, sur l'origine de ces unités, leur lien avec les minéralisations et leur potentiel d'exploration, en utilisant la chimie minérale (pyrite, carbonates). J'ai réalisé ce stage à la fin de ma maitrise professionnelle et ces premiers travaux ont mis en évidence un probable lien entre les brèches à carbonates de fer et les minéralisations volcanogènes du camp de Selbaie ainsi qu'un potentiel pour l'exploration. Nous avons donc proposé à SOQUEM de continuer à étudier le sujet au cours d'une maitrise afin de tester les hypothèses soulevées pendant le stage et d'étoffer les premières conclusions. Cette proposition fut acceptée par SOQUEM et donna lieu à cette maitrise qui s'inscrit ainsi dans l'effort d'exploration de la compagnie dans la caldeira de Selbaie, notamment sur les propriétés de Wagosic, et Carheil.

# CHAPTER 1

# INTRODUCTION

Volcanogenic massive sulfide deposits (VMS) are a significant source of base (Cu, Zn, Pb) and precious metals (Au, Ag), with also important resources in many metals listed as critical and strategic (Natural Resources Canada, 2022). With the growing need for these metals, developing new exploration tools is essential. Exploration for VMS deposits has always been a challenge, because of the difference between the large size of the wide, plurikilometric chlorite-sericite-(carbonate) alteration halo relative to the mineralization (10s to 100s m; Galley et al., 2007; Gibson et al., 2007). It is particularly important to develop precise vectoring tools, adapted to the characteristics of these mineralizations. For VMS deposits, traditional large-scale exploration consists of geophysical surveys in order to target magnetic or electromagnetic anomalies due to the abundance of sulfides (chalcopyrite, pyrrhotite, pyrite; Ford et al., 2007; Gibson et al., 2007). Lithogeochemistry is also widely used at all stages of VMS exploration. Initially, works were mostly based on the use of major elements (Ishikawa et al., 1976; Spitz and Darling, 1978), then minor and trace elements (Barrett and MacLean, 1999; Trépanier et al., 2015) and more recently the semi-volatile metals (Large et al., 2001a; Genna et Gaboury, 2019). Advances in laser ablation-inductively coupled plasma-mass spectrometry (LA-ICP-MS) analyses allow more studies to focus on mineral chemistry with increasing quality and improved detection limits (Cook et al., 2016). In particular, the trace element chemistry of alteration minerals in VMS systems, such as phyllosilicates; (Soltani-Dehnavi et al., 2019) and sulfides (pyrite, Huston et al., 1995; Genna et Gaboury, 2015; Soltani-Dehnavi et al., 2018), have proven their potential as petrogenetic tools with potential to help vector towards VMS mineralization.

Morton and Franklin (1987) described two types of VMS deposits in Archean greenstone belts, based on their alteration: 1) Noranda-type, displaying a typical VMS alteration halo dominated by proximal chlorite and more distal sericite and, 2) Mattabi-type, displaying a carbonatation in addition to the usual Noranda-type alteration assemblage. Classic Canadian examples of Mattabi-type VMS

deposits are Mattabi (Wabigoon greenstone belt, Ontario, Franklin et al., 1975; Morton and Franklin, 1987; Groves et al., 1988) and Normétal (Abitibi greenstone belt, Québec, Lafrance et al., 2000; Lafrance, 2003). This classification is nowadays rarely used, due to the more recent classification of Franklin et al. (2005) based on the VMS host-rock composition. However, abundant stratabound carbonate alteration has been documented in major deposits in Canada (Kidd Creek, Abitibi, Ontario - Schandl and Wicks, 1993; Koopman et al., 1999; Wolverine, Bradshaw et al., 2008; ABM, Finlayson Lake District, Yukon - Denisová and Piercey, 2023) and worldwide, notably in Australia (Rosebery - Large et al., 2001; Thalanga - Herrmann and Hill, 2001; Paulick et al., 2001); Spain (Tharsis - Conde et al., 2021), China (Honghai - Mao et al., 2019; Deng et al., 2020) and Sweden (Kristineberg - Hannington et al., 2003; Barrett et al., 2005). Mattabi-type deposits are described as related to shallow seawater volatile-rich volcanism, with dominant felsic units. Carbonate alteration is semi-conformable, replacing the most porous units (Morton and Franklin, 1987; Lafrance, 2003) and can extend up to several kilometers away from the mineralization (Lafrance, 2003). A zonation is documented in this alteration halo with siderite ($FeCO_3$) around the mineralization, surrounded by a Fe-ankerite to Fe-dolomite ($Ca((Fe,Mg)CO_3)_2$) halo, and distal calcite ($CaCO_3$; Morton and Franklin, 1987; Lafrance, 2003; Mueller et al., 2008). This zonation can be used for large-scale exploration, but few methods exist to vector precisely within this carbonate alteration (Lafrance, 2003). The geometry and zonation of this carbonatation suggest a hydrothermal origin, linked to the VMS formation (Lafrance, 2003; Mueller et al., 2008). However, carbonates in Archean greenstone belts can have many other origins: metamorphic (Veizer et al., 1989a; Groves et al., 1998; Goldfarb and Groves, 2015), biogenic, including the presence of stromatolites (Hofmann and Masson, 1994; Van Kranendonk et al., 2003; Allwood et al., 2010; Khelen et al., 2019), or diagenetic (Veizer et al., 1989b; Rouchon et al., 2009).

Very few studies have characterized in detail trace elements in carbonates from Archean volcanogenic systems (Matagami district, Abitibi, Québec, Genna et al., 2015), furthermore, it has never been used as a potential exploration tool. A few studies on modern seafloor hydrothermal systems have documented the chemistry of the fluids (Klinkhammer et al., 1994; Mitra et al., 1994;

Mills and Elderfield, 1995; Bau and Dulski, 1999; Craddock et al., 2012) and the carbonate minerals (Eickmann et al., 2009) in present-day hydrothermal vents and black smoker chimneys. Other authors give insights for the use of carbonate as petrogenetic tools, such as using the Y/Ho ratio as a proxy for the seawater influence on the formation of carbonates (Bau, 1996; Nozaki et al., 1997; Bau and Dulski, 1999; Bohlar et al., 2004; Allwood et al., 2010).

On the other hand, pyrite chemistry has already been successfully used as a petrogenetic and exploration tool for ancient and modern seafloor hydrothermal systems (TAG - Grant et al., 2018), including classic Noranda-type VMS deposits, such as Yaman-Kasy, Southern Urals, Russia (Maslennikov et al., 2009), several Canadian deposits from the Abitibi greenstone belt (Noranda district -Sharman et al., 2015; Bracemac McLeod- Genna and Gaboury, 2015), the Bathurst mining camp (Soltani-Dehnavi et al., 2018) and from the Iberian Pyrite Belt, Spain and Portugal (González-Jiménez et al., 2022). Pyrite can record changes in fluid chemistry and temperature during the evolution of the hydrothermal system, thus it can help understand the conditions of formation of mineralization and associated alteration (Large et al., 2007; Genna et Gaboury, 2015).

This study aims to understand better the formation of Mattabi-type carbonatation using trace elements in carbonate and pyrite in order to evaluate the potential of this carbonate alteration for VMS exploration. For this study, the B26 VMS prospect, in the Selbaie mining camp (Abitibi greenstone belt, Québec, Canada) is an ideal case study. The area of the former Selbaie mine is known for extensive carbonate alteration associated with the volcanogenic mineralization and synvolcanic structures (Piché and Jébrak, 2006; Faure, 2012). Recent work from Fayard (2020) has studied in detail the geological context of the B26 project and its mineralization, which is by replacement of felsic volcaniclastic units. Furthermore, its association with carbonate alteration makes it a potential Mattabi-type deposit. Using a combination of textural observations with polished thin sections and micro-X-ray fluorescence (µXRF) maps, lithogeochemistry and mineral chemistry on carbonate, pyrite and sphalerite, this study shows that the carbonate alteration surrounding the B26 VMS is effectively

synvolcanic in origin, formed by a dominant proximal hydrothermal-magmatic fluid which is progressively diluted by modified seawater. It also shows that the most distal carbonated units are not linked to the B26 VMS system and are mostly formed by seawater during diagenesis. Finally, it confirms that pyrite trace elements are tracers of the evolution of the hydrothermal system and can be used as an exploration tool for VMS deposits.

# CHAPTER 2

# GEOLOGICAL BACKGROUND

## 2.1 Regional geology of the Selbaie mining camp

The Selbaie mining camp is located in the northern part of the Archean Abitibi greenstone belt, in Québec, Canada (Figure 2.1a). It is best known for the former mine of Les Mines Selbaie, a Zn-Cu-Au-Ag epithermal-VMS deposit (Sinclair, 1977; Faure et al., 1996) and several VMS showings, including the B26 project (Fayard, 2020). The Selbaie mining camp is hosted in the Brouillan Intrusive Complex and the Brouillan Volcanic Complex. Detailed geological descriptions of the Selbaie mining camp are given in Lacroix (1994), Taner (2000) and Faure (2012) from which the following is summarized. The Brouillan Intrusive Complex is a polyphase synvolcanic intrusion with predominant calc-alkaline felsic to intermediate phases and a minor tholeiitic mafic phase (Lacroix, 1994; Faure, 2012). The tonalitic phase was dated at 2729 ± 4 Ma using U-Pb on zircon (Barrie and Krogh, 1996). The Brouillan Volcanic Complex, coeval and cogenetic to the Brouillan Intrusive Complex, is composed mainly of andesitic to rhyolitic volcaniclastic units, with occurrences of andesitic lava flows and rhyolitic domes (Lacroix, 1994). The Brouillan Intrusive Complex and Brouillan Volcanic Complex form together a large caldera, centered around the Brouillan pluton (Larson and Hutchinson, 1993; Taner, 2000; Faure, 2012). The synvolcanic Brouillan Intrusive Complex is interpreted as the heat source of the volcanic-related mineralization (VMS and epithermal) in the Selbaie camp (Larson and Hutchinson, 1993; Taner, 2000; Fayard, 2020).

The units of Les Mines Selbaie were dated using U-Pb on zircon by Barrie and Krogh (1996). They dated a flow-banded rhyolite at 2729 +3/-2 Ga, which they interpreted as similar in age as the VMS-type mineralization, and a felsic dyke at 2726 ± 3 Ga, which crosscuts the early VMS lenses and is cross-cut by the late epithermal veins. All the units of the Selbaie mining camp are metamorphosed to the greenschist facies (Lacroix, 1994; Fayard, 2020). In general, the units in Selbaie show

moderate deformation, except on the interpreted southern borders of the Selbaie caldera, especially along the contact between the Brouillan Volcanic Complex and the Enjalran-Bapst Group (Figure 2.1; Lacroix, 1994; Taner, 2000; Fayard, 2020).

Another characteristic of the Selbaie camp is the ubiquitous presence of carbonates. Piché and Jébrak (2006) and Faure (2012) highlight the abundance of carbonates in the Selbaie camp (Annex 1), using respectively NORMAT normative mineral alteration index from Piché and Jébrak (2004) and the Alt_Carb_SV350 index from Trépanier (2013). These methods illustrate the importance of carbonate alteration in the Selbaie mining camp as observed petrographically in the samples (Figures 2.2, 2.3). The carbonatation is particularly intense around Selbaie and B26 mineralizations, and along interpreted synvolcanic faults (Faure, 2012; Annex 1). However, despite the intensity of the carbonatation, its origin has not been interpreted yet. Indeed, in Archean greenstone belts, carbonate can have many origins: sedimentary (biogenic or diagenetic; Veizer et al., 1989b; Hofmann and Masson, 1994), metamorphic (Veizer et al., 1989a; Groves et al., 1998) or volcanogenic, related to Mattabi-type VMS (Morton and Franklin, 1987; Lafrance, 2003; Mueller et al., 2008).

## 2.2   Geology of the B26 prospect

The B26 project is located 5km south of Les Mines Selbaie, at the southern limb of the Brouillan Volcanic Complex and close to the contact with the overlaying Enjalran-Bapst group (Figure 2.1; Fayard et al., 2020a). The resources of B26 are estimated at 11.4 Mt at 1.52% Cu, 1.19% Zn, 0.78 g/t Au and 30 g/t Ag (indicated and inferred, Camus and Vadnais-Leblanc, 2018). The mineralization and local geology have been described in detail by Fayard (2020) using a combination of drill core description, whole-rock geochemistry and mineral chemistry of pyrite. The following is summarised from Fayard (2020). Three rhyolitic units of the Felsic member were distinguished in B26 using immobile elements : 1) rhyolite A has high $Zr/TiO_2$ (>2500) and $Al_2O_3/TiO_2$ (>100) ratios, 2) rhyolite B has a low $Zr/TiO_2$ (1000 to 2000) ratio and a moderate $Al_2O_3/TiO_2$ (75 to 120) ratio and 3) rhyolite

C has low Zr/TiO$_2$ (<1500) and Al$_2$O$_3$/TiO$_2$ (25 to 60) ratios. The mineralization is hosted in rhyolitic tuffs (Rhyolite A) where it is interpreted to have formed by replacement of these porous felsic units (Figure 2.1b; Fayard et al., 2020a). All the Felsic members have a similar calc-alkaline affinity and are part of the same magmatic system; rhyolites A and B were dated at 2728 ± 1 Ma (Fayard et al., 2020a). Rhyolite A was interpreted as a rhyolitic dome or flow-dome complex with a large proportion of related volcaniclastic units. Rhyolites B and C are composed of quartz(-feldspar) porphyry-bearing units. Rhyolite B is a group of cryptodomes and sills that are contemporaneous with the emplacement of rhyolite A. Rhyolite C is the uppermost unit at B26, it overlies rhyolite A and shows little alteration.

## 2.2.1 Mineralization

Together, the mineralized zones are up to 75m thick with an E-W extension of 2km and 1km deep (Fayard, 2020). The B26 mineralization is separated into three main zones (Fayard et al., 2020b): 1) The Cu-zone is characterized by unconformable chalcopyrite-dominated stringers and disseminations and represents the feeder zone of the VMS, with local *durchbewegung* texture (Figure 2.2a), indicating an intense deformation of the ore zone (Marshall and Gilligan, 1989). It is hosted in the footwall (Rhyolite A). 2) The main Zn-zone comprises two main semi-massive to massive sulfide lenses, which are mostly sphalerite-rich (Figure 2.2b). It is located at the contact between the footwall and hanging-wall. 3) The upper Zn-zones are small sphalerite-rich disseminations in the hanging-wall (Rhyolite A; Figure 2.2c) of the main Zn-zone. The main and upper Zn-zones display a variation of mineralization styles with 1) semi-massive to massive sulfide lenses (Figure 2.2b); 2) dissemination (Figure 2.2c); 3) veins and stringers; and 4) Ag-rich veins and veinlets (Fayard et al., 2020b). The B26 prospect was emplaced directly along a synvolcanic fault, interpreted to be the southern border of the Selbaie caldera (Faure, 2012; Fayard, 2020). Later regional N-S shortening led to a stretching and a flattening of both the mineralization and the host units, resulting in a parallelization of the stratigraphy and the discordant mineralization. The E-W stretching along the southern border of the caldera dismembered both Cu and Zn-zones (Fayard, 2020).

## 2.2.2   Alteration

Several alteration assemblages were described by Fayard et al. (2020b) for B26. A chlorite-sericite assemblage mostly occurs in the proximal zones, around the mineralization of the Cu-zone and the main Zn-zone. It corresponds to the most altered rocks of B26. The footwall is characterized by an increase of sericite over chlorite with distance from the deposit. This chlorite-sericite alteration assemblage is continuous for more than 1km along strike and has a thickness of about 300m below the mineralization. Silicification is also present in the hanging-wall overlying the main Zn-zone. The hanging-wall is intensely altered with an alteration assemblage dominated by carbonates, sericite, and chlorite with minor albite and K-feldspars. Carbonate alteration is present throughout the deposit and in most of the alteration assemblages (Fayard, 2020; Figure 2.2d-f), but has not been systematically mapped or studied in detail. Field observations can only distinguish between white calcite and orange to brownish Fe-carbonates.

## 2.2.3   Carbonatation

In and around B26, carbonate alteration is stratabound in the rhyolitic tuffs (rhyolite A) replacing its most porous layers. Iron-carbonates are dominant in the mineralized zones, in meter-thick horizons in the hanging-wall (Figure 2.2c-e; 2.3a-c) and in ankerite-magnetite-biotite breccias located above the mineralization (Figure 2.2f). Calcite is disseminated in the upper, least-altered volcaniclastic units, and in late veins. These textures are observed in the most distal zones. More intense alteration occurs as a replacement of the host rock matrix and/or the lapilli, with up to 70% of alteration minerals, including 40% carbonates (Figure 2.2e-f; 2.3c, d). The intensity of alteration and the proportion of alteration minerals, including carbonates, increase towards the Cu and Zn mineralization. The most intensely carbonate-altered horizon in B26 is the hanging-wall of the main Zn-zone, with a carbonate-(± chlorite ± sericite) assemblage. In certain cases, there is a brecciation of the host rock (Figure 2.2f). Low-intensity alteration textures consist of scarce dissemination or veinlets of carbonate

associated with other alteration minerals, most commonly sericite, chlorite, and pyrite (Figure 2.3). It is frequently observed that there are some cross-cutting relationships between carbonate-pyrite-(± chlorite ± sericite) veins or veinlets and other carbonate-bearing alteration phases (Figure 2.2d), indicating a long-lasting hydrothermal system, possibly due to zone-refining (Eldridge et al., 1983).
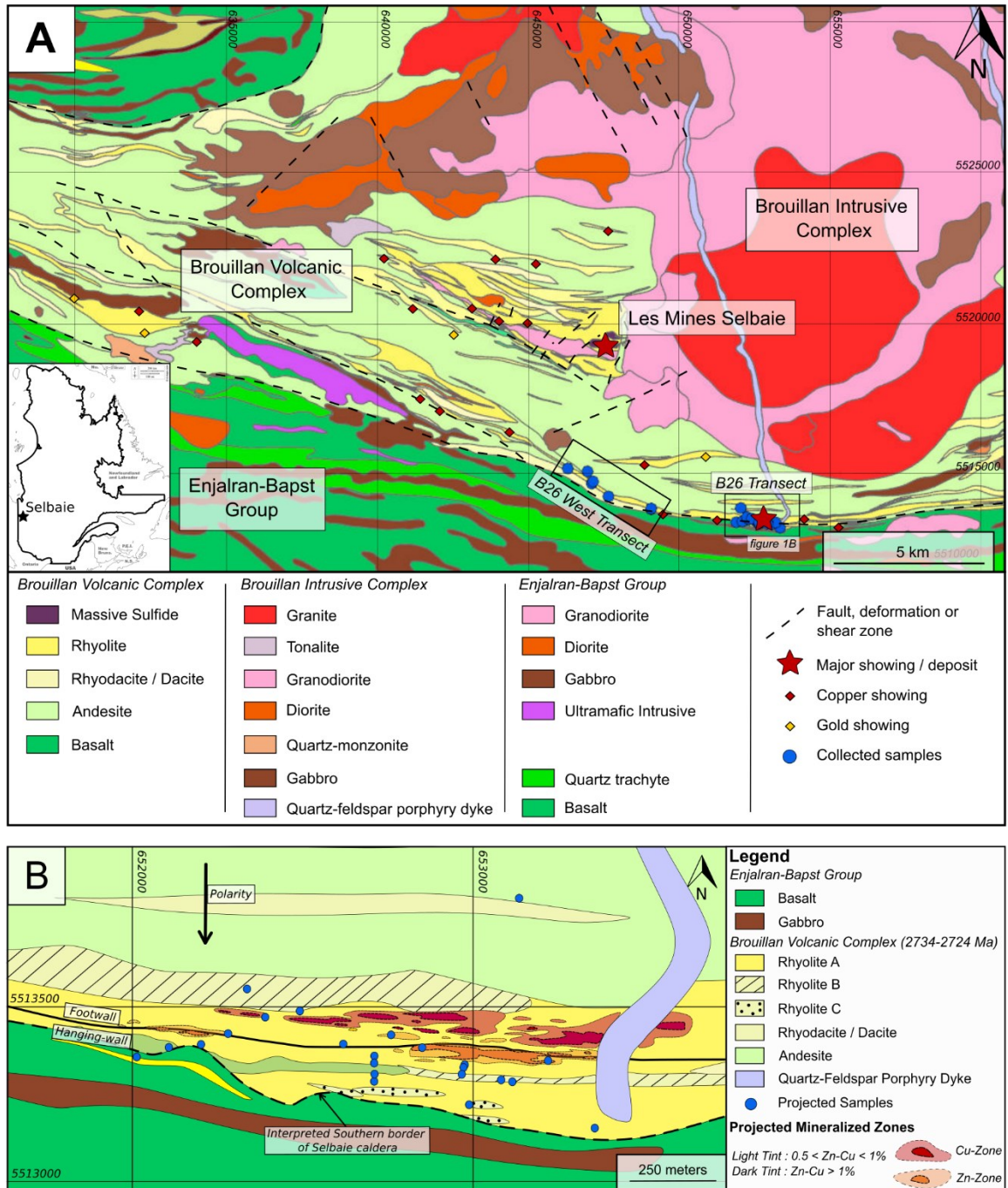
Figure 2.1: A. Geological map of the Selbaie mining camp (Geology from CONSOREM and SIGEOM; modified from Lacroix, 1994); B. Detailed geology of the B26 transect, showing the location of the mineralization and the collected samples (modified from Fayard, 2020). The black line corresponds to the projected limit between the footwall and the hanging wall of the mineralization.
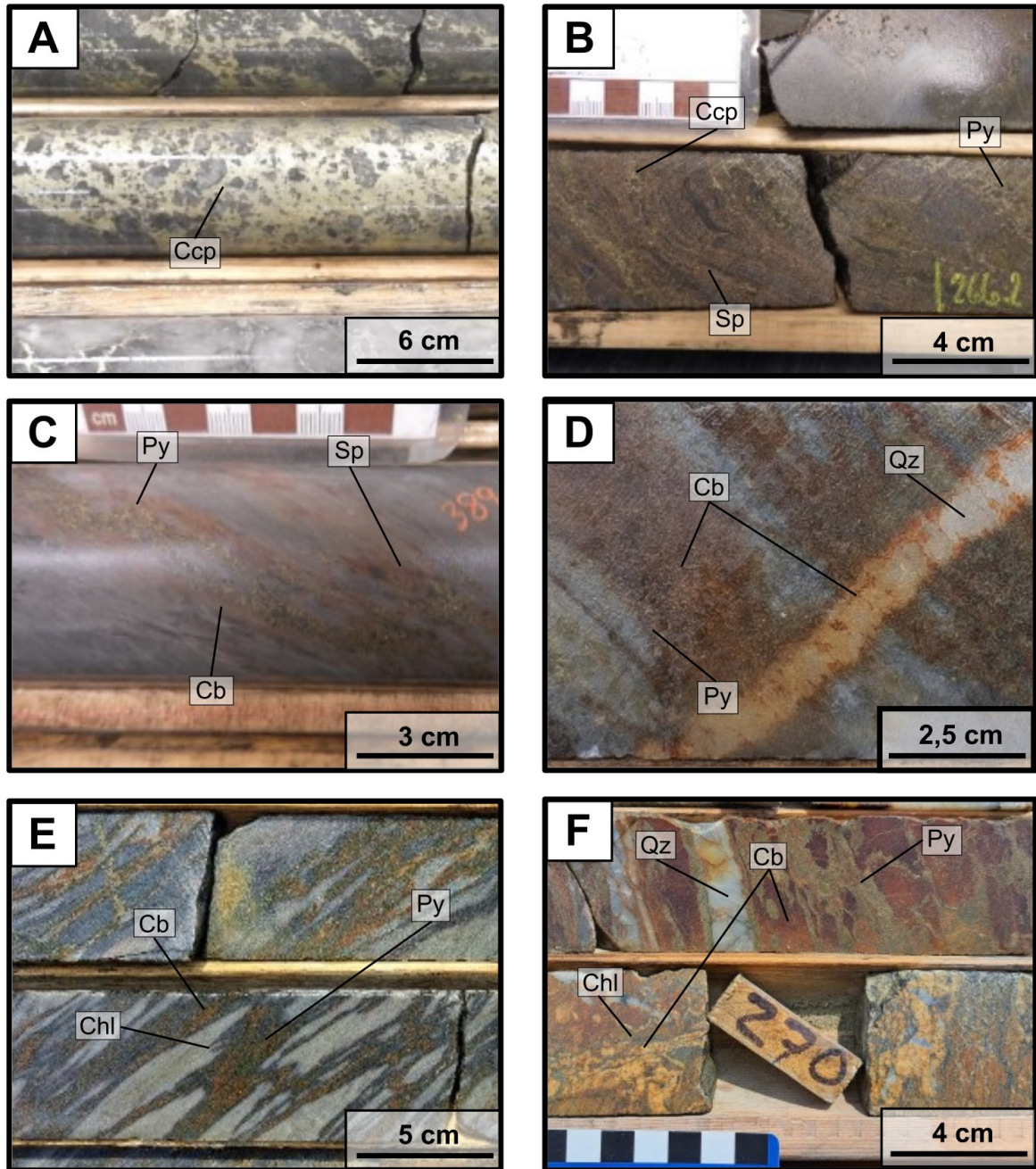
Figure 2.2: Photographs of drill core of the mineralization and carbonate alteration of B26. A. Massive chalcopyrite (Ccp) showing Durchbewegung texture from the Cu-zone (Drill hole 1274-16-236, 1082.5m deep). B. Massive sphalerite (Sph) with minor pyrite (Py) and chalcopyrite from the main Zn-zone (1274-14-185M, 266m deep). C. Disseminations of sphalerite associated with pyrite and carbonate (Cb) of the secondary Zn-zones (1274-16-232, 389.5m deep). D. Rhyolitic tuff with Fe-carbonate alteration cross-cut by a quartz (Qz)-carbonate vein (1274-14-153, 228m deep). E. Carbonate-altered lapilli tuff associated with chlorite (Chl) and pyrite (1274-16-236, 1295m deep). F. Fe-carbonate-pyrite-chlorite breccia (1274-14-160, 270m deep)
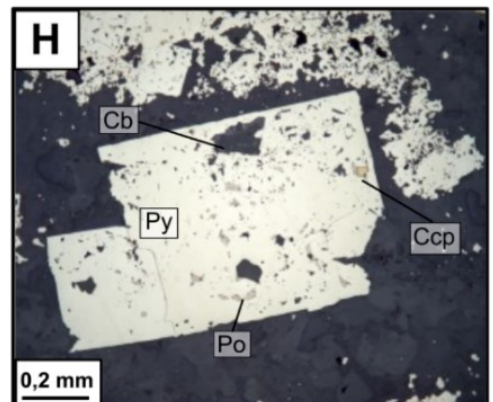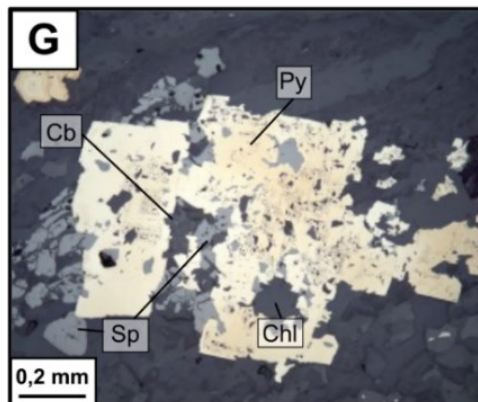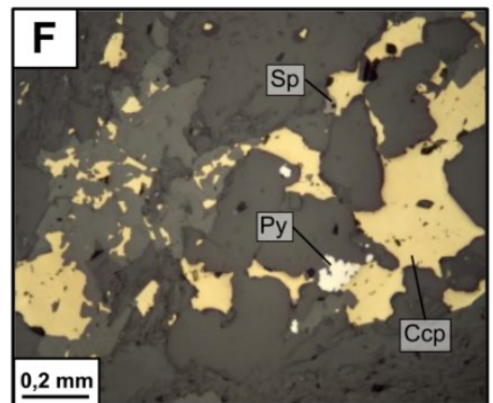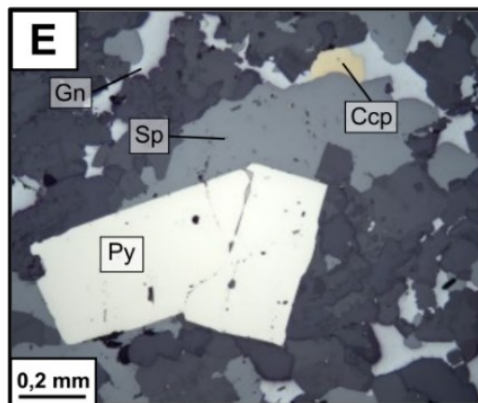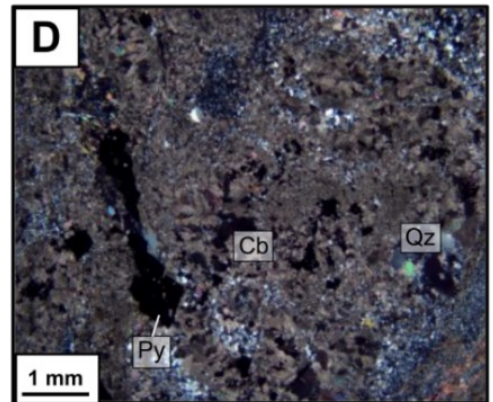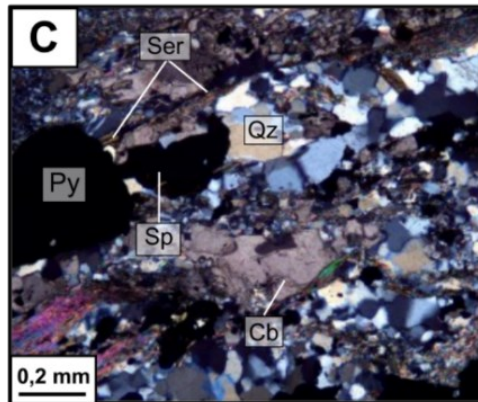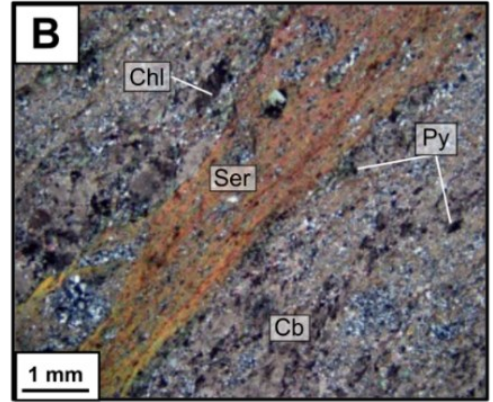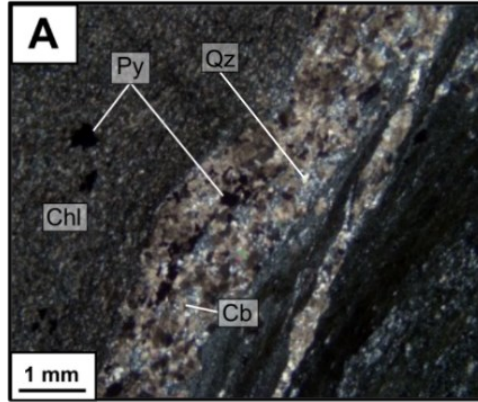
Figure 2.3: Microphotographs of B26 carbonate alteration and pyrite textures. A. Quartz (Qz)-carbonate (Cb) layer in a highly chloritized rhyolitic tuff (B236-1308; drill hole: 1274-16-236; depth: 1308m). B. Intense carbonate-sericite (Ser) alteration of a rhyolitic tuff, with minor chlorite (Chl) and pyrite (Py; B184-325,2; drill hole: 1274-14-184; depth: 325.2m). C. Carbonate-sericite alteration associated with pyrite and sphalerite (Sp) in a rhyolitic tuff (B144-717; drill hole: 1274-14-144; depth: 71.7m). D. Intense carbonatation of porous rhyolitic tuff (B288-240; drill hole: 1274-19-288; depth: 240m). E. Euhedral pyrite grains associated with sphalerite, chalcopyrite (Ccp) and galena (Gn; B242-790.3; drill hole: 1274-17-242; depth: 790.3m). F. Amorphous pyrite-chalcopyrite-sphalerite cluster (B190-321.3; drill hole: 1274-14-190; depth: 321.3m). G. Zoned pyrite with sphalerite, chlorite and carbonate inclusions (B288-226.8; drill hole: 1274-18-288; depth: 226.8m). H. Zoned pyrite with carbonate and pyrrhotite (Po) inclusions (B288-240; drill hole: 1274-18-288; depth: 240m).

# CHAPTER 3

# METHODS

## 3.1 Sampling strategy

The hanging-wall of the mineralization was identified as the most altered in carbonates, thus, sampling was focused on this unit. Twenty-three samples, containing both pyrite and carbonates, were taken along the hanging-wall on 2 transects. The first comprised thirteen drill core samples along a 2 km-long E-W transect centered on the B26 deposit (termed B26 transect). The second was a 3-km transect made between 6.5km and 3.5km West of B26 mineralization, with ten more samples (termed B26 West transect). The stratigraphy is less well-known in this area west of B26, so the focus was made on the carbonate-rich units. For each sample, a thin section and geochemical analyses were realized. As the Selbaie area was metamorphosed to greenschist facies (Lacroix, 1994), both pyrite and carbonate could have either a volcanogenic or a metamorphic origin. Sampling end-members for volcanogenic mineralization in the area helped understand the origin of the pyrite-carbonate bearing units and their link to these mineralizations using mineral chemistry. The volcanogenic signatures were obtained by reanalyzing historical polished thin sections: 5 for Selbaie epithermal mineralization (Faure et al. 1996), and 5 for B26 VMS mineralization (Cu-zone, main Zn-zone, secondary Zn-zones and ankerite-magnetite veins; Fayard, 2020). Location and a brief description of the samples used in this study are in Electronic Supplementary Material - S1.

## 3.2 Whole-rock analyses

On the B26 project, between 2013 and 2019, a total of 2565 whole-rock geochemical analyses were made by SOQUEM with the commercial laboratory ALS Minerals. Most of the analyses followed the protocol SOQ-5, combining Li-metaborate fusion with induced-coupled plasma atomic emission

spectroscopy (ICP-AES) analysis for major elements and induced-coupled plasma-mass spectroscopy (ICP-MS) for trace elements, including Zr, and four-acid digestion with ICP-MS analysis for Ag, Cd, Co, Cu, Li, Mo, Ni, Pb, Sc, Zn. This analytical protocol provides 66 elements, including majors, traces, REE, base metals and loss on ignition (LOI). Details about the protocols, with the corresponding limits of detection and data quality are presented in Electronic Supplementary Materials – S2 and S3. This database was used to document the alteration patterns and their variations in and around B26, as well as the extent of the carbonate alteration in the area.

Twenty-two additional analyses for base metals and trace elements were conducted on the samples collected for this study. As most units have already been sampled by SOQUEM, only complementary analyses have been conducted on the same samples. This resampling was made in order to improve detection limits for 48 trace elements, including semi-volatile elements, using four-acid digestion coupled with ICP-MS analysis at ALS Laboratory (ME-MS61 package). The reference materials used are OREAS 621, a mineralized rhyodacite from Gossan Hill VMS in Australia and CDN-ME-1414, a semi-massive sulfide from Archean VMS mineralization. The relative difference between certified and analyzed values is lower than 10% for most elements, except Se and Sb for the 2021 values and Mo for 2022 values. All reference material data are presented in Electronic Supplementary Material – S3.

## 3.3   Micro-XRF maps of polished thin sections

Micro-XRF maps were performed on 3 polished thin sections of the B26 transect in order to study in detail the chemistry and the textures of the alteration. The Bruker-Tornado M4, equipped with a Rhodium anode, at Université Laval, Québec was used.  Maps (presented in Annex 2) were produced from 20µm points on a 20µm grid, each point analyzed for 5ms with a 50kV voltage and 600µA current. The chosen samples represent the main types of alteration found in B26 carbonate alteration: one sample from the secondary Zn-zones (259-462.3A), one with a carbonate-sericite-chlorite

assemblage (B144-717), and one with a carbonate-chlorite alteration (B236-1308). Micro-XRF maps were initially made to highlight some possible geochemical zonation within the carbonate masses but no such observations have been made, possibly due to the small size of grains within the felsic tuffs and the large amount of inclusions (Figure 2.2a-d). Still, these maps were used as a support to petrological observations.

## 3.4  LA-ICP-MS analyses for mineral chemistry

Trace elements in carbonates, pyrite and sphalerite were analyzed by LA-ICP-MS (Laser Ablation Inductively Coupled Plasma Mass Spectrometry) at LabMaTer, Université du Québec à Chicoutimi (UQAC). The LA-ICP-MS system comprises an Agilent 7900 ICP-MS, coupled with an ArF RESOLution M-50 Excimer (193 nm) laser. For all the minerals, ablation lines were made with a laser beam of 55µm and at a speed of 10µm/s. Ablation lines of 60s followed a background acquisition of the gas blank of 20 to 30s. Lines were preferred to identify micro-inclusions and any zonation of the minerals, following the protocol of Genna and Gaboury (2015). For all the analyzed samples, an average of 6 analyses were made per mineral. The number of analyses ranged from 1 to 10 depending on the abundance of the minerals and the textural variations. Data reduction was carried out using Iolite 4 software (Paton et al., 2011).

### 3.4.1  LA-ICP-MS on carbonates

For the carbonates, 48 isotopes were measured : $^{7}$Li, $^{24}$Mg, $^{27}$Al, $^{29}$Si, $^{31}$P, $^{34}$S, $^{44}$Ca, $^{47}$Ti, $^{55}$Mn, $^{57}$Fe, $^{59}$Co, $^{60}$Ni, $^{63}$Cu, $^{66}$Zn, $^{71}$Ga, $^{74}$Ge, $^{75}$As, $^{77}$Se, $^{88}$Sr, $^{89}$Y, $^{95}$Mo, $^{109}$Ag, $^{111}$Cd, $^{115}$In, $^{118}$Sn, $^{121}$Sb, $^{125}$Te, $^{137}$Ba, $^{139}$La, $^{140}$Ce, $^{141}$Pr, $^{146}$Nd, $^{147}$Sm, $^{151}$Eu, $^{153}$Eu, $^{157}$Gd, $^{159}$Tb, $^{163}$Dy, $^{165}$Ho, $^{166}$Er, $^{169}$Tm, $^{172}$Yb, $^{175}$Lu, $^{182}$W, $^{197}$Au, $^{205}$Tl, $^{208}$Pb, $^{209}$Bi. This protocol was used to analyze 177 carbonate grains from 27 thin sections, including 5 from B26 mineralization from Fayard (2020). Carbonate analyses were calibrated coupling NIST-610 and GSE, following Savard et al. (2023). As multiple reference materials

were used for calibration, data was treated with the Iolite 4 3D Trace elements tool to improve the accuracy of the calibration (Paul et al., 2023). The sum of the major elements constituting the carbonate minerals ($^{24}$Mg, $^{44}$Ca, $^{55}$Mn, $^{57}$Fe) was normalized to 100% using the stoichiometric $CO_2$ content of each carbonate mineral. Analysis of carbonate reference materials (GProbe 4 and MACS-3) were used for data quality (data presented in Electronic Supplementary Material – S4): most trace elements in carbonate reference materials were within 10% accuracy and 10% precision. To demonstrate that this method of calibration is accurate for carbonate analysis, 7 samples from the carbonate alteration of Normétal VMS system (Lafrance 2003) were analysed by LA-ICP-MS and the major elements were compared to the microprobe data of Lafrance (2003, Electronic Supplementary Material – S5). For calcite and siderite, major elements systematically have less than 10% difference between microprobe and LA-ICP-MS data. However, for ankerite, variation within a single analysis can be significant. Since, there is no indication of the location of the microprobe point on the thin section, it is not necessarily the same carbonate grain that have been analyzed with LA-ICP-MS. Still, the low difference observed for major elements in calcite and siderite indicates that the methodology used here is robust to determine the mineralogy of carbonates with LA-ICP-MS.

Some carbonate minerals are highly porous and contain micro-inclusions (Figure 2.3a-d). Several elements were used to detect and exclude micro-inclusions during data reduction: P for phosphates (apatite, monazite), Si and Al for silicate minerals (e.g., sericite, chlorite), Fe and S for sulfides (pyrite, chalcopyrite, sphalerite) and Fe and Ti for Fe-oxides. Apatite and phyllosilicate inclusions may affect the REE+Y content of the carbonate (Genna et al., 2015; Debruyne et al., 2016). Therefore, data with P > 500ppm and/or Si+Al > 2wt.% were removed from the dataset to limit the contamination on REE+Y patterns.

### 3.4.2 LA-ICP-MS on sulfides

For both pyrite and sphalerite analyses, the same sulfide protocol was used to determine the trace elements of these sulfide minerals and also to provide information about inclusions. The 40 isotopes measured were $^{24}$Mg, $^{29}$Si, $^{31}$P, $^{33}$S, $^{34}$S, $^{39}$K, $^{44}$Ca, $^{47}$Ti, $^{51}$V, $^{52}$Cr, $^{55}$Mn, $^{57}$Fe, $^{59}$Co, $^{60}$Ni, $^{65}$Cu, $^{66}$Zn, $^{71}$Ga, $^{73}$Ge, $^{74}$Ge, $^{75}$As, $^{78}$Se, $^{82}$Se, $^{95}$Mo, $^{107}$Ag, $^{111}$Cd, $^{115}$In, $^{118}$Sn, $^{121}$Sb, $^{125}$Te, $^{128}$Te, $^{137}$Ba, $^{182}$W, $^{197}$Au, $^{202}$Hg, $^{204}$Pb, $^{205}$Tl, $^{206}$Pb, $^{207}$Pb, $^{208}$Pb, $^{209}$Bi, $^{238}$U. A total of 224 pyrite grains on 26 thin sections, including 6 thin sections of B26 mineralization from Fayard (2020), were analyzed. In addition, a total of 62 grains of sphalerites were analysed from 6 thin sections: 2 in the Cu-zone, 2 in the main Zn-zone and 2 in the carbonate alteration halo. Analyses of pyrite were calibrated using MASS-1, a U.S. Geological Survey Fe-Cu-Zn-S pressed pellet reference material. The Fe-rich glass GSE was also used for some elements (Co, Ni, Ba, Pb) with better reproductivity and precision (Electronic Supplementary Material – S6). Data quality was monitored using UQAC-FeS1 and UQAC-FeS5 (in-house sulfide reference materials from LabMaTer; Savard et al., 2018; Duran et al., 2019; Baumgartner et al., 2020). $^{57}$Fe was used as the internal standard using stoichiometric values for pyrite analyses. For sphalerite, the stoichiometric sulfur concentration was used as an internal standard to calculate Fe concentration in sphalerite (which varies naturally). The calculated $^{57}$Fe was then used as an internal standard following Gaboury et al. (2021). Data for most trace elements in the sulfide reference materials were within 10% accuracy and 10% precision (Electronic Supplementary Material – S7).

Although micro-inclusions of other sulfides, and in some cases carbonates and Fe-Ti oxides, are common in pyrite, they reflect the metallic signature of the hydrothermal fluid forming the pyrite; either during coprecipitation from the fluid or recrystallization of pyrite (i.e. expulsion of excess metals in pyrite lattice) during zone refining and/or later metamorphism (Huston et al., 1995, Large et al., 2007; Genna and Gaboury, 2015). As such, they were not removed from the signal in this study, following Genna and Gaboury (2015) and Gaboury et al. (2021). Sphalerite was analyzed to use the GGIMFis geothermometer developed by Frenzel et al. (2016), which uses the Ga, Ge, In, Mn and Fe

concentration in sphalerite. The main micro-inclusion mineral in the sphalerite analyses is chalcopyrite, due to the chalcopyrite disease texture, which is common in B26 (Figure 2.3e). Nevertheless, sphalerite is richer in Ga, In and Mn than chalcopyrite (George et al., 2016), so the signature should not be altered significantly.

The most common inclusions, identified with petrography and LA-ICP-MS signals, in pyrites are sulfides, mainly chalcopyrite, sphalerite and galena, Fe-Ti oxides, and in some cases carbonates. Sulfides highly affect Cu, Zn and Pb concentrations resulting in high variations in the concentration of these elements, ranging from 0.1ppm to 5 wt.%. Sulfide inclusions also affect other elements enriched in these mineral phases, positive correlations between the higher values of Cu with high values of In, Sn, Ag and Sb indicating an effect of chalcopyrite inclusions on these elements. Sphalerite inclusions result in nearly perfect positive correlations between Zn and Cd and In, and galena inclusions result in positive correlations between Pb, Ag and Sb. Carbonates have also a major impact on Mn concentrations, which is shown by the positive correlation between Ca and Mn.

# CHAPTER 4

# RESULTS

## 4.1 Whole-rock analyses

### 4.1.1 Lithology classification

As samples collected for this study have been intensively altered, the original volcanic lithologies have been determined using the immobile trace element classification diagram of Winchester and Floyd (1977; Figure 4.1a; Electronic Supplementary Material – S8). Based on this diagram, all of the carbonate-altered samples from the B26 transect are rhyolites, whereas, on the B26 West transect, the carbonate-bearing units was hosted not only in rhyolite but also in dacite and andesite (Figure 4.1a). These samples were then compared to B26 host units using the $Zr/TiO_2$ vs $Al_2O_3/TiO_2$ discrimination diagram of Fayard et al. (2020a), which is efficient for differentiating the three types of rhyolites (A, B and C) identified in the B26 prospect (Figure 4.1b). Samples of carbonate alteration from the B26 transect all have high $Zr/TiO_2$ (2500 to 3700) and $Al_2O_3/TiO_2$ (>100), which corresponds to the signature of the rhyolite A of B26 (Figure 4.1b), host of the mineralization and most of the alteration. The carbonate-altered rhyolites from the B26 West transect have lower $Zr/TiO_2$ (<1000) and $Al_2O_3/TiO_2$ (<100) ratios and are most similar to the chemical signature of rhyolite B (Figure 4.1b). The sampled andesite and dacite samples from B26 West transect have the lowest $Zr/TiO_2$ (<500) and $Al_2O_3/TiO_2$ (<50), typical of andesite and dacite from B26 (Fayard et al., 2020a; Figure 4.1b).

### 4.1.2 Alteration

Few methods have been developed to study carbonate alteration of volcanic rocks; the Chlorite-Carbonate-Pyrite Index (CCPI) developed by Large et al. (2001a) is the only index applied to VMS

deposits. Fayard (2020) showed that, at B26, the increase in the CCPI value mostly reflects the ratio of chlorite/sericite rather than the intensity of the carbonatation. Other methods useful for studying carbonate alteration are normative calculations. Piché and Jébrak (2006) and Faure (2012) already highlighted the intense carbonatation in the Selbaie mining camp using respectively NORMAT normative mineral alteration index from Piché and Jébrak (2004) and the Alt_Carb_SV350 index from Trépanier (2013; Annex 1). These methods illustrate the importance of carbonate alteration in the Selbaie mining camp as observed petrographically in the samples (Figures 2.2, 2.3).

For this study, normative calculations were made using CONSONORM_LG from Trépanier et al. (2015) on SOQUEM's database (N=2755), in order to quantify the carbonatation in and around the B26 deposit and detect the zoning of the carbonate mineralogy. The map on Figure 4.2 shows the extents of normative calcite (>3%), ankerite (>1.5%) and siderite (>0.3%). These thresholds correspond to the 80th percentile and were chosen to discriminate the background carbonatation commonly associated with greenschist metamorphism (Groves et al., 1987; Veizer et al., 1989a).

Normative carbonates show a wide alteration halo, with anomalous values of normative ankerite (>1.5%) up to 1km away from the deposit on either side of the B26 transect (Figure 4.2). Siderite is dominant in the vicinity (<500m) of the mineralized zones. The upper hanging-wall and the footwall of B26 are dominated by calcite (Figure 4.2). Domination of calcite is also observed on the B26 West transect, 3.5km west from B26. There, most of the samples are calcite-dominated, with 1.2 to 9.5% of normative calcite, but three samples are dominated by Fe-carbonates, with over 15% of normative ankerite or siderite. The lack of geological constraints (absence of outcrops and low drill hole density) on this B26 West transect, limits our ability to clearly see the lateral zonality of these Fe-carbonate-enriched units. However, it shows that the carbonate alteration in B26 is stratabound and continuous over more than 2km.

Figure 4.3 shows the volcanic sequence and its alteration assemblage along two different drill holes, one crosscutting the B26 main Zn-zone (1274-17-259: 562m long; Figure 4.3a), and the other located in the proximal alteration halo, 250m west of the massive sulfide lenses (1274-16-236: 1533m long; Figures 4.2 and 4.3b). The drill hole 1274-17-259 mainly intersects rhyolites A and B, as well as dacite and a quartz-feldspar porphyry (QFP) intrusive (Figures 4.2 and 4.3a). The drill hole 1274-16-236 first intersects a succession of felsic to intermediate volcanic units followed by the felsic members, rhyolites A and B (Figure 4.3b). In both cases, the highest Cu values (>0.5%) are located in the footwall and the high Zn values (> 0.5%) are at the top of the footwall and in the hanging-wall; only the main Zn-zone contains both Cu and Zn.

In terms of alteration, in both drill holes there is a systematic difference between the footwall and the hanging-wall of the mineralization, highlighted by the normative calculations of carbonate minerals (calcite, ankerite, siderite; Trépanier et al., 2015) and the Spitz-Darling Index (Spitz and Darling, 1978). Along the B26 transect, the alteration in the footwall is thick, up to 450m, characterized by a Spitz-Darling Index over 100, indicating an important leaching of the host rock, and a normative carbonate index close to 0%. There is also a decrease of the Eu/Eu* ratio in the rhyolites, compared to the least-altered rock data from Fayard (2020). These three features indicate an intense leaching of the host rock, which is consistent with the observation of a dominant chlorite-sericite alteration assemblage in B26 by Fayard et al. (2020b). On the other hand, the hanging-wall is characterized by a lower Spitz-Darling Index (<10), an increase in the Eu/Eu* ratio, compared to precursor (Fayard, 2020) and the apparition of normative carbonates: calcite, ankerite and siderite for the hole 1274-17-259 and ankerite and siderite for the drill hole1274-16-236. Carbonatation is the most intense in the hanging-wall, with up to 50% of normative ankerite and siderite (Figure 4.3b). In the drill hole 1274-16-236, carbonatation is also present up to 800m below the mineralization within the felsic-intermediate volcanic successions. In this case, it is dominated by normative calcite (5-15%) with minor normative ankerite (<3%).

The alteration indexes used here, as well as the normative calculations, highlight the differences in the alteration assemblages in B26, with an intensively leached footwall, dominated by chlorite-sericite, and a carbonated hanging-wall, dominated by Fe-carbonates. Those Fe-carbonates are however less abundant directly over the mineralization compared to the proximal and intermediate alteration halo (Figure 4.3a and b). Both footwall and hanging-wall are wrapped by a calcite-dominated, pervasive alteration. These features highlight the semi-concordant geometry of the carbonate alteration in B26, which is also typical of the Mattabi-type deposits, as defined by Morton and Franklin (1987). The size of the carbonate alteration zones is similar to that of the model developed by Lafrance (2003) for the Normétal deposit, with an Fe-carbonate halo extending several kilometres away from the mineralization.

## 4.2   Carbonate geochemistry

### 4.2.1   Carbonate classification

Carbonate minerals are important components in the B26 alteration halo forming between 5 and 40% of the composition of the altered samples. It is usually found as amorphous millimetric to centimetric masses disseminated in the volcaniclastic units or veinlets crosscutting previously carbonate-altered units (Figures 2.2 and 2.3). They are systematically associated with other alteration phases, especially sericite, chlorite and pyrite (Figure 2.3 a-d). This association between phyllosilicates, sulfides and carbonates is particularly visible on µXRF maps (Annex 2). In this study, classification of carbonate minerals follows the nomenclature used by Lafrance (2003), based on Berry and Mason (1959) and Deer et al. (1967). The calcite and siderite poles are quite pure with, respectively, Ca/(Ca+Fe+Mg) and Fe/(Ca+Fe+Mg) over 85%, with minor amounts of Mg (0.01 to 4% in calcite, and 1 to 8% in siderite) and Mn (0.3 to 1.5% in calcite, and 2 to 10% in siderite). The ankerite-dolomite series displays a solid solution between pure dolomite $((Ca,Mg)(CO_3)_2)$ and ferrodolomite $((Ca,Fe)(CO_3)_2)$. In B26 and its carbonate alteration halo, the carbonates, determined

by LA-ICP-MS, comprise the three species: calcite (33 grains), siderite-sideroplesite (27 grains) and 100 grains from the ankerite-dolomite series (Figure 4.4). Most samples only contain one type of carbonate mineral. When several carbonate minerals coexist in the same sample, it is due to zoning in a large carbonate mass (Figure 2.3d). The mineralogy of the analyzed carbonate is consistent with the observations made with the normative calculations.

## 4.2.2   Minor and trace elements in carbonates

The minor and trace element data of carbonates is shown on box and whisker plots in Figure 4.5 (other elements are shown in Annex 3). Only Sr (350ppm in median) and Zn (60ppm in median) are the most abundant minor elements in carbonates. Semi-volatile metals (Ag, Cd, In, Sn, Sb, Au, Tl, and Bi) are low in carbonates and most of the analyses for these elements are near the detection limit (Figure 4.5). Ca-rich carbonates (calcite and ankerite-dolomite series) tend to be enriched in Sr (50 to 5000ppm) and Pb (1 to 50ppm), as Sr and Pb substitute for Ca in the carbonate lattice (Berry and Mason, 1959; Speer, 1983). On the other hand, Fe-bearing carbonates are richer in Cu, Li, Mn, Co, Ni (1 to 100ppm), Ga and Mo (0.1 to 1ppm; Figure 4.5; Electronic Supplementary Material – S9), as all these elements substitute for Fe (Co, Cu, Mn; Berry and Mason, 1959; Reeder, 1983; Veizer, 1983) and Mg (Co, Cd, Cu, Ni, Li, Berry and Mason, 1959; Reeder, 1983; Veizer, 1983; Barton et al., 2014).

However, the rare earth elements (REE) and Y are the focus of this study because they have been widely studied and their capacity to trace geochemical processes and to characterize the involved hydrothermal fluids has been demonstrated (Bau, 1991; Bau and Möller, 1992; Bau, 1996; Debruyne et al., 2016; Smrzka et al., 2019). The total REE concentration in the carbonates varies from 1 to 803ppm. Concentrations of total REE+Y in carbonates depend on the mineralogy, specifically the Ca content: calcite is usually the most REE-enriched of the carbonate minerals (median value of ∑REE = 51ppm), followed by the ankerite-dolomite series (∑REE = 24ppm) and then siderite (∑REE =

16ppm). In theory, Ca-rich carbonates should be enriched in light rare earth elements (LREE) and Fe and Mg-rich carbonates should easily incorporate heavy rare earth elements (HREE) due to similar ionic radii (Shannon, 1976; Bau and Möller, 1992; De Bruyne et al., 2016; Figure 4.5). However, our study points out that mineralogy does not affect significantly the REE+Y pattern shapes. It only influences the REE+Y concentrations in the carbonates.

The carbonates analyzed were divided into three types using REE+Y chondrite-normalized (CN) patterns, as well as Eu and Y anomalies (Figure 4.6). Type 1 carbonates (N = 9 samples, n = 40 analyses) are Fe-bearing carbonates (ankerite to siderite), located directly in the mineralization or in its direct vicinity. They are the most enriched in REE, with a median of 250 times chondrite values. The main characteristic of type 1 is a weakly fractionated REE+Y pattern ([La/Yb]$_{CN}$ = 0.71) with a marked negative Eu anomaly ([Eu/Eu*]$_{CN}$ = 0.37) and no Y anomaly (Y/Ho = 30; Figure 4.6a). Type 2 carbonates (N = 13, n = 110) comprise mainly the ankerite-dolomite series and a few calcites, with moderate REE concentrations and a median 100 times chondrite values. They are the most common in B26, occurring in the mineralization, in the secondary Zn-zones, in ankerite-magnetite veins located directly over B26, but also all along the transect in the alteration halo, and even the B26 West transect. Type 2 carbonates are characterized by a slight LREE-enriched pattern ([La/Yb]$_{CN}$ = 1.67) and a systematic significant positive Eu positive anomaly ([Eu/Eu*]$_{CN}$=2.25) and no anomaly in Y (Y/Ho = 20; Figure 4.6b). Type 3 carbonates (N = 4, n = 28) comprise calcite and siderite. They have a scarce distribution in the B26 camp, with no visible spatial link to the deposit or any known major structure. However, they are most common in the distal alteration halo, especially on the B26 West transect. These carbonates exhibit the lowest REE abundance, with a median of 30 times chondrite values. The distinctive spoon-shaped (concave) REE+Y pattern, with an unusually low abundance of LREE and medium rare earth elements (MREE), and an enrichment in HREE ([La/Yb]$_{CN}$ = 0.50), is characteristic of type 3 carbonates. They also have a negative Eu anomaly ([Eu/Eu*]$_{CN}$ = 0.66) and positive La and Y anomalies (Y/Ho = 36) (Figure 4.6c). Within type 3 carbonates, there is considerable variability in their REE+Y spectra, even within a sample or a carbonate mass, with a strongly marked

spoon-shaped pattern in the center and a flat pattern, richer in total REE+Y on the borders of the carbonate mass. The spatial distribution of the different types of carbonate is shown in Annex 5.

A binary diagram, using the Eu anomaly and the Y/Ho ratio, can be used to discriminate all three types of carbonate described using the REE+Y patterns (Figure 4.7). Type 1 carbonate, including those from the mineralization display a negative Eu anomaly as well as a low Y/Ho ratio (>35). Type 2 carbonate, which are dominating the carbonate alteration halo are characterized by a positive Eu anomaly and a low Y/Ho ratio (>35). Finally, type 3 carbonates, found mostly on the B26 West transect have a high Y/Ho ratio (35 to 50), with a usually slightly marked Eu anomaly, which could be whether positive or negative. This diagram can be used for the classification of carbonates in the B26 area.

## 4.3   Trace elements in pyrite

### 4.3.1   Textural characteristics of pyrite and its affect on trace element chemistry

Pyrite is ubiquitous in B26 and its alteration halo, particularly in the semi-concordant carbonate alteration halo. It is found as disseminations in and around the carbonate masses and sometimes as thin layers or veinlets within the rhyolitic tuffs (Figure 2.2b-f). In most cases, pyrite is associated with other alteration minerals (carbonates, chlorite, sericite) and in some cases with other sulfides (sphalerite, chalcopyrite, galena) or Fe-Ti oxides (magnetite, ilmenite) (Figures 2.2-2.3; Annex 2), which suggests a cogenetic link between carbonate and the other alteration minerals.

A large variety of textures have been observed microscopically for pyrite. The most common is subhedral pyrite grains, zoned with a porous core and clear borders (Figure 2.3g-h), which resembles to the pyrites described in other VMS districts (Mt Read, Large, 1992; Matagami, Genna and Gaboury,

2015; Bathurst, Soltani-Dehnavi et al., 2018). The clear borders in these pyrites are characteristic of recrystallization due to continuous fluid flows, caused by zone refining, metamorphism or deformation (Eldridge et al., 1987; Huston et al., 1995; Large et al., 2007). Amorphous mass of pyrite and veinlets are also common textures observed in B26 (Figure 2.3f).

## 4.3.2   Trace elements in pyrite

Pyrites from the B26 mineralization are classified by ore type: Cu-zone and main Zn-zone. Those from the carbonate-alteration are further grouped according to the distance of the samples to the B26 mineralization: 1) proximal (N = 7, n = 43) are less than 250m away from the mineralized lenses; 2) intermediate (N = 6, n = 44) are from 250 to 700m and 3) distal (N = 47, n = 6) are more than 3km from B26 and comprise all the data from the B26 West transect. All proximal and intermediate samples are located within the hanging-wall, in the most intensively carbonated rocks (Annex 6). The zonation observed in the textures of the pyrites is reflected in the geochemical signature, with the core enriched in semi-volatile elements, while the borders display higher concentrations in Ni, Co and As (Figure 2.3g-h; Annex 4).

For each group of pyrite, most of the analyzed elements are above the limit of detection of the LA-ICP-MS (Figure 4.8), with only Te and Hg having a significant number of analyses below detection limit (Electronic Supplementary Material – S10). A selection of trace element data detected in pyrite is plotted on the box and whisker plot (Figure 4.8; other elements are shown in Annex 5). Pyrite from the mineralized zones (both Zn and Cu-zones) are the most enriched in the majority of trace elements: Co, Pb (100 to 10000ppm), Ag, Cu, Se (10 to 100ppm), Bi, Hg, Cd Sn, Sb, Tl (0.1 to 10ppm), Au and In (<0.1ppm; Figure 4.8) compared to pyrite from the carbonate-alteration. Among the mineralized zones, pyrite from the Cu-zone displays the highest concentrations in most elements, in particular Bi (median value of 45ppm), In (0.4ppm) and Se (110ppm), and the lowest concentrations in Mn, Sb, Ga, Te and most notably As (0.3ppm) and Zn (0.7ppm). Pyrite from the Zn-zone exhibits the highest

27

concentrations in As (1240ppm), Sb (6ppm) and Zn (95ppm). In contrast, pyrites from proximal and intermediate samples are similar or depleted in most trace elements compared to the pyrite from the B26 ore zones (Figure 4.8). Pyrites from the distal carbonate alteration of B26 West have the highest values in Mn (82ppm), V (0.7ppm) and Te (0.3ppm) of all pyrite (both from mineralization and carbonate-alteration) but display similar concentrations of the other elements in pyrite from the carbonate alteration of the B26 transect (Figure 4.8).

Binary diagrams (Figure 4.9) showcasing variations in certain pyrite trace elements (Ag, As, Co, Mn, Se, V), highlighted by the box plot diagrams of Figure 4.8, are useful for discriminating pyrites from the different lithologies and different locations. It is possible to distinguish pyrites from the B26 and B26 West transects using their Mn and V contents, as pyrites from the B26 West transect are enriched in V (>0.2ppm) and Mn (>10ppm) compared to those of B26 (Figure 4.9a). This Mn vs V diagram shows that pyrite from the two transects may have different origins (see discussion below). Thus, the next diagrams only use data from the B26 transect in order to differentiate the mineralization from the carbonate alteration and distinguish the Cu-zone from the Zn-zone.

Using semi-volatile and/or magmatic elements (Se, Ag; Figure 4.9b; Co, As; Figure 4.9c) is particularly efficient to: 1) differentiate the carbonate alteration to the mineralization, most enriched in most elements (Figure 4.9b, c) and, 2) separate pyrites from the Cu and Zn-zones as those from the Cu-zone are highly depleted in As (<10ppm), plotting several orders of magnitude below the Zn-zone and the carbonate alteration (Figure 4.9c). It is finally possible to see a difference in the trace element content of the pyrite with distance to the mineralization, intermediate pyrites being depleted in Se, Ag, Co and As compared to proximal pyrites, highlighting these elements as potential vectors for exploration (Figure 4.9b, c).

## 4.4   Trace elements in sphalerite

Sphalerites analyzed in B26 display equilibrium textures with pyrite, carbonates and other alteration minerals (Figure 2.3c, e, f, g). They are present as amorphous grains on the borders of other sulfides, mainly pyrite or chalcopyrite. The main inclusions identified in sphalerite are chalcopyrite, with a chalcopyrite disease texture (Figure 2.3e), and galena.

A wide variety of trace elements are present in B26 sphalerites (N = 6; n = 32), with Fe and Cd being the most important minor elements, with concentration ranging from 0.2 to 0.5% for Cd and 0.5 to 6% for Fe (Electronic Supplementary Material – S11). Notable trace elements include Mn, Cu, Co, Se, In, Pb with a range of concentration between 10 to 100ppm. Other notable elements are As and Hg (1 to 10ppm), and Ga and Sb (0.1 to 1ppm). The remaining elements are often below the detection limit, including Bi, Au, Tl, W, Te and Ge. Sphalerite from the mineralization is the most enriched in most trace elements, with the exception of Ag, Hg, Pb and Sb. Within the mineralization, sphalerite from the Cu-zone displays the highest concentration in Bi, Co, Cu, Ga, Ge, In, Mn and Se whereas they are depleted in Cd, Ag and Sb. Sphalerite from the Zn-zone is particularly enriched in Cd (median value = 5969ppm) and As (2 ppm) whereas those from the Cu-zone are slightly depleted (Cd = 2603ppm).

Sphalerite trace element content has been shown to be controlled by fluid temperature (Frenzel et al., 2016). In this study, we have used the Ga, Ge, In, Mn, Fe in sphalerite (GGIMFis) geothermometer following the equations of Frenzel et al. (2016), which is based on the correlations between homogenization temperature of fluid inclusions in sphalerite and co-existing concentrations of Ga, Ge, Fe, Mn and In of sphalerite:

$$PC1^* = ln\left(\frac{C_{Ga}^{0.22} \times C_{Ge}^{0.22}}{C_{Fe}^{0.37} \times C_{Mn}^{0.20} \times C_{In}^{0.11}}\right)$$

$$T\ (°C) = -(54.4 \pm 7.3)PC1* + (208 \pm 10)$$

As many Ge analyses were below the detection limit, a fixed value was given to these analyses, corresponding to the limit of detection of Ge itself, following the recommendation of Frenzel et al. (2016). It leads to an underestimation of the variability of the calculated temperatures from the Zn-zone and the alteration halo. Chalcopyrite inclusions, and the chalcopyrite disease textures were discussed by Frenzel et al. (2016) and seem to have a minor impact on the geothermometer.

Sphalerite from the Cu and Zn mineralization gives a calculated median temperature of 346 ± 28°C, with no significant difference between the two zones of mineralization. These temperatures are consistent with temperatures of VMS mineralization formed by replacement (Large, 1992; Galley et al., 2007; Schardt and Large, 2009), confirming the model of Fayard (2020). Sphalerite from the carbonate alteration records slightly cooler temperatures, with a calculated median temperature of 315 ± 24 °C (Figure 4.10). However, this is much higher than the 248 ± 12°C°C measured at the Kidd Creek VMS deposit (Abitibi, Ontario, Canada), by Schandl and Bleeker (1999) in fluid inclusions in siderite from the talc-carbonate-altered units.
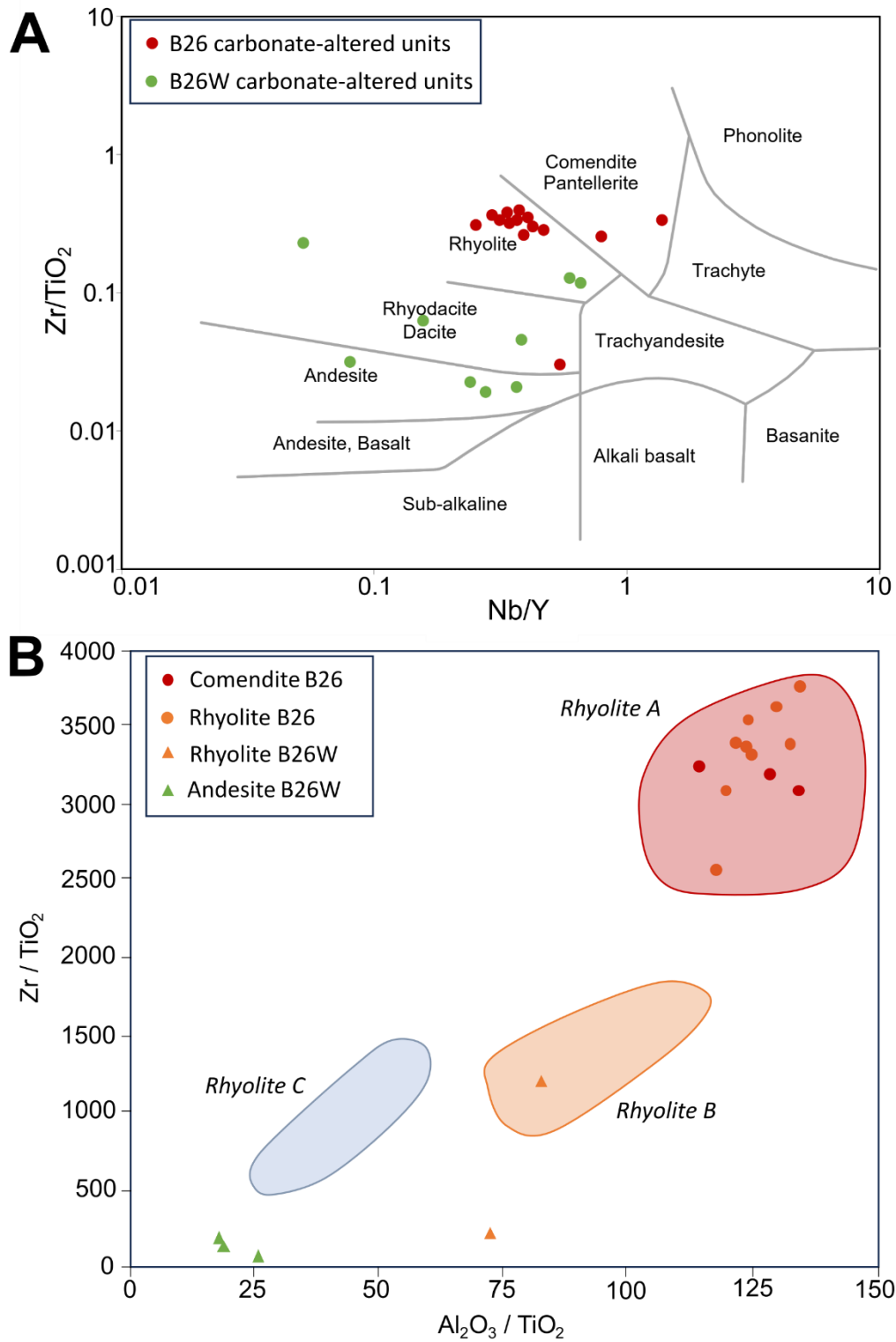
Figure 4.1: Lithogeochemical classification of volcanic rocks from B26. A. Zr/TiO$_2$ vs. Nb/Y binary diagram of Winchester and Floyd (1977) to classify altered volcanic rocks. B. Zr/TiO$_2$ vs Al$_2$O$_3$/TiO$_2$ discrimination diagram to classify the 3 rhyolite types of B26 (coloured fields from Fayard, 2020)
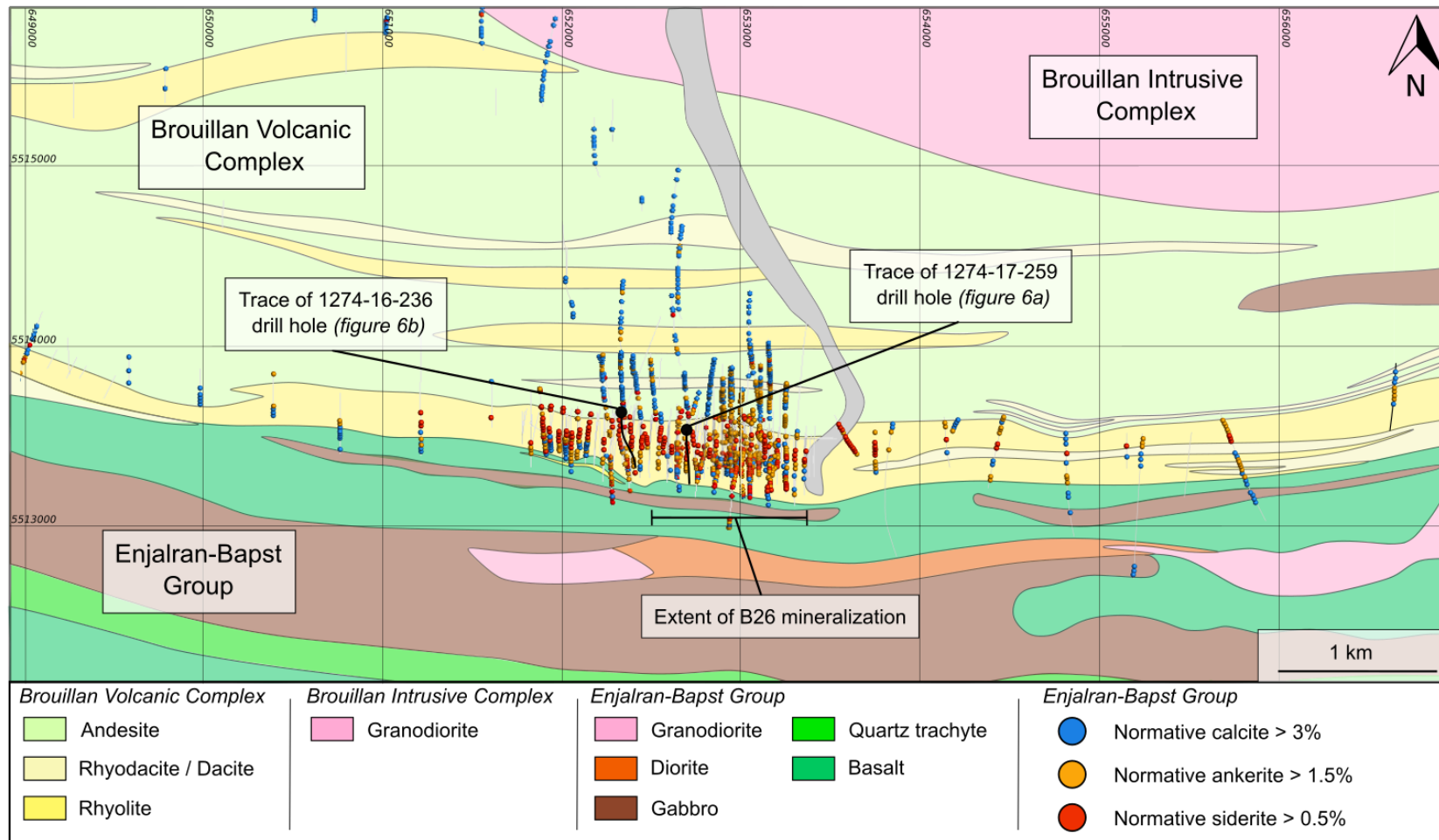
Figure 4.2: Geological map of the B26 transect centered on B26 mineralization showing the normative carbonate alteration calculated using CONSONORM_LG (Trépanier et al., 2015) using the database of SOQUEM (n = 2755)
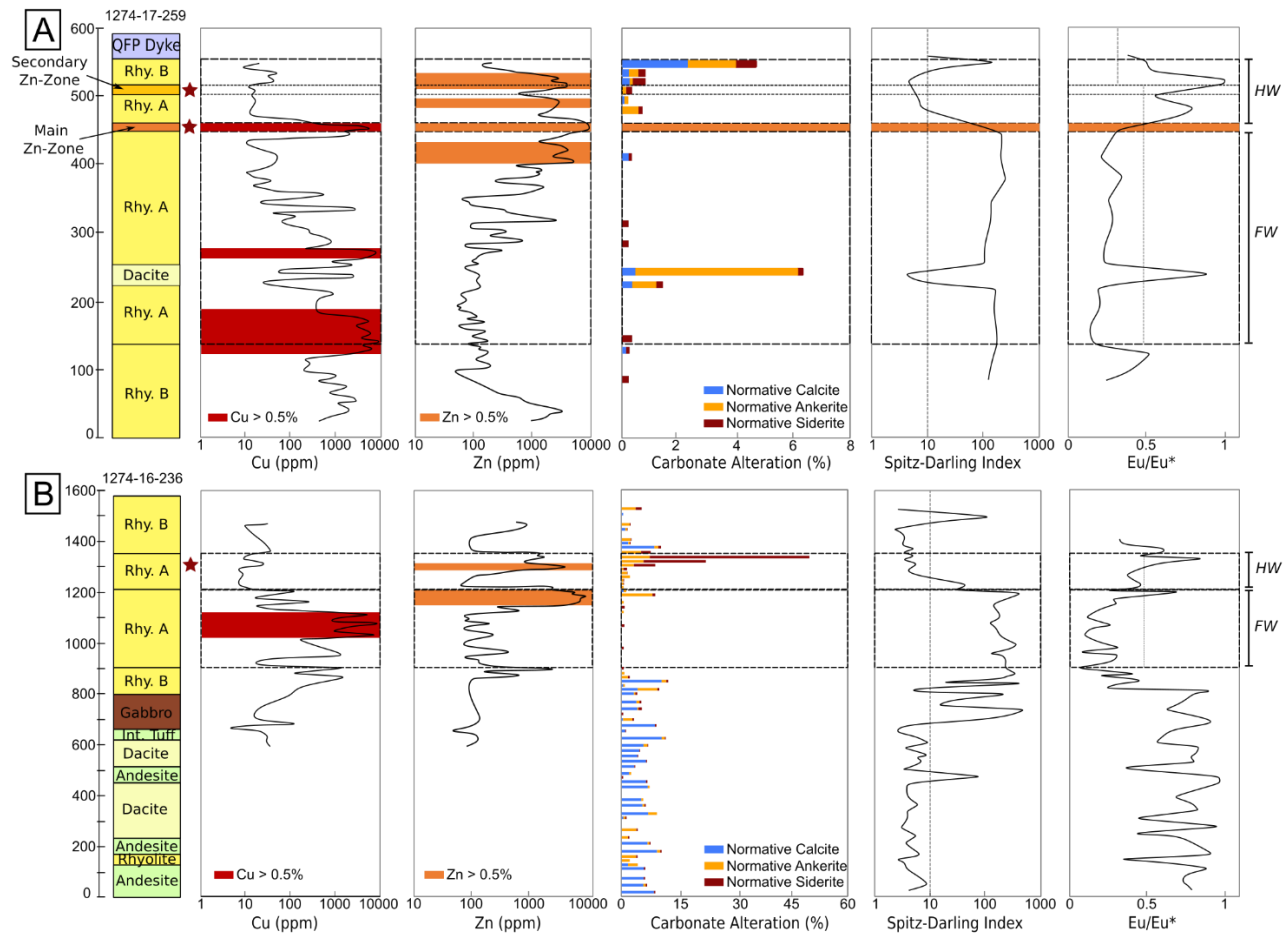
Figure 4.3: Geologic and geochemical profiles of drill holes A. 1274-17-259 (proximal alteration) and B. 1274-16-236 (intermediate alteration). Horizontal lines give the limits of the footwall and the hanging wall, in both drill holes, the footwall is intercepted first. Normative carbonate calculations were realized using CONSONORM_LG (Trépanier et al., 2013). Spitz-Darling Index ($Na_2O/Al_2O_3$) is a proxy for leaching, vertical line represents the value for non-leached rhyolites (Spitz and Darling, 1978). Vertical lines on the Eu/Eu* graph represents the value for fresh samples given by Fayard et al. (2020a). Red stars shows the location of samples from this study taken from these drill holes. HW = Hanging-wall;  FW = Footwall
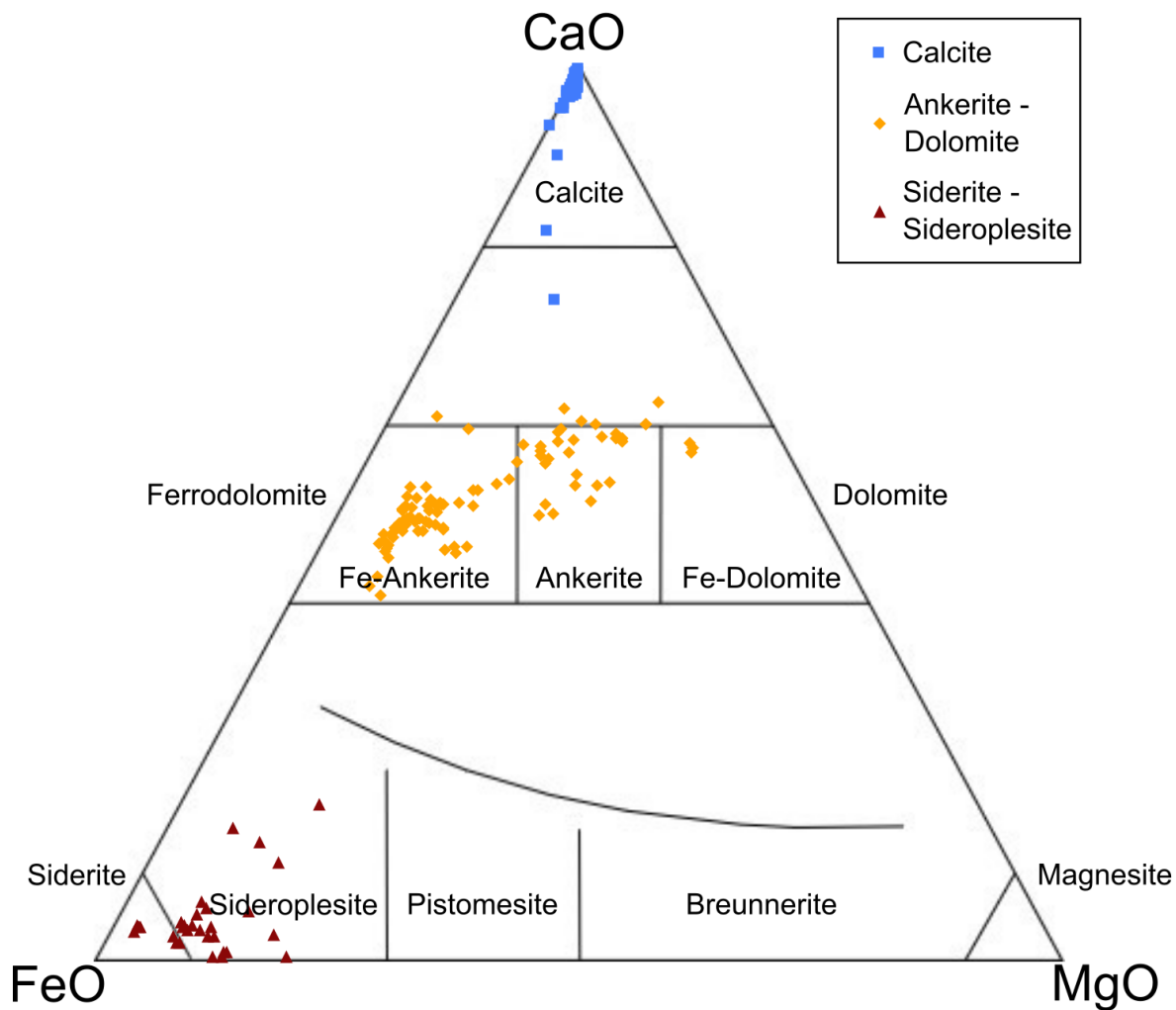
Figure 4.4: Ternary diagram (CaO, FeO, MgO, in wt.%) of carbonate mineralogy from B26. Fields are from Lafrance (2003) after Berry and Mason (1959) and Deer et al. (1967). N = 22 samples; n = 177 analyses

Figure 4.5: Box plot diagrams showing the variations of selected trace elements of carbonates at B26, according to their mineralogy (calcite, ankerite-dolomite, siderite). Limit of detection (LOD) is represented by a light gray dash line; if it is not present, the detection limit is below the limits of the diagram. LREE = Light Rare Earth Elements; HREE = Heavy Rare Earth Elements; REE = Rare Earth Elements; N = number of samples; n = number of analyses.
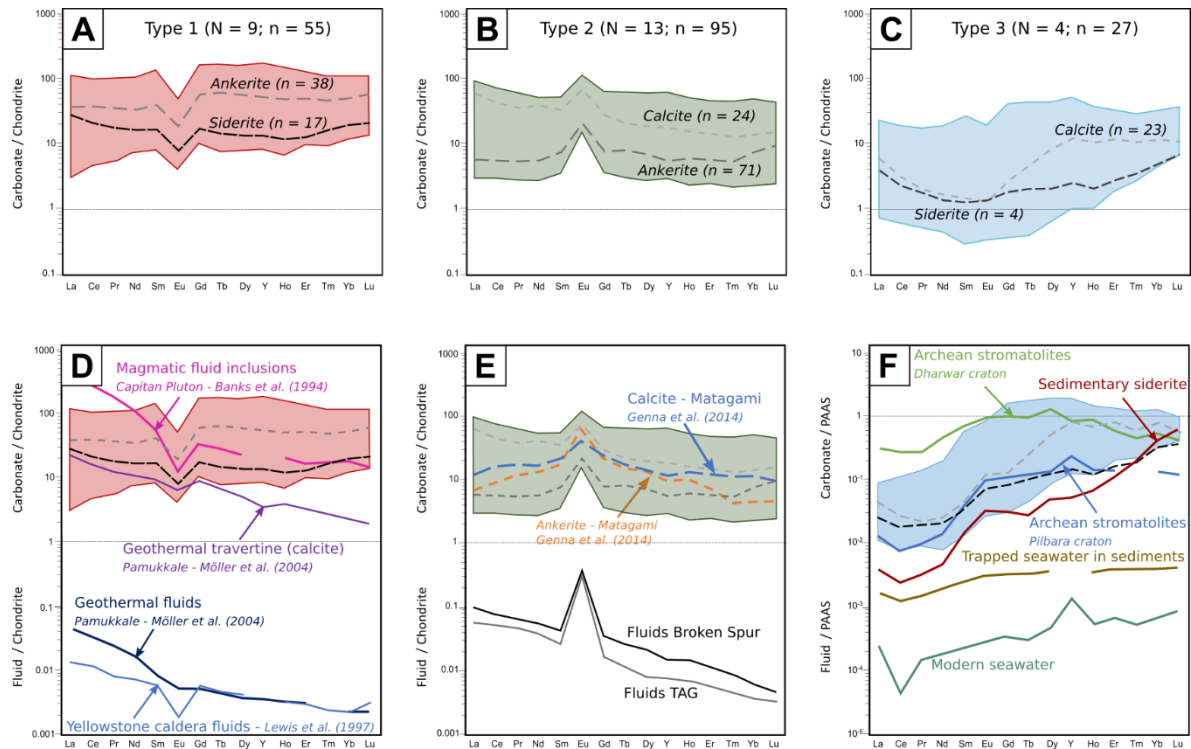
Figure 4.6: Normalized Rare-Earth Element and Y (REE+Y) diagrams of B26 carbonates. A. Type 1 carbonates, with median ankerite signal (dashed grey line) and median siderite signal (dashed black line). B. Type 2 carbonates with median ankerite signal (dashed dark grey line) and median calcite signal (dashed light grey line). C. Type 3 carbonates, with median calcite signal (dashed grey line) and median siderite signal (dashed black line). D to F Comparison of carbonate data from B26 (fields) with data from the literature. D. Type 1, data from magmatic fluid inclusions are from Banks et al. (1994), geothermal fluids and travertine from Pamukkale (Turkey) are from Möller et al. (2004), Yellowstone caldera fluid data are from Lewis et al. (1997). E. Type 2, carbonate data for Matagami are from Genna et al. (2014), data for Broken Spur and TAG fluids are from James et al. (1995), Mills and Elderfield (1995), James and Elderfield (1996) and Bau and Dulski (1999). F. Type 3, calcite data for stromatolites are from Khelen et al. (2019; Dharwar craton) and Van Kranendonk et al. (2003; Pilbara Craton), sedimentary siderites are from the Guelb Moghrein IOCG deposit (Mauritania, Sakellaris, 2007), trapped water in sediments data is from Haley et al. (2004) and modern seawater composition from Bau et al. (1997). The shaded areas correspond to the 10th and 90th percentile. Dashed horizontal line at 1 is for ease of reference. Detection limit is not shown on A to C, as it plots below the limits of the diagram. A to E are normalized to chondrite (Sun and McDonough, 1989) and F is normalized to Post-Archean Australian Shale (PAAS, Nance and Taylor, 1976)

36
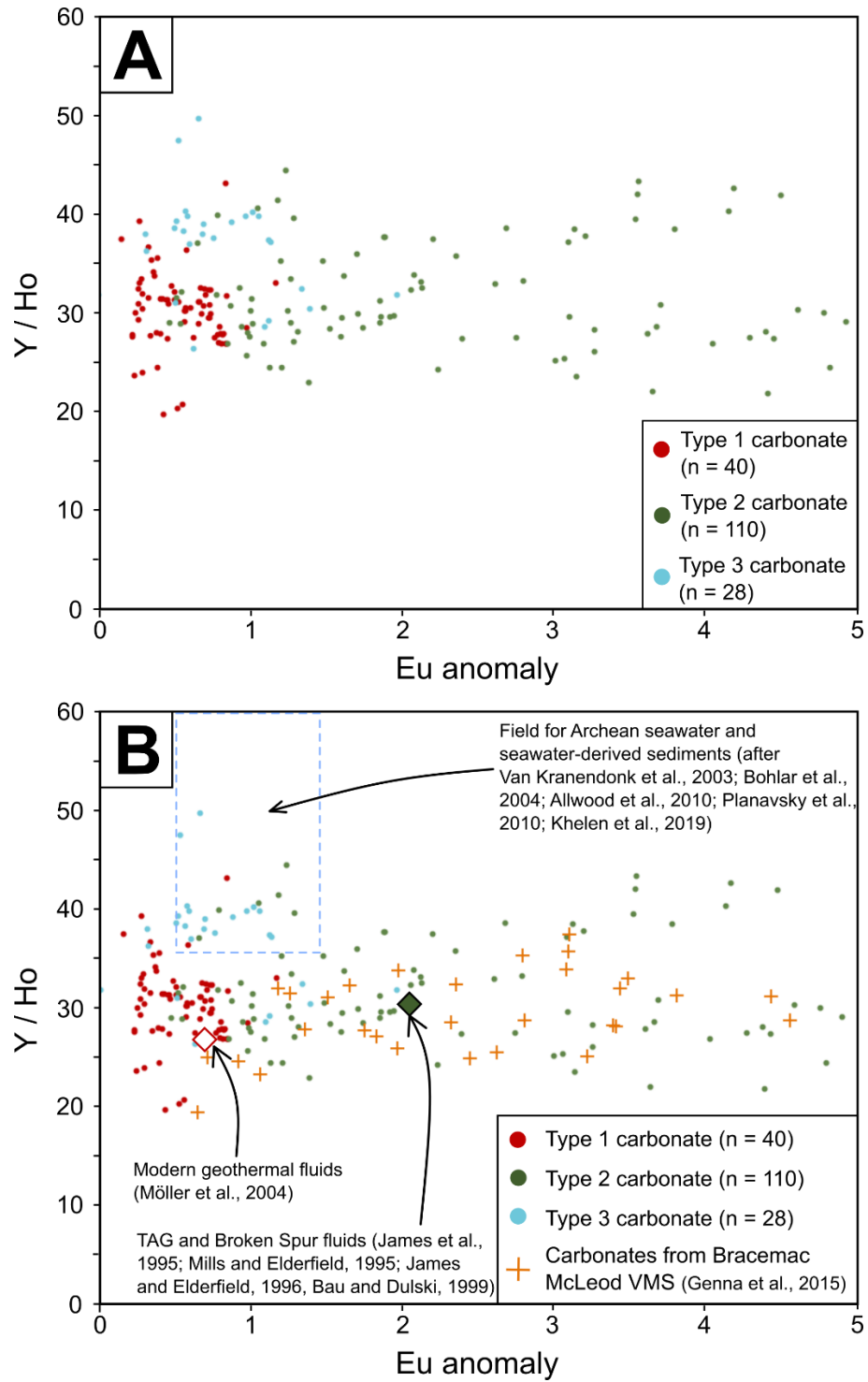
Figure 4.7: Binary diagrams (Eu anomaly vs Y/Ho) for discriminating Archean carbonates A.in the B26 area and B) comparing them with data from literature.
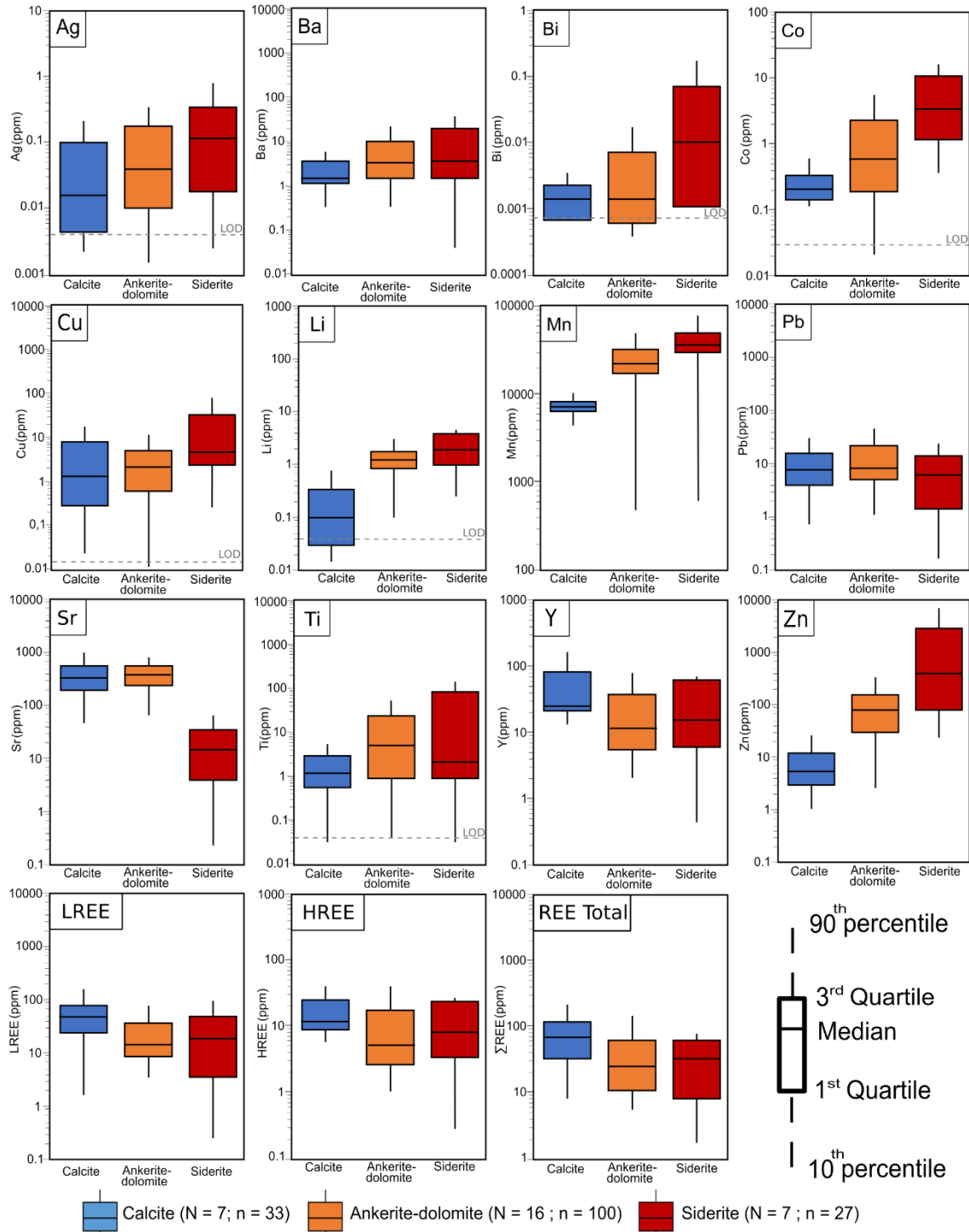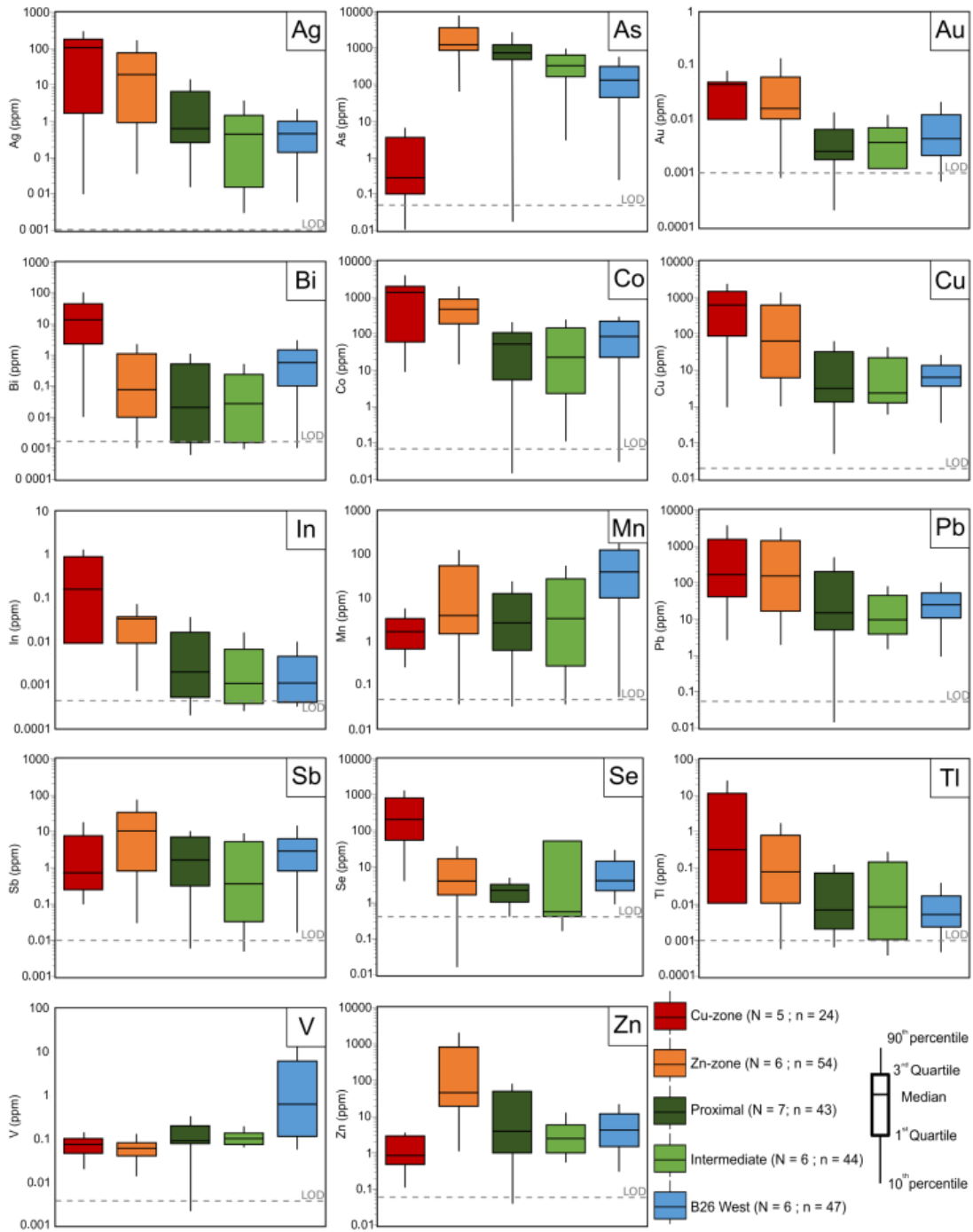
Figure 4.8: Box plot diagrams showing the variations of selected trace elements in pyrite at B26, according to their location in the mineralization or around the prospect, in the proximal (dark green) or intermediate (light green) carbonate alteration halo. B26 West corresponds to distal samples (3 to 6 km). Limit of detection (LOD) is represented by a light grey dash line. N = number of samples; n = number of analyses
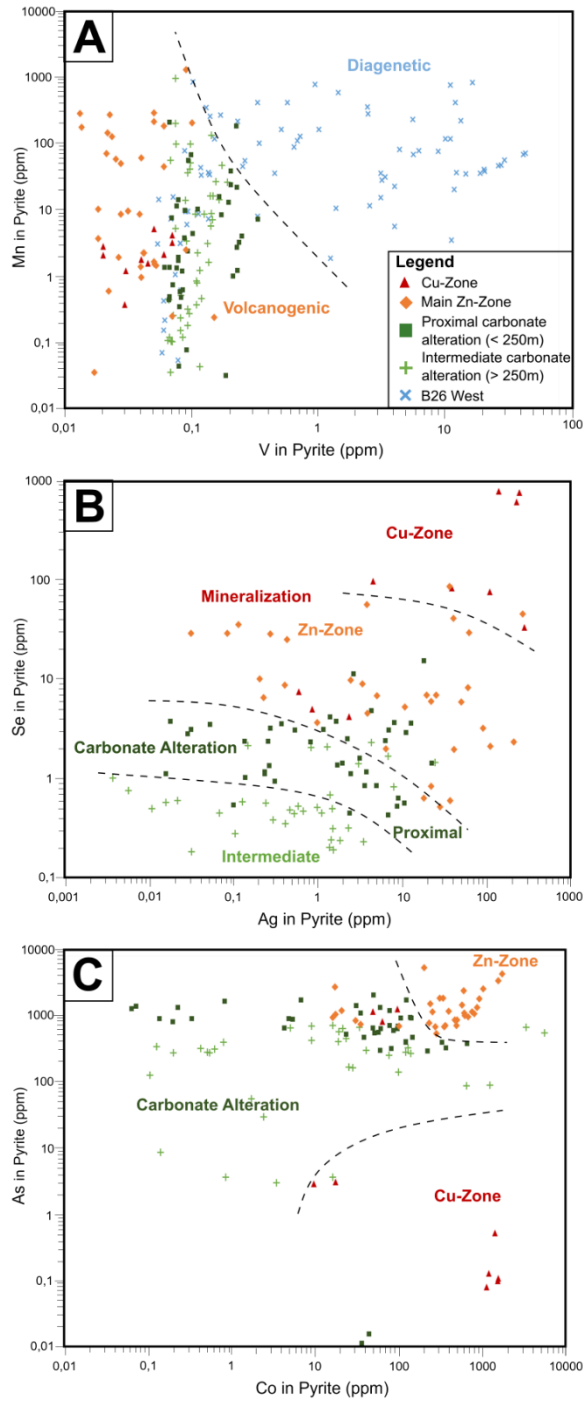
Figure 4.9: Binary diagrams of trace elements in pyrite, discriminating types of pyrite in B26. A. Mn vs V diagram separating volcanogenic and diagenetic pyrite. B. Se vs Ag and C. As vs Co diagrams for discriminating pyrites from the carbonate alteration (proximal and intermediate) and those from the mineralization in B26 (Cu-zone and Zn-zone)

39
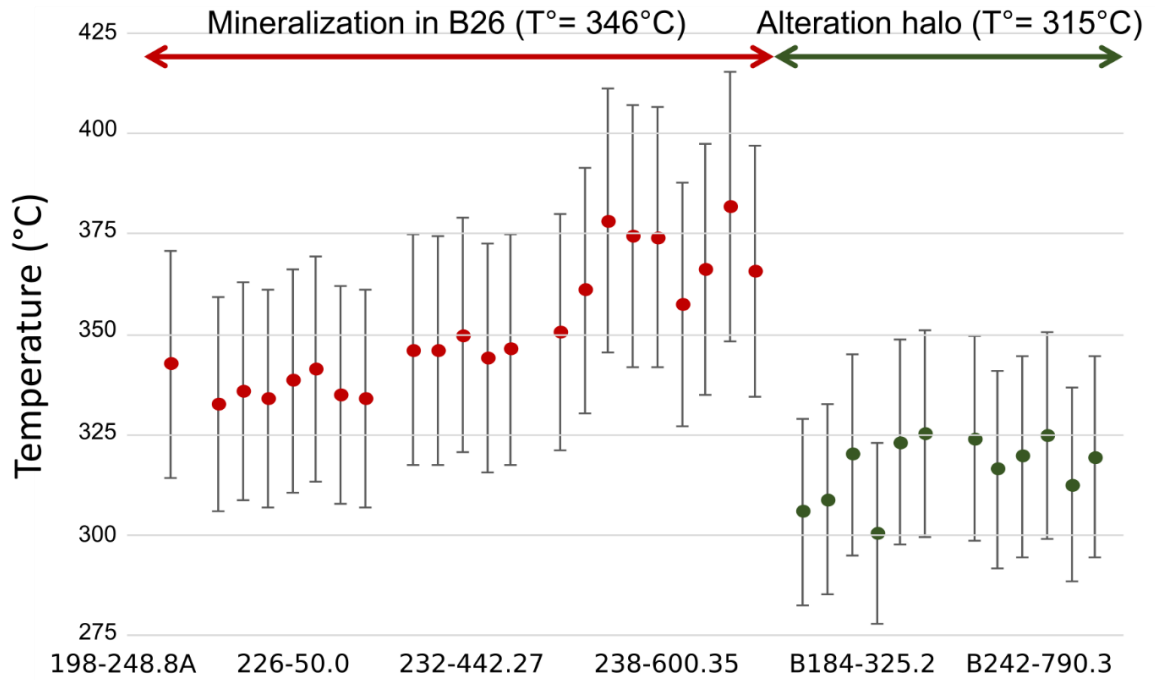
Figure 4.10: Histogram of temperatures (T°) calculated with the GGIMFis geothermometer of sphalerite (Frenzel et al., 2016) for B26 mineralization and proximal (B184-325.2) and intermediate (B242-790.3) carbonate alteration

**CHAPTER 5**

**DISCUSSION**


## 5.1 Origin of carbonates in Archean VMS environments


In an Archean greenstone belt, carbonates can have several origins: 1) volcanogenic (Morton and Franklin, 1987; Lafrance et al., 2000; Lafrance, 2003; Mueller et al., 2009), 2) biogenic, with the presence of stromatolites (Hofmann and Masson, 1994; Van Kranendonk et al., 2003), 3) diagenetic by the trapping of seawater in the pores of clastic or volcanogenic units (Veizer et al., 1989b; Rouchon et al., 2009), and 4) metamorphic, linked to the circulation of large amounts of metamorphic fluids through shear zones (Groves et al., 1987; Veizer et al., 1989a; Goldfarb and Groves, 2015). Below we show that mineral chemistry, supported by textural observations and whole-rock geochemistry, improves our understanding of the petrogenesis of the carbonate-bearing units in the Selbaie mining camp and its relation to the VMS mineralization at B26.


In the Selbaie mining camp, all 4 origins of carbonate could be possible. The B26 VMS mineralization formed above the calc-alkaline Brouillan Intrusive Complex and stromatolites have been previously identified in sedimentary carbonate units near the Selbaie mine (Hofmann and Masson, 1994; Taner, 2000). Stromatolites and Archean biogenic carbonates in general are mainly composed of calcite and dolomite (Veizer et al., 1990; Hofmann and Masson, 1994; Allwood et al., 2010). Diagenetic carbonates can form in porous marine sedimentary or volcaniclastic rocks saturated in seawater (Hein and Scholl, 1978; Haley et al., 2004). During diagenesis, this trapped fluid will lead to the crystallization of a variety of minerals, mainly oxides, sulfides or sulfates and carbonates (calcite, dolomite and siderite; Brooks et al., 1968; Haley et al., 2004; Smrzka et al., 2019 and references therein). Carbonate veins in deformation zones surrounding the Selbaie caldera, related to metamorphic fluids during the main deformation event (Lacroix, 1994), are common in the area. Metamorphic carbonates can have a wide variety of mineralogy, ranging from calcite to siderite

and magnesite, depending on the chemistry of the metamorphosed rocks (Veizer et al., 1989a). Thus first, it is necessary to decipher the origin of the stratabound carbonate alteration halo surrounding B26 VMS mineralization.

In the studied samples, the close connection between carbonate and other common VMS alteration minerals (chlorite, sericite, and pyrite: Figures 2.2, 2.3; Annex 2) indicates a genetic link between the volcanogenic hydrothermal activity and the formation of carbonate minerals. Cross-cutting relationships are sometimes observed between carbonate-altered units and carbonate-bearing veins, suggesting multiple carbonatation events, potentially tied to zone refining. Whole-rock geochemistry and normative calculations reveal the large scale of carbonatation surrounding B26 (Figures 4.2, 4.3). It is centered on the mineralization and continuous over several kilometers following the porous felsic tuffs.

Normative calculations also highlight two types of carbonatation in B26: 1) a moderate pervasive calcite-dominated alteration (5% normative calcite) under the footwall of B26 and, 2) an intense Fe-carbonate alteration (> 10% normative ankerite + siderite) focused in the hanging-wall. The calcite-dominated assemblage under the footwall is associated with non-leached units and could be linked either to the volcanogenic activity or the late metamorphism. On the other hand, the intense Fe-carbonate alteration, located in the hanging-wall, and its distribution, centered on the mineralization, and dimension highlighted by the normative calculations suggest that the carbonate and the mineralization are related (Figure 4.3b). The silicification documented by Fayard (2020) for the B26 deposit could have acted as a cap rock, which seals the system focusing the fluid flows and allowing carbonate to precipitate (Mueller et al., 2008). Similar size and zoning of carbonate alteration have also been documented in Mattabi-type VMS (Mattabi, Franklin et al., 1975; Groves et al., 1988; Normétal, Lafrance, 2003).

In order to decipher the origin of the carbonate alteration in Archean deposits (as volcanogenic or metamorphic in origin), Lafrance (2008) proposed a binary diagram with two indexes: the Carbonate Saturation Index ($CO_2/CaO+FeO+MgO+MnO_{molar}$) and the Carbonate Discrimination Index ($CO_2/CaO$; Figure 5.1). The Carbonate Saturation Index is a proxy for the intensity of carbonatation of rock samples and the Carbonate Discrimination Index is used to identify the dominant carbonate mineral, based on the Ca and $CO_2$ content. Lafrance (2008) created two fields on the diagram: i) the volcanogenic field, with an intermediate to intense Fe-carbonate-dominated alteration (Carbonate Saturation Index/Carbonate Discrimination Index > 0.25) and ii) the orogenic field, characterized by an intense carbonate alteration and dominated by Ca-bearing carbonate (Carbonate Saturation Index/Carbonate Discrimination Index < 0.25). The limit of the two fields was empirically established after a thorough statistical investigation on several databases of orogenic and VMS deposits in the Abitibi greenstone belt regrouping 24000 samples (Lafrance, 2008). For B26, among the 3580 analyses plotted on the diagram, the majority (62%) have a VMS signature (Carbonate Saturation Index/Carbonate Discrimination Index >0.25; Figure 5.1). These results are consistent with the examples tested by Lafrance (2008): samples from VMS in general have a volcanogenic signature ranging from 41 to 68%, whereas, for orogenic sectors tested in Abitibi, only 7 to 34% of the samples plot in the volcanogenic field. This is consistent with the observations made on the normative calculations and supports a volcanogenic origin for carbonate.

## 5.2   Carbonate trace element chemistry as a petrogenetic tool

In this study, mineral chemistry is used to constrain the nature of the fluids that created the carbonate-bearing units in and around B26 and to better understand their origin. The combination of carbonate, pyrite and sphalerite chemistry indicates a continuous volcanogenic signature for most of the samples from B26, but not for the distal samples from the B26 West transect.

The REE+Y patterns in carbonate minerals have been used in several hydrothermal deposits to highlight the evolution of the hydrothermal conditions (Mississippi-Valley type: Kontak and Jackson, 1995; Sedimentary Exhalative: Davies et al., 1998; Duan et al., 2017; VMS: Genna et al., 2015; Clastic-dominated massive sulfide: Rieger et al., 2021). Carbonates from B26 were divided into three types based on their REE+Y patterns (Figure 4.6).

## 5.2.1   Hydrothermal-magmatic origin of type 1 carbonates

Type 1 carbonates (siderite and ankerite), only present in the mineralization and its direct alteration halo, have distinct negative Eu anomalies, with relatively flat REE+Y pattern (Figure 4.6a, d). No carbonate minerals so far analyzed in VMS environments (Genna et al., 2014) or in active hydrothermal seafloor vents (Eickmann et al., 2009; Kendrick et al., 2022), have negative Eu anomalies. However, similar negative Eu anomalies have been documented in $CO_2$-rich fluids from subaerial calderas (Yellowstone, USA, Lewis et al., 1997; Valles Caldera, USA, Michard and Albarède, 1986) and geothermal springs (Pamukkale, Turkey; Möller et al., 2004) and, in a few cases, hydrothermal carbonates themselves from geothermal springs (e.g., calcitic travertine from Pamukkale, Turkey; Möller et al., 2004) and are shown for comparison in Figure 4.6a and d. On the Eu anomaly vs Y/Ho carbonate classification diagram, the geothermal springs from Pamukkale (Turkey, Möller et al., 2004) also plot within the type 1 carbonate field (Figure 4.7b). All of these environments are closely linked to a degassing magmatic intrusion, leading to $CO_2$-rich magmatic fluid flows. Magmatic fluid inclusions analyzed in the Capitan pluton (Banks et al., 1994; Figure 4.6d) also display systematic negative Eu anomaly. Negative Eu anomaly in magmatic fluids is probably inherited from the rhyolitic magma which typically have negative Eu anomalies due to crystallization of plagioclase incorporating all the divalent Eu (Sverjensky, 1984). Therefore, we interpret that negative Eu anomalies in hydrothermal fluids and carbonates can be linked to the presence of an active intrusion with volcanic degassing of $CO_2$, forming type 1 carbonates (ankerite and siderite). Moreover, the higher REE+Y content in type 1 carbonates in comparison to the one of the other carbonate types (Figure 4.6) suggests a signature more proximal to the source, as hydrothermal-

magmatic fluids are more enriched in REE+Y than seawater (Michard and Albarède, 1986). This is consistent with the presence of these carbonates in the direct vicinity of the Cu-zone at B26, which formed at high temperature and deep in the VMS system (Fayard et al., 2020a). Such signature can thus be used to identify active synvolcanic fault, directly connected to a subvolcanic intrusion, in a VMS district.

## 5.2.2   Volcanogenic origin of type 2 carbonates

Type 2 carbonate (ankerite-dolomite series with few calcite) are the most abundant in the alteration halo. They are associated with secondary Zn-zones and the upper ankerite-magnetite veins. Their signature is characterized by a positive Eu anomaly and a slightly fractionated REE+Y pattern (Figure 4.6b), as well as a low Y/Ho ratio (>35), which is very similar to the volcanogenic carbonates (calcite and ankerite) from the VMS deposits of the Matagami district (Figures 4.6e and 4.7b; Genna et al., 2014). Moreover, the general pattern of both the volcanogenic carbonates of Matagami and type 2 carbonates of B26 is similar to the REE+Y spectra of the carbonates (Eickmann et al., 2009) and fluids analyzed from modern seafloor hydrothermal systems, such as TAG or Broken Spur (Klinkhammer et al., 1994; Mitra et al., 1994; Mills and Elderfield, 1995; Bau and Dulski, 1999; Craddock et al., 2012). Also, the presence of these carbonates in the secondary Zn-zones and ankerite-magnetite veins located directly over the mineralization support a direct link with the mineralizing fluids. Thus, we interpret type 2 carbonate signature as hydrothermal/volcanogenic in origin. The presence of type 2 carbonates in the direct hanging-wall of the mineralization which extends all along the B26 transect, indicates a continuous volcanogenic signature for the carbonatation.

### 5.2.3 Diagenetic origin of type 3 carbonates

Type 3 carbonates (calcite and siderite) are much less abundant in B26 (only one sample), with a few more occurring in the B26 West transect. Their spoon-shaped, concave pattern, with a lack of an Eu anomaly, is unusual and unexpected for volcanogenic or hydrothermal carbonates (Figure 4.6c). However, this REE pattern is commonly documented in modern marine environments (Elderfield and Sholkovitz, 1987; Bau et al., 1999; Haley et al., 2004; Kim et al.; 2012; Smrzka et al., 2019) and in ancient marine sediments (Kamber et al., 2005; Sakellaris, 2007), including Archean stromatolites (Van Kranendonk et al., 2003; Allwood et al., 2010; Khelen et al., 2019) and banded iron formations (Bohlar et al., 2004; Planavsky et al., 2010). Stromatolites are often used as proxy for seawater-dominated environments and for ancient seawater composition (Van Kranendonk et al., 2003; Khelen et al., 2019). A LREE depletion, combined with a positive La anomaly and a high Y/Ho ratio is characteristic of Archean shallow seawater-derived sediments (Van Kranendonk et al., 2003; Kamber et al., 2004), with a variable Eu anomaly (Kamber et al., 2004). The Y/Ho ratio is a common tool for evaluating the importance of seawater in the formation of the unit: high Y/Ho values indicate an important seawater contribution, as modern seawater Y/Ho ratio (Y/Ho >60; Nozaki et al., 1997) is higher than the average upper crust (Y/Ho = 26; Kamber et al., 2005). Type 3 carbonates have a median Y/Ho ratio of 36, which is higher than types 1 and 2 carbonates (Y/Ho=30; Figure 4.7a), and significantly higher than the average upper crust. This ratio is similar to other carbonate data from Archean stromatolites, which have a range of Y/Ho values between 29 and 59 for stromatolites from Dharwar craton, India (Khelen et al., 2019), and slightly lower than the values reported by Kamber et al. (2004) for Mushandike carbonates, Zimbabwe, which range from 47 to 56 (Figure 4.7b). Type 3 carbonates thus have a typical Archean marine signature, comparable to that of Archean stromatolites (Figure 4.6f). Moreover, the high variability found in the REE+Y patterns in type 3 carbonates from B26, even in a single carbonate mass, could be indicative of continuous carbonate crystallization during diagenesis from trapped seawater-dominated fluids in the porous tuffs. Elderfield and Sholkovitz (1987) documented a high variation in the REE+Y patterns of the trapped fluids in marine sediments pores during the first centimetres of diagenesis, with a strongly marked

spoon-shaped pattern in the first few centimetres with a progressive flattening (due to enrichment in LREE) at 30 centimetres deep. A parallel can be made with the strongly fractionated core of the carbonate mass, and the more REE+Y-enriched borders with a flat pattern. Thus, we conclude that mineral chemistry shows that type 3 carbonate has a diagenetic origin with a strong influence of seawater chemistry and was formed, during diagenesis, by the seawater trapped in the pores of the volcanic tuff on the seafloor.

In summary, carbonate REE+Y chemistry has helped to understand better the origin of the carbonate-alteration at B26 and B26 west. We have shown, for the first time, that it is possible to differentiate the main fluids forming the carbonates: 1) hydrothermal-magmatic fluids forming type 1 Fe-carbonates during degassing of the Brouillan Intrusive Complex, 2) volcanogenic hydrothermal fluids (modified seawater) forming the abundance of type 2 carbonates of the carbonate alteration halo of the VMS mineralization and 3) seawater-dominated fluids trapped in sediments pores formed type 3 calcites and siderites.

## 5.3   Pyrite chemistry as a petrogenetic tool

The pyrite trace element data were plotted on a multi-element diagram, normalized to the Archean Sedimentary Pyrite (ASP, Figure 5.2; Genna, 2020; Gaboury et al., 2021). The diagram uses 20 trace elements commonly occurring in pyrite and was developed in order to characterize the nature of gold mineralization (orogenic, intrusion-related, VMS) in the Abitibi greenstone belt (Genna, 2020; Gaboury et al., 2021). The suite of elements is arranged in decreasing order of abundance for orogenic gold deposits (Genna, 2020). For VMS, this sequence of elements follows a decrease of temperature, with high-temperature elements (>350°C; Au, Co, Bi, Se, Te) on the left of the diagram and lower temperature elements on the right (Mn, Tl, Sb; Maslennikov et al., 2009; Genna, 2020). In this study, this multi-element diagram (Figure 5.2) is used to illustrate the signature of the B26 pyrites and the characteristics of the mineralizing fluids.

### 5.3.1 Volcanogenic origin of pyrite from B26 and its carbonate alteration

Figure 5.2a shows the trace element pattern of the different mineralized zones of B26 (Cu-zone, main Zn-zone, secondary Zn-zones) and the overlying barren ankerite-magnetite-biotite veins. Although many elements on the left of the diagram (Co, Se, Bi, Sn, In, As, Cu, Zn) shows variations over several orders of magnitude between the different ore zones, the 'M' shape pattern on the right side of the diagram, with positive peaks in Ag, Tl and Pb and a negative peak in W, is similar in all samples from B26 mineralization, including the overlying, late carbonate veins (ankerite-magnetite-biotite; Figure 5.2a). This 'M' shape pattern is thus characteristic of volcanogenic pyrite from the B26 VMS system. The pyrite pattern of the VMS mineralization of B26 is completely different to that of pyrite from orogenic gold, as defined by Genna (2020) and Gaboury et al. (2021), with much higher concentrations in semi-volatile (Se, Bi, In, Ag, Tl, Pb, Sb) or temperature sensitive metals (Co, Se, Ag: Figure 4.9a).

In detail, there is a progressive depletion in the concentration of semi-volatile elements (Co, Se, Bi, Cd, Ag, Tl, Pb) in pyrite along the different zones of the B26 deposit: pyrite from the Cu-zone is the most enriched, followed by the main Zn-zone, the secondary Zn-zones with pyrite from the ankerite-magnetite-biotite veins in the hanging-wall having the lowest concentrations (Figure 5.2a). Most of the elements enriched in pyrite from Cu and Zn mineralization of B26 (Co, Se, Bi and In) are known to be linked to high-temperature mineralization in VMS and seafloor hydrothermal systems (Huston et al., 1995; Maslennikov et al., 2009; Genna et Gaboury, 2015; Grant et al., 2018). Selenium is controlled by temperature in VMS systems (Auclair et al., 1987; Hannington et al., 1999; Layton-Matthews et al., 2008; Genna et al., 2015). Thallium is highly volatile and usually characteristic of low-temperature mineralization (Huston et al., 1995; Maslennikov et al., 2009; Genna and Gaboury, 2019), but its enrichment in pyrite is typical of an acidic hydrothermal environment, commonly found in epithermal deposits (Steadman et al., 2021) and in Zn-rich parts of VMS deposits (Genna and Gaboury 2015; Soltani-Dehnavi et al., 2018). A key aspect is the progressive decrease of some elements concentrations (Co, Se, Bi, In, Ag, Tl, Pb) following the diminution of the temperature and

the distance to the source of the fluids: pyrite from the warmer and deeper Cu-zone is the most enriched in these elements, with a progressive depletion in their concentration in pyrite to the later main and upper Zn-zones and uppermost ankerite-magnetite-bearing veins which are the most depleted (Figure 5.2a).

The signature of the pyrite from the proximal and intermediate carbonate-alteration halo of B26 is similar to the signature of pyrite associated with B26 secondary Zn-zones and ankerite-magnetite veins, which are both depleted compared to that of the main mineralization (Figure 5.2a, b). The two patterns are similar, the 'M' shape is still present at the end of the signal formed with positive anomalies in Ag, Tl, Pb and Sb and a negative anomaly in W (Figure 5.2b). The only difference between pyrites from proximal and intermediate samples is the abundance of elements, proximal pyrites are slightly more enriched in all the trace elements, except Au and Te. Both signals are slightly depleted in comparison to Archean sedimentary pyrites, only As and Ag are at the same levels (Figure 5.2b). The 'M' shape of the pattern is less strongly marked in the pyrites from the alteration halo than in the mineralization. A progressive depletion of Co, Se, Bi, In, Ag, Tl and Pb is observed, in one hand, between pyrites from the mineralization and the alteration halo and on the other hand within the alteration samples, between proximal and intermediate pyrites (Figure 5.2a, b).

This suite of elements is the same as the ones controlled by the temperature in B26 mineralization, which is consistent with the temperature calculated using the sphalerite geothermometer showing a slightly lower temperature in the alterations (315°C) than in the mineralization (346°C). It has been documented that pyrite composition records the evolution of the forming hydrothermal fluids chemistry (Large et al., 2007; Reich et al., 2013; Genna and Gaboury, 2015). Consequently, the vertical and lateral variations of the pyrite composition in and around B26 reflect the evolution of the hydrothermal fluids. The progressive depletion in trace elements and the dilution of the volcanogenic signature is a sign of an evolving fluid, flowing away from the mineralization. Thus, pyrite from

proximal and intermediate samples have a volcanogenic origin and records the evolution of the hydrothermal fluids.

The pyrite from the B26 mineralization, especially the Cu-zone, is enriched in semi-volatile (Se, Bi, Sn In, Cu, Ag, Tl, Pb) and magmatic elements (Co, Se, Bi, Sn, In, Cu, Ag). Enrichment in semi-volatiles is observed in other VMS deposits or volcanogenic mineralization in the Abitibi (Bracemac McLeod: Genna and Gaboury, 2015; Horne 5: Krushnisky et al., 2023; Perron: Gaboury et al., 2021). Most of these semi-volatile elements, especially Bi, Cu and Tl, could be interpreted to be linked to a magmatic input in the hydrothermal fluids of VMS deposits and modern submarine hydrothermal vents (Keith et al., 2016; Maslennikov et al., 2017; Genna and Gaboury, 2019). This hydrothermal-magmatic contribution is consistent with the chemistry of type 1 carbonates (magmatic degassing signature) observed in the mineralized zones and the associated intense leaching alteration. The enrichment in semi-volatiles, as found in pyrite from the B26 Cu-zone, is often linked to the surface expression of an underlying degassing intrusive (Spooner, 1993; Azevedo et al., 2022). The large difference of Bi content of pyrite between the Cu-zone and the Zn-rich mineralization could highlight the progressive dilution of the magmatic signature, showing the evolution of the fluid towards the more classic VMS signature, with a growing importance of modified seawater, leading to the formation of type 2 carbonates in the upper mineralized zones.

### 5.3.2 Diagenetic origin of pyrite from B26 West

Pyrite from the most distal samples (3.5-6.5 km) from the B26 mineralization (B26 West transect) generally have a different trace element pattern (Figure 5.2c). The signal, normalized to Archean sedimentary pyrite, is relatively flat and missing the 'M' shape characteristic of pyrite from B26 VMS system. However, the overall signal is close to the Archean sedimentary pyrite pattern (Figure 5.2c) except for a positive anomaly in Mn. The Mn concentration in pyrite from B26 West is correlated with Ca and Mg, suggesting micro-inclusions of carbonate, as observed in some thin sections (Figure

2.3a-d). The high Mn content in pyrite is typically considered characteristic of diagenetic or sedimentary processes (Shikazono et al., 1994; Gregory et al., 2015). Pyrite from B26 West are also the most enriched in V (Figure 4.9). Haase et al. (2024) reported that FeS is the most efficient sorbent for V in anoxic seawater. Most V from seawater will then enter sedimentary pyrite. Moreover, V is more abundant in seawater than in submarine hydrothermal springs (Wheat et al., 2002). Such high V concentrations in pyrite, coupled with Mn from carbonate micro-inclusions, could indicate a sedimentary origin of pyrite with an important contribution of seawater in its formation. The porous texture of the pyrites in the B26 West transect (Figure 2.3h), as well as and the absence of framboidal, nodular or fine-grained pyritic mass, however, is not characteristic of a pure sedimentary origin (Raiswell and Plant, 1980; Thomas et al., 2011; Gregory et al., 2015). Instead, the flat trace element pattern of pyrite, similar to that of Archean sedimentary pyrite except for enrichments in Mn and V, coupled with the presence of diagenetic (type 3) carbonates in B26 West samples suggest an important marine sedimentary contribution to the formation of carbonate-rich units in this sector. The high Mn content in pyrite also suggests that both carbonates and pyrite precipitated during diagenesis from pore water trapped in volcanic tuffs distal from the B26 mineralization.

## 5.4   Formation of volcanogenic carbonates in a VMS environment

The formation of a large-scale (plurikilometer), stratabound carbonate alteration halo surrounding the B26 VMS mineralization, as observed in the Selbaie mining camp, implies an important source of $CO_2$ that could be linked to the volcanogenic activity. Studies on active volcanoes have shown that calc-alkaline volcanic activity is responsible for the degassing of large amounts of $CO_2$ in the atmosphere but also within the surrounding rocks (Allard et al., 1991; Etiope et al., 1999; Epiard et al., 2017). In some cases, subsurface $CO_2$ has been measured up to 2km away from the crater, with the highest diffusion along the faults or the most porous units, such as volcanic tuffs or breccias (Etiope et al., 1999; Epiard et al., 2017). Experimental studies conducted by Gysi and Stefansson (2012) and Kumar et al. (2017) have shown that reactions between continuous $CO_2$ degassing and

volcanic rocks can form calcite, ankerite, dolomite and siderite. Formation of volcanogenic calcite and aragonite by replacement of a porous unit has been documented by Pichler and Dix (1996) and Pichler and Veizer (2004) near the submarine hydrothermal vents of Tutum Bay (Papua New Guinea). They explain the formation of carbonate by the mixing of a $CO_2$-rich fluid from the degassing of an underlying intrusion with seawater. Flows of hydrothermal-magmatic $CO_2$-rich fluids would flow preferentially through major synvolcanic fragile faults which enhance the porosity of the host rock, leading to the crystallization of volcanogenic carbonates. These features are also characteristic of Mattabi-type VMS environments, as described by Morton and Franklin (1987).

## 5.5 Volcanogenic Model for the formation of stratabound carbonate-alteration of the B26 VMS deposit

The Selbaie mining camp is centred around the Brouillan Intrusive Complex, which is a calc-alkaline synvolcanic intrusion displaying thick piles of felsic to intermediate volcaniclastic-dominated units (Sinclair, 1977; Lacroix, 1994; Faure et al., 1996). It has been described as an Archean caldera environment (Larson and Hutchinson, 1993; Taner, 2000; Mueller et al., 2009). The Selbaie area share similitudes with Mattabi-type VMS environment, with shallow water characteristics, marked by the presence of stromatolites, epithermal mineralizations in Selbaie, associated with thick volcaniclastic piles (Faure et al., 1996; Taner, 2000; Fayard, 2020). A shallow water environment allows the formation of hydrothermal carbonates around the volcanogenic mineralization of B26 (Fayard et al., 2020b) and the VMS-epithermal mineralization of Selbaie (Faure et al., 1996) and along the interpreted synvolcanic faults (Faure, 2012; Figure 5.3a).

The combination of geochemical methods used in this study helped to decipher the origin of the fluids involved in the formation of the carbonates. Alteration at B26 shows two main different patterns: the footwall is intensely leached, with minor carbonate, whereas the hanging wall is dominated by Fe-carbonates all along the B26 transect (Figure 4.2; 5.3b). These two different alterations imply a

difference in the chemistry of the hydrothermal fluids involved. Moreover, the distal B26 West transect exhibits a different geochemical behavior dominated by seawater.

### 5.5.1 Hydrothermal-magmatic fluids

The leaching in the footwall, characterized by a high Spitz-Darling Index (> 100) and a diminution of the Eu anomaly, indicates an acidic fluid, altering the plagioclase to form chlorite, sericite and minor carbonates (Figure 5.3b). The presence of hydrothermal-magmatic- type 1 carbonates in and around the mineralization is in agreement with the lithogeochemistry. The footwall would have been preferentially altered by hot, acidic magmatic fluids, forming minor type 1 carbonates. The low proportion of carbonate observed in the proximal footwall (Figure 4.3a) is probably linked to its proximity to synvolcanic structures, which focus the fluids flow. The continuous fluid flow through synvolcanic structures, probably during zone refining, could have inhibited the crystallization of the carbonates or could have forced a constant recrystallization of the previously formed carbonates in these units. The reuse of the main conduits in B26 is also interpreted as the origin of the secondary Zn-zones, and the ankerite-magnetite veins in B26 (Fayard et al., 2020a). Further away from these structures, less fluid flow would have preserved the intense carbonate alteration. The chemistry of the hydrothermal-magmatic fluids is particularly witnessed in the pyrite trace element composition. The enrichment in semi-volatile and/or magmatic elements (Co, Se, Bi, TI) in pyrite from the mineralization, and the progressive decrease of these elements with distance to the source of the fluids (Figure 5.3b), indicates a magmatic origin of the mineralizing fluids, with a calculated temperature of 350°C using the geothermometer on sphalerite.

### 5.5.2 VMS fluids

The hanging-wall is intensely altered with carbonates, with minor leaching. The alteration fluids are more likely $CO_2$-saturated neutral fluids. The spatial correlation between the highest carbonated

units and an increase in the Zn concentrations (Figure 4.3) could indicate that carbonate deposition was linked to a mixing between hydrothermal fluid flows and seawater-saturated porous units, increasing the pH and saturating the fluid in $CO_2$ (Bourcier and Barnes, 1987; Franklin et al., 2005), which lead to the deposition of carbonate. The presence of type 2 carbonates in the hanging-wall, with a positive Eu anomaly, interpreted volcanogenic as it is common in other VMS settings, is coherent with a mixing of the $CO_2$-rich fluids with modified seawater. Moreover, the pyrite trace element signature found in the hanging-wall (secondary Zn-zones, ankerite-magnetite veins and carbonate alteration), resembles that of the B26 mineralization but remains depleted in semi-volatile elements. Thus, secondary mineralization and carbonate-altered units have a continuous volcanogenic signature which is progressively diluted with increasing distance from the mineralization (Figure 5.3b). This dilution is also shown by a decrease of 30 to 50°C between B26 mineralization and the carbonate alterations, using the geothermometer on sphalerite.

### 5.5.3   Seawater

Macro- and microscopically, carbonate units from the B26 West transect resemble that of B26, with no textural differences in the carbonates nor the pyrite. However, trace element geochemistry indicates that seawater was the dominant fluid in the area. The presence of type 3 carbonate, with a concave REE+Y pattern and a high Y/Ho ratio (Y/Ho = 36), similar to that of calcite of Archean stromatolites, as well as Mn and V-rich pyrites, indicate a diagenetic origin for the carbonated units (Figure 5.3b). The distal porous volcaniclastic rocks were saturated in seawater, which precipitated carbonates and pyrite during diagenesis. Diagenetic carbonate alteration of volcaniclastic rocks was documented in recent units by Hein and Scholl (1978). The minor influence of hydrothermal-magmatic and volcanogenic fluids is consistent with the location of the transect, far from the Brouillan Intrusive Complex, the source of the fluids (Figure 5.3a).

## 5.6　Implications for exploration of Mattabi-type VMS

### 5.6.1　Using carbonates as a vectoring tool?

Historically, zoning in the carbonate alteration defined by Morton and Franklin (1987), with proximal siderite, intermediate ankerite-dolomite and distal calcite, has been used for the exploration of VMS deposits (Lafrance, 2003; Mueller et al., 2008). At B26, this geometry is present, highlighted by the normative calculations (Figures 4.2-4.3), this distribution can be used as a vector for the mineralization. However, mineralogical zoning of the carbonates only gives thresholds for mineral exploration with no precise vector within each zone. Still, some classic vectors for VMS can be applied to carbonate-altered VMS, such as using Mn concentrations in whole-rock analyses, as Mn is widely influenced by carbonate, but also possibly by chlorite, epidote and allanite (Hannington et al., 2003; Maslennikov et al., 2012). At B26, Pearson correlation coefficients (r) shows that the MnO content in whole-rock analyses is highly correlated with normative calculations of ankerite (r = 0.36), siderite (r = 0.70) and rhodochrosite (r = 0.88) and shows very little correlation with calcite (r = 0.04) and dolomite (r = 0.14; Electronic Supplementary Material - S12). It indicates a link between MnO and an intense Fe-carbonate alteration. Manganese is thus a proxy for the mineralogy of the carbonate present in the rock, in B26. However, normative calculations for carbonates are based directly on the $CO_2$ content of the rock and provide more precise estimations of the carbonatation, as it is less influenced by other mineral phases (Trépanier et al., 2015). Lafrance (2003) also proposed a possible vector directly developed for Mattabi-type VMS mineralization in the Normétal area, based on the major elements of the ankerite-dolomite series, with an increase of the Mg/Fe ratio closer to the mineralization. This tool was tested for B26 and does not work to vector to the mineralization. However, the current sampling was restricted by the availability of drill holes and did not allow to document the lateral extent of the ankerite-dolomite halo, so additional samples would be needed to fully test the tool. Nevertheless, the evolution of REE+Y pattern in carbonates from type 3 (distal) to type 2 (proximal-intermediate) and type 1 (directly in the mineralization) could provide a guide for exploration.

### 5.6.2   Using pyrite as a vectoring tool

Pyrite chemistry can also be used for mineral exploration of Archean VMS, as demonstrated for pyrite in the volcanic tuff (Key Tuffite) of the Bracemac-McLeod deposit, Matagami in Abitibi by Genna and Gaboury (2015). There they used the increase of the semi-volatile metal (Sb, Tl) contents in pyrite to vector towards the mineralization.

At B26, the mineralization is formed by replacement of porous volcaniclastic units (Fayard, 2020). Hydrothermal fluid flows are focused vertically on the main structures and laterally along the most porous units. We have demonstrated that both carbonates and pyrite occurring in and around the mineralization (type 1 carbonate and pyrite from the Cu-zone) record the contribution of hydrothermal-magmatic fluids. For the pyrite, it contains an abundance of hydrothermal-magmatic semi-volatile elements (Bi, Se, Ag, Tl). Vertically, within B26, there is a gradual depletion of these elements, following both the temperature and the evolution of the fluid. The same patterns are observed laterally. Box plot diagrams on Figure 4.8 highlight a wide list of elements which display the same progressive depletion from the mineralization to the most distal altered units (Ag, As, Bi, Co, Cu, In, Sb, Se, Tl). The use of semi-volatile elements has already been highlighted as potential effective vectors for VMS deposits for the Bracemac McLeod VMS deposit in Matagami, using both pyrite (Genna and Gaboury, 2015) and whole-rock geochemistry (Genna and Gaboury, 2019). For B26, Se, Ag and As content of pyrite are the most effective tools for exploration as they increase towards the mineralization (Figure 5.4) and provides better results than whole-rock data for the same elements (Annex 6).
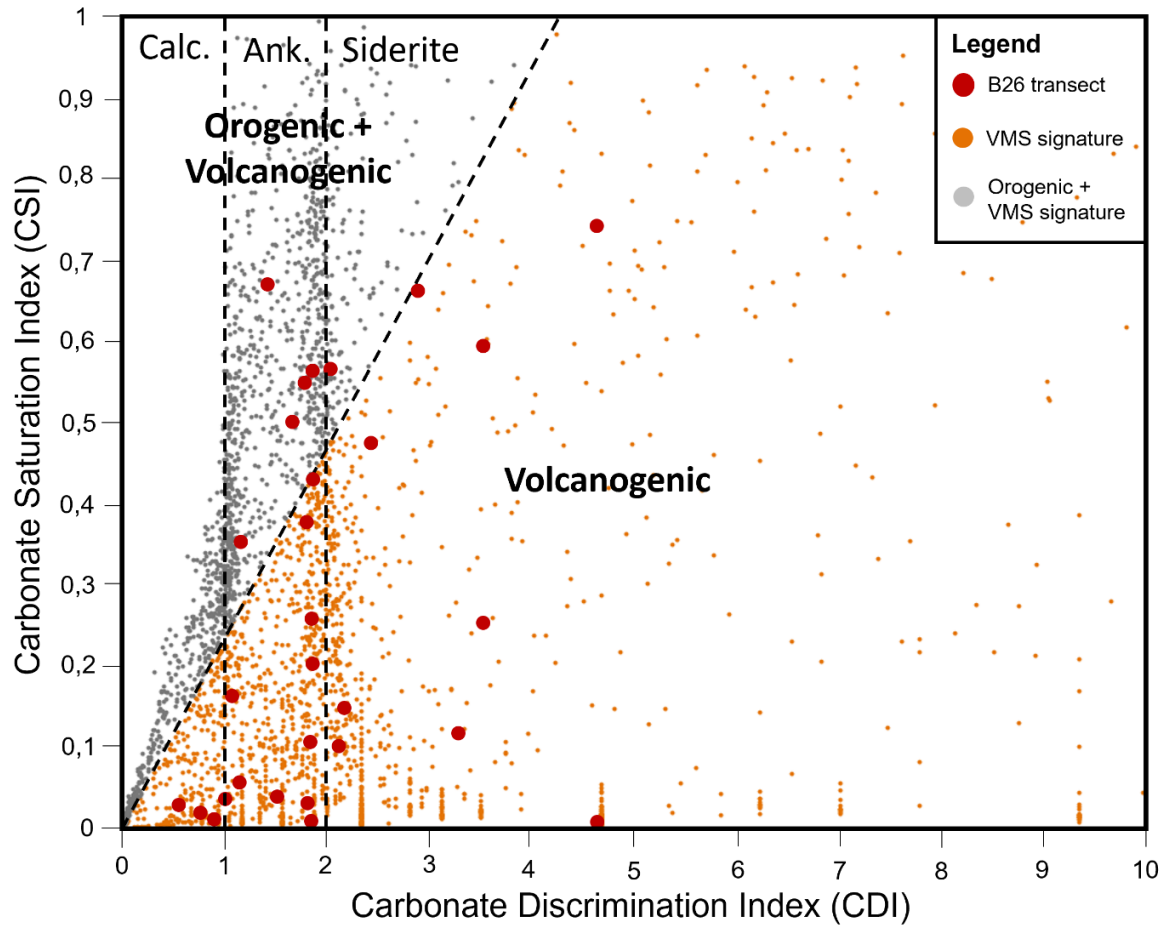
Figure 5.1: Carbonate Saturation Index ($CO_2$/CaO+MgO+FeO+MnO) vs Carbonate Discrimination Index ($CO_2$/CaO) diagram to determine the origin of carbonate alteration in Archean greenstone belts (Lafrance, 2008; Number of analyses = 3580)
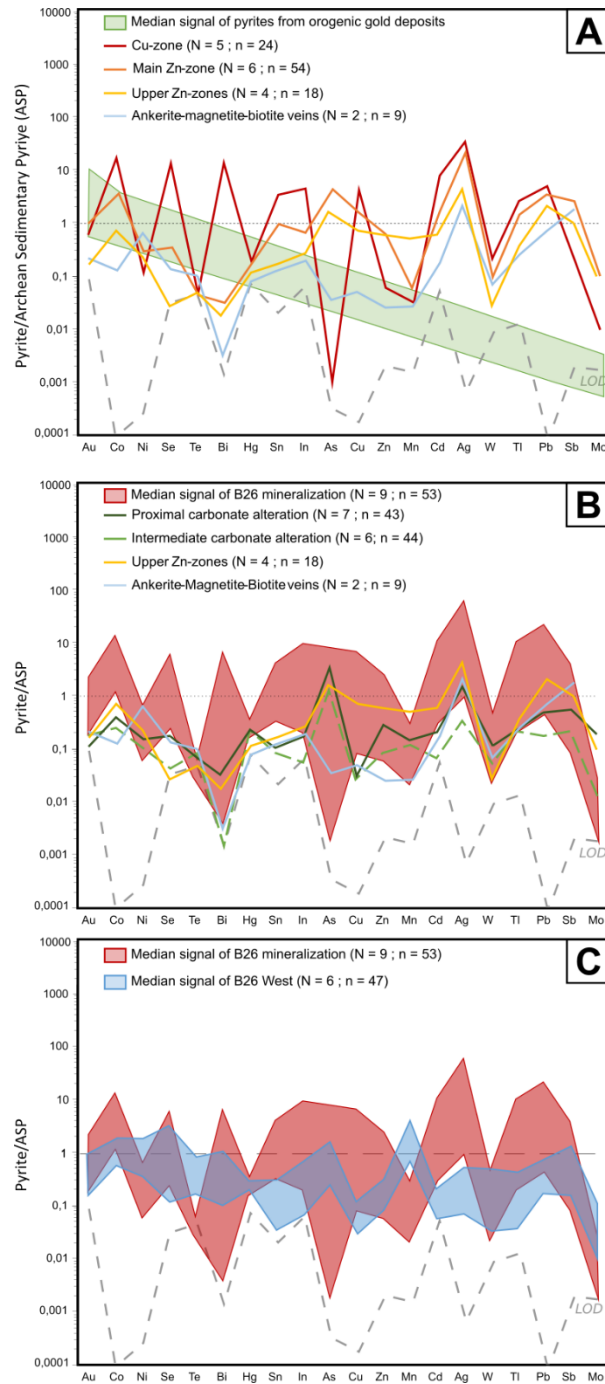
Figure 5.2: Multi-element diagram of trace elements in pyrite, normalized to Archean Sedimentary Pyrite (ASP) after Genna (2020). A. Pyrite from B26 mineralization, combining data from this study and that from Fayard (2020), compared to median pyrite data from orogenic gold deposits in Abitibi (green field: Gaboury et al., 2021). B.Pyrite from proximal (dark green) and intermediate (light green) carbonate alteration at B26 compared to the pyrite signal of B26 mineralization (Cu-zone, main Zn-zone and secondary Zn-zones, the red shape corresponds to the 25th and 75th  centiles). C. Pyrite from distal carbonate alteration, from B26 West transect, compared with pyrite from B26 mineralization.
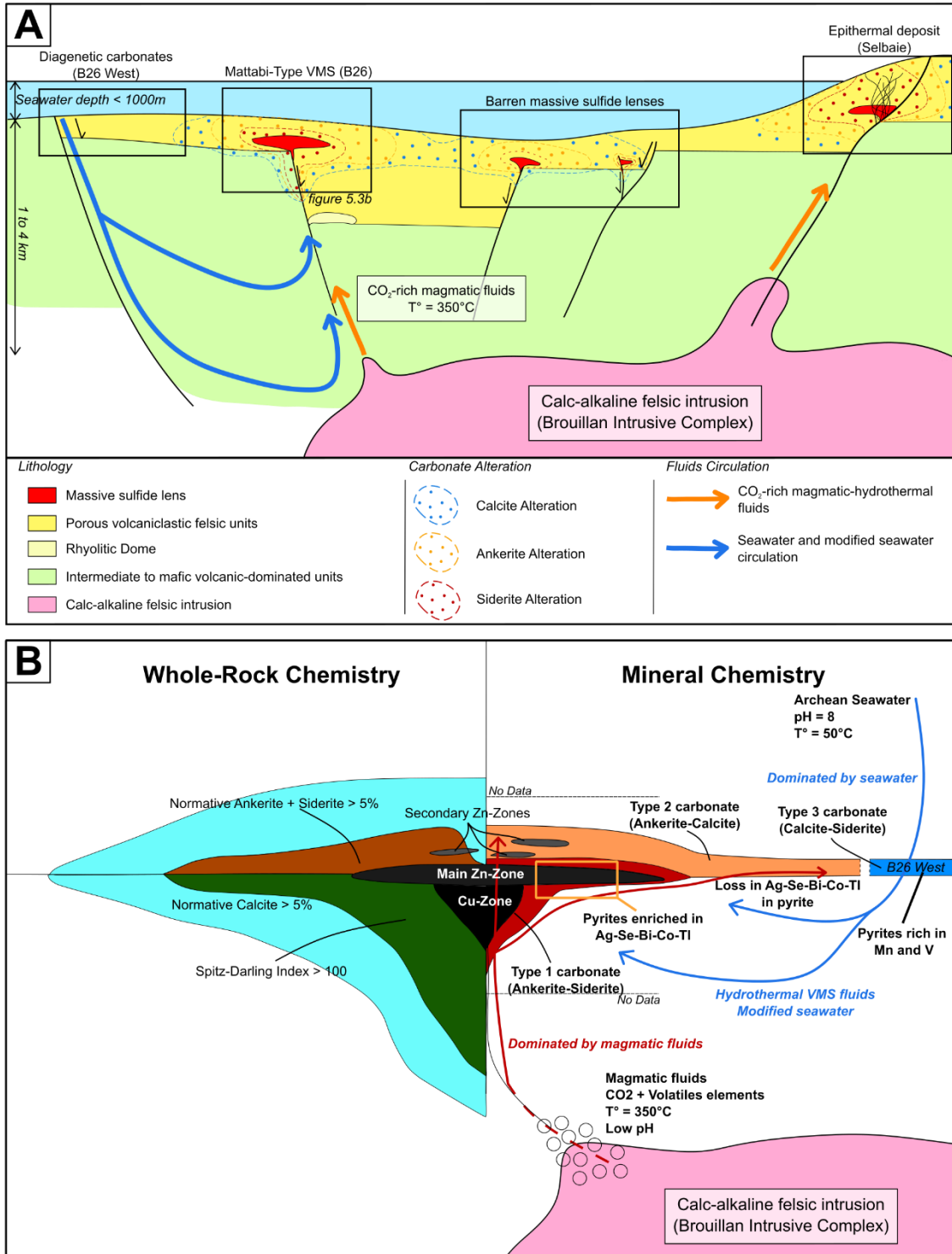
Figure 5.3: Genetic model for B26 VMS mineralization and carbonate alteration. A. Regional schematic representation of the Selbaie caldera, with its volcanogenic minerlization and ditribution of carbonate alteration. B. Geochemical synthesis of the alteration in and around the B26 prospect. See text for explanation
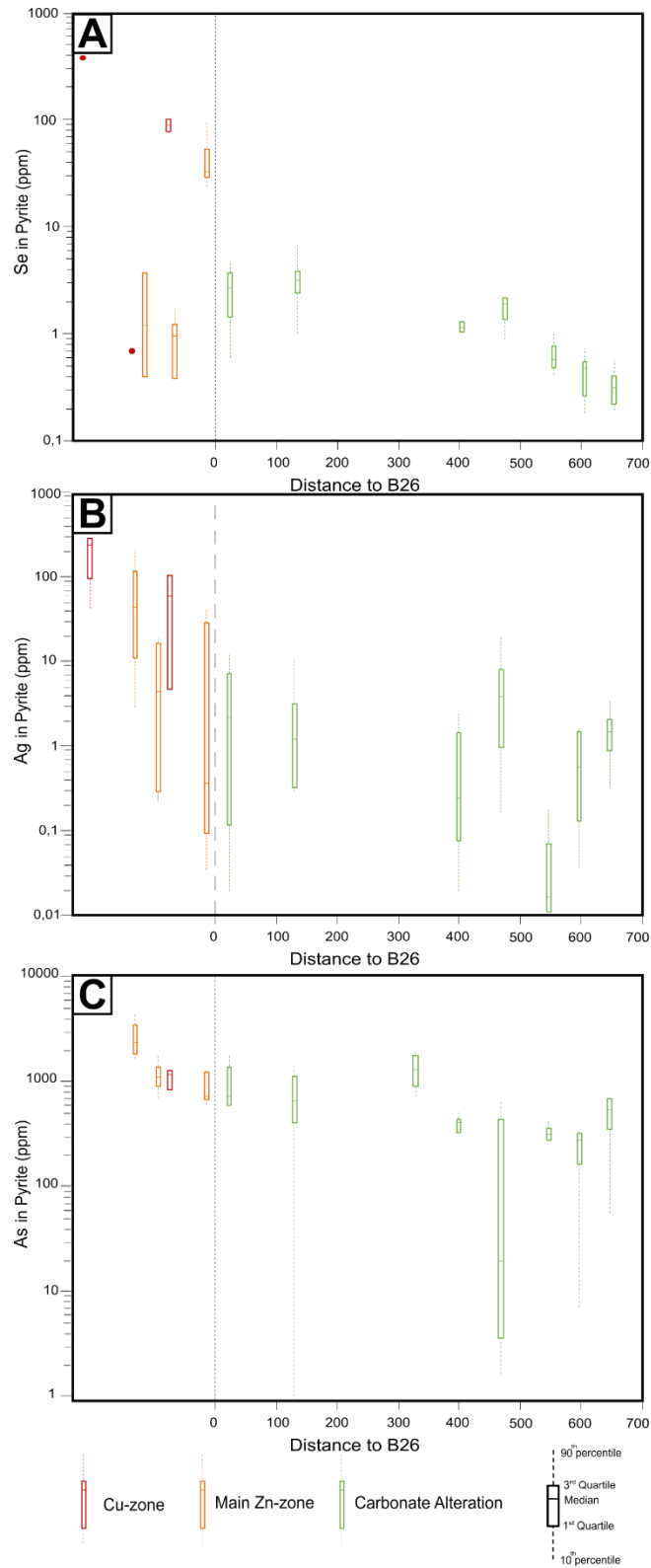
Figure 5.4: Binary diagrams of Se, As and Tl content of pyrite in carbonate alteration as a function of distance towards B26 mineralization, highlighting possible vectors for exploration

# CHAPTER 6

# CONCLUSION

The B26 prospect displays classic characteristics of Mattabi-type VMS environment, comparable to Mattabi (Franklin et al., 1975; Groves et al., 1988) or Normétal (Lafrance, 2003). The extensive semi-conformable carbonate alteration follows the most porous units (rhyolitic tuffs) and is zoned with siderite centered on the mineralization surrounded by a large ankerite-dolomite halo and with calcite in the uppermost and lowermost units. Even though carbonate alteration exhibits a wide range of textures and its intensity varies along the B26 transect, it is systematically associated with other common VMS alteration minerals (pyrite, chlorite, sericite). The geometry and the textural characteristics of the carbonate alteration in B26 suggest a cogenetic link between carbonates and the volcanogenic activity.

The combination of LA-ICP-MS trace element chemistry of carbonates and pyrite is an efficient tool for constraining the fluid chemistry involved in the carbonatation in B26 and Mattabi-type VMS deposits. Carbonate REE+Y diagrams can distinguish 3 types of fluids involved in forming the carbonate alteration at B26: 1) hydrothermal-magmatic fluids in and around the mineralization, 2) VMS-type fluids and 3) seawater, with the occurrence of diagenetic carbonates in B26 West. Although type 2 carbonates are similar to those observed in other VMS and hydrothermal vents, the presence of purely hydrothermal-magmatic carbonates associated with the mineralization in VMS has never been documented before, proving a direct link with an underlying synvolcanic pluton.

Pyrite chemistry was used to determine the signature of the B26 mineralization and compare it to the carbonate alteration halo. Pyrite from B26 mineralization is enriched in semi-volatile (Se, Ag, Bi, Tl) and temperature-dependent (Co, Se) elements and those in carbonate alteration halo from the B26 transect show a similar signature, although slightly depleted in most trace elements. However, pyrite of the B26 West transect exhibits a different trace element content, characterized by high Mn

and V content, often associated with sedimentary pyrites. All these elements were used to build binary diagrams useful for discriminating pyrites from the different locations in and around B26: mineralization, carbonate alteration halo and non-volcanogenic pyrites. The integration of both carbonate and pyrite analyses emerges as a robust petrogenetic tool, confirming the volcanogenic origin of the carbonate-altered units across the 1km-long B26 transect and distinguishing it from the diagenetic origin of the carbonates from the B26 West transect.

This multi-disciplinary approach provides new insights for the comprehension of the formation of volcanogenic carbonates, with the importance of $CO_2$-degassing from an underlying intrusion. This study also demonstrates the potential of using these easily detectable, large-scale carbonate-altered units for the exploration of volcanogenic mineralization. The REE+Y content of type 1 carbonate, with a negative Eu anomaly, indicates proximity to the ore zone and by the progressive enrichment of semi-volatile elements in pyrite (Ag, Se, As) can vector towards the mineralization in B26.

# REFERENCES

Acocella, V. (2007). Understanding caldera structure and development: An overview of analogue models compared to natural calderas. Earth-Science Reviews, 85(3-4), 125-160. https://doi.org/10.1016/j.earscirev.2007.08.004

Allard, P., Carbonnelle, J., Dajlevic, D., Le Bronec, J., Morel, P., Robe, M. C., Maurenas, J. M., Faivre-Pierret, R., Martin, D., Sabroux, J. P., & Zettwoog, P. (1991). Eruptive and diffuse emissions of $CO_2$ from Mount Etna. Letters to Nature, 351, 387-391.

Allwood, A. C., Kamber, B. S., Walter, M. R., Burch, I. W., & Kanik, I. (2010). Trace elements record depositional history of an Early Archean stromatolitic carbonate platform. Chemical Geology, 270(1-4), 148-163. https://doi.org/10.1016/j.chemgeo.2009.11.013

Azevedo, C., Jébrak, M., Genna, D., & Pinti, D. L. (2022). Evidence of gold related to Neoarchean alkaline magmatism in the Abitibi greenstone belt (Canada) from mineral parageneses and microscale trace element geochemistry on pyrite. Ore Geology Reviews, 145, 104878. https://doi.org/10.1016/j.oregeorev.2022.104878

Banks, D. A., Yardley, B. W. D., Campbell, A. R., & Jarvis, K. E. (1994). REE composition of an aqueous magmatic fluid : A fluid inclusion study from the Capitan Pluton, New Mexico, U.S.A. Chemical Geology, 113(3-4), 259-272. https://doi.org/10.1016/0009-2541(94)90070-1

Barrett, T. J., & MacLean, W. H. (1999). Volcanic sequences, lithogeochemistry, and hydrothermal alteration in some bimodal volcanic-associated massive sulfide systems. Reviews in Economic Geology, 8, 101-131.

Barrett, T. J., MacLean, W. H., & Årebäck, H. (2005). The Palaeoproterozoic Kristineberg VMS deposit, Skellefte district, northern Sweden. Part II : Chemostratigraphy and alteration. Mineralium Deposita, 40(4), 368-395. https://doi.org/10.1007/s00126-005-0001-2

Barrie, C. T., & Krogh, T. E. (1996). U-Pb zircon geochronology of the Selbaie Cu-Zn-Ag-Au mine, Abitibi Subprovince, Canada. Economic Geology, 91(3), 563-575. https://doi.org/10.2113/gsecongeo.91.3.563

Barton, I. F., Yang, H., & Barton, M. D. (2014). The mineralogy, geochemistry and metallurgy of Cobalt in the rhombohedral carbonates. The Canadian Mineralogist, 52(4), 653-670. https://doi.org/10.3749/canmin.1400006

Bau, M. (1991). Rare-earth element mobility during hydrothermal and metamorphic fluid-rock interaction and the significance of the oxidation state of europium. Chemical Geology, 93(3-4), 219-230. https://doi.org/10.1016/0009-2541(91)90115-8

Bau, M. (1996). Controls on the fractionation of isovalent trace elements in magmatic and aqueous systems : Evidence from Y/Ho, Zr/Hf, and lanthanide tetrad effect. Contributions to Mineralogy and Petrology, 123(3), 323-333. https://doi.org/10.1007/s004100050159

Bau, M., & Dulski, P. (1999). Comparing yttrium and rare earths in hydrothermal fluids from the Mid-Atlantic Ridge : Implications for Y and REE behaviour during near-vent mixing and for the YrHo ratio of Proterozoic seawater. Chemical Geology, 155, 77-90.

Bau, M., & Möller, P. (1992). Rare earth element fractionation in metamorphogenic hydrothermal calcite, magnesite and siderite. Mineralogy and Petrology, 45(3-4), 231-246. https://doi.org/10.1007/BF01163114

Baumgartner, R. J., Van Kranendonk, M. J., Pagès, A., Fiorentini, M. L., Wacey, D., & Ryan, C. (2020). Accumulation of transition metals and metalloids in sulfidized stromatolites of the 3.48 billion–year–old Dresser Formation, Pilbara Craton. Precambrian Research, 337, 105534. https://doi.org/10.1016/j.precamres.2019.105534

Berry, L. G., & Mason, B. (1961). Mineralogy : Concepts, descriptions determinations. Geological Journal, 2(3). https://doi.org/10.1002/gj.3350020315

Bolhar, R., Kamber, B. S., Moorbath, S., Fedo, C. M., & Whitehouse, M. J. (2004). Characterisation of early Archaean chemical sediments by trace element signatures. Earth and Planetary Science Letters, 222(1), 43-60. https://doi.org/10.1016/j.epsl.2004.02.016

Bourcier, W. L., & Barnes, H. L. (1987). Ore Solution Chemistry VII. Stabilities of Chloride and Bisulfide Complexes of Zinc to 350°C. Economic Geology, 82, 1839-1863.

Bradshaw, G. D., Rowins, S. M., Peter, J. M., & Taylor, B. E. (2008). Genesis of the Wolverine Volcanic Sediment-Hosted Massive Sulfide Deposit, Finlayson Lake District, Yukon, Canada : Mineralogical, Mineral Chemical, Fluid Inclusion, and Sulfur Isotope Evidence. Economic Geology, 103(1), 35-60. https://doi.org/10.2113/gsecongeo.103.1.35

Brooks, R. R., Presley, B. J., & Kaplan, I. R. (1968). Trace elements in the interstitial waters of marine sediments. Geochimica et Cosmochimica Acta, 32, 397–414.

Camus, Y., & Vadnais-Leblanc, O. (2018). Rapport Technique NI 43-101 et estimation des ressources, Projet B26, Québec (p. 136) [Unpublished Internal Report].

Conde, C., Tornos, F., Danyushevsky, L. V., & Large, R. (2021). Laser ablation-ICPMS analysis of trace elements in pyrite from the Tharsis massive sulphide deposit, Iberian Pyrite Belt (Spain). Journal of Iberian Geology, 47(1-2), 429-440. https://doi.org/10.1007/s41513-020-00161-w

Cook, N., Ciobanu, C., George, L., Zhu, Z.-Y., Wade, B., & Ehrig, K. (2016). Trace Element Analysis of Minerals in Magmatic-Hydrothermal Ores by Laser Ablation Inductively-Coupled Plasma

Mass Spectrometry : Approaches and Opportunities. Minerals, 6(4), 111. https://doi.org/10.3390/min6040111

Craddock, P. R., Bach, W., Seewald, J. S., Rouxel, O. J., Reeves, E., & Tivey, M. K. (2010). Rare earth element abundances in hydrothermal fluids from the Manus Basin, Papua New Guinea : Indicators of sub-seafloor hydrothermal processes in back-arc basins. Geochimica et Cosmochimica Acta, 74(19), 5494-5513. https://doi.org/10.1016/j.gca.2010.07.003

Davies, J. F., Prevec, S. A., Whitehead, R. E., & Jackson, S. E. (1998). Variations in REE and Sr-isotope chemistry of carbonate gangue, Castellanos Zn–Pb deposit, Cuba. Chemical Geology, 144(1-2), 99-119. https://doi.org/10.1016/S0009-2541(97)00123-X

Debruyne, D., Hulsbosch, N., & Muchez, P. (2016). Unraveling rare earth element signatures in hydrothermal carbonate minerals using a source–sink system. Ore Geology Reviews, 72, 232-252. https://doi.org/10.1016/j.oregeorev.2015.07.022

Deer, W. A., Howie, R. A., & Zussman, J. (1967). Rock-forming minerals: Vol. 5 Non-silicates (5$^e$ éd.).

Deng, X.-H., Wang, J.-B., Pirajno, F., Mao, Q.-G., & Long, L.-L. (2020). A review of Cu-dominant mineral systems in the Kalatag district, East Tianshan, China. Ore Geology Reviews, 117, 103284. https://doi.org/10.1016/j.oregeorev.2019.103284

Denisová, N., & Piercey, S. J. (2023). Evolution of the Hydrothermal System Associated with the ABM Replacement-Style Volcanogenic Massive Sulfide Deposit, Finlayson Lake District, Yukon, Canada. Economic Geology, 118(5), 1055-1083. https://doi.org/10.5382/econgeo.5004

Duan, X., Zeng, Q., Wang, Y., Zhou, L., & Chen, B. (2017). Genesis of the Pb−Zn deposits of the Qingchengzi ore field, eastern Liaoning, China : Constraints from carbonate LA−ICPMS trace element analysis and C–O–S–Pb isotopes. Ore Geology Reviews, 89, 752-771. https://doi.org/10.1016/j.oregeorev.2017.07.012

Duran, C. J., Dubé-Loubert, H., Pagé, P., Barnes, S.-J., Roy, M., Savard, D., Cave, B. J., Arguin, J.-P., & Mansur, E. T. (2019). Applications of trace element chemistry of pyrite and chalcopyrite in glacial sediments to mineral exploration targeting : Example from the Churchill Province, northern Quebec, Canada. Journal of Geochemical Exploration, 196, 105-130.

Eickmann, B., Bach, W., Rosner, M., & Peckmann, J. (2009). Geochemical constraints on the modes of carbonate precipitation in peridotites from the Logatchev Hydrothermal Vent Field and Gakkel Ridge. Chemical Geology, 268(1-2), 97-106. https://doi.org/10.1016/j.chemgeo.2009.08.002

Elderfield, H., & Sholkovitz, E. R. (1987). Rare earth elements in the pore waters of reducing nearshore sediments. Earth and Planetary Science Letters, 82, 280-288.

Eldridge, C. S., Barton, P. B., & Ohmoto, H. (1983). Mineral Textures and Their Bearing on Formation of the Kuroko Orebodies. In H. Ohmoto & B. J. Skinner, The Kuroko and Related Volcanogenic Massive Sulfide Deposits. Society of Economic Geologists. https://doi.org/10.5382/Mono.05.15

Epiard, M., Avard, G., De Moor, J. M., Martínez Cruz, M., Barrantes Castillo, G., & Bakkar, H. (2017). Relationship between Diffuse $CO_2$ Degassing and Volcanic Activity. Case Study of the Poás, Irazú, and Turrialba Volcanoes, Costa Rica. Frontiers in Earth Science, 5, 71. https://doi.org/10.3389/feart.2017.00071

Etiope, G., Beneduce, P., Calcara, M., Favali, P., Frugoni, F., Schiattarella, M., & Smriglio, G. (1999). Structural pattern and $CO_2$–$CH_4$ degassing of Ustica Island, Southern Tyrrhenian basin. Journal of Volcanology and Geothermal Research, 88(4), 291-304. https://doi.org/10.1016/S0377-0273(99)00010-4

Faure, S. (2012). Réévaluation paléo-environnementale du complexe volcanique de Selbaie et de son  potentiel métallogénique (Projet 2011-08). CONSOREM.

Faure, S., Jébrak, M., & Angelier, J. (1996). Structural evolution of Les Mines Selbaie, Northern Abitibi Belt, Québec, Canada. Exploration and Mining Geology, 5(3), 215-230.

Fayard, Q. (2020). Contrôles volcaniques, hydrothermaux et structuraux sur la nature et la distribution des métaux usuels et précieux dans les zones minéralisées du projet B26, complexe volcanique de Brouillan, Abitibi, Québec [MSc Thesis]. Université du Québec à Chicoutimi.

Fayard, Q., Mercier-Langevin, P., Daigneault, R., Perreault, S., & Wodicka, N. (2020). The B26 Cu-Zn-Ag-Au project, Brouillan volcanic complex, Abitibi greenstone belt, part 2 : Hydrothermal alteration and mineralization (8712; p. 8712). https://doi.org/10.4095/323669

Fayard, Q., Mercier-Langevin, P., Wodicka, N., Daigneault, R., & Perreault, S. (2020). The B26 Cu-Zn-Ag-Au project, Brouillan volcanic complex, Abitibi greenstone belt, part 1 : Geological setting and geochronology (8712; p. 8712). https://doi.org/10.4095/323668

Ford, K., Keating, P., & Thomas, M. D. (2007). Overview of geophysical signatures associated with Canadian ore deposits. In Mineral Deposits of Canada : A synthesis of Major Deposit-Types, District Metallogeny, the Evolution of Geological Provinces and Exploration Methods (p. 939-970).

Franklin, J. M., Gibson, H. L., Jonasson, I. R., & Galley, A. G. (2005). Volcanogenic Massive Sulfide Deposits. In Economic Geology : One Hundredth Anniversary Volume (Society of Economic Geologists, p. 523-560).

Franklin, J. M., Kasarda, J., & Poulsen, K. H. (1975). Petrology and chemistry of the alteration zone of the Mattabi massive sulfide deposit. Economic Geology, 70(1), 63-79. https://doi.org/10.2113/gsecongeo.70.1.63

Frenzel, M., Hirsch, T., & Gutzmer, J. (2016). Gallium, germanium, indium, and other trace and minor elements in sphalerite as a function of deposit type—A meta-analysis. Ore Geology Reviews, 76, 52-78. https://doi.org/10.1016/j.oregeorev.2015.12.017

Gaboury, D., Genna, D., Trottier, J., Bouchard, M., Augustin, J., & Malcolm, K. (2021). The Perron Gold Deposit, Archean Abitibi Belt, Canada : Exceptionally High-Grade Mineralization Related to Higher Gold-Carrying Capacity of Hydrocarbon-Rich Fluids. Minerals, 11(10), 1066. https://doi.org/10.3390/min11101066

Galley, A. G., Hannington, M. D., & Jonasson, I. R. (2007). Volcanogenic massive sulphide deposits. In Mineral Deposits of Canada : A synthesis of Major Deposit-Types, District Metallogeny, the Evolution of Geological Provinces and Exploration Methods (Goodfellow, W.D., p. 141-161).

Genna, D. (2020). Reconnaissance géochimique de la contribution magmatique dans les minéralisations aurifères archéennes (Projet 2019-02). CONSOREM.

Genna, D., & Gaboury, D. (2015). Deciphering the Hydrothermal Evolution of a VMS System by LA-ICP-MS Using Trace Elements in Pyrite : An Example from the Bracemac-McLeod Deposits, Abitibi, Canada, and Implications for Exploration. Economic Geology, 110(8), 2087-2108. https://doi.org/10.2113/econgeo.110.8.2087

Genna, D., & Gaboury, D. (2019). Use of semi-volatile metals as a new vectoring tool for VMS exploration : Example from the Zn-rich McLeod deposit, Abitibi, Canada. Journal of Geochemical Exploration, 207, 106358. https://doi.org/10.1016/j.gexplo.2019.106358

Genna, D., Gaboury, D., & Roy, G. (2014). Evolution of a volcanogenic hydrothermal system recorded by the behavior of LREE and Eu : Case study of the Key Tuffite at Bracemac–McLeod deposits, Matagami, Canada. Ore Geology Reviews, 63, 160-177. https://doi.org/10.1016/j.oregeorev.2014.04.019

George, L. L., Cook, N. J., & Ciobanu, C. L. (2016). Partitioning of trace elements in co-crystallized sphalerite–galena–chalcopyrite hydrothermal ores. Ore Geology Reviews, 77, 97-116. https://doi.org/10.1016/j.oregeorev.2016.02.009

Gibson, H. L., Allen, R. L., Riverin, G., & Lane, T. E. (2007). The VMS model : Advances and Application to Exploration Targeting. In Proceedings of Exploration 07 : Fifth Decennial International Conference on Mineral Exploration (Milkereit, p. 713-730).

Goldfarb, R. J., & Groves, D. I. (2015). Orogenic gold : Common or evolving fluid and metal sources through time. Lithos, 233, 2-26. https://doi.org/10.1016/j.lithos.2015.07.011

González-Jiménez, J. M., Yesares, L., Piña, R., Sáez, R., de Almodóvar, G. R., Nieto, F., & Tenorio, S. (2022). Polymetallic nanoparticles in pyrite from massive and stockwork ores of VMS

deposits of the Iberian Pyrite Belt. Ore Geology Reviews, 145, 104875. https://doi.org/10.1016/j.oregeorev.2022.104875

Grant, H. L. J., Hannington, M. D., Petersen, S., Frische, M., & Fuchs, S. H. (2018). Constraints on the behavior of trace elements in the actively-forming TAG deposit, Mid-Atlantic Ridge, based on LA-ICP-MS analyses of pyrite. Chemical Geology, 498, 45-71. https://doi.org/10.1016/j.chemgeo.2018.08.019

Gregory, D. D., Large, R. R., Halpin, J. A., Baturina, E. L., Lyons, T. W., Wu, S., Danyushevsky, L., Sack, P. J., Chappaz, A., Maslennikov, V. V., & Bull, S. W. (2015). Trace Element Content of Sedimentary Pyrite in Black Shales. Economic Geology, 110(6), 1389-1410. https://doi.org/10.2113/econgeo.110.6.1389

Groves, D. A., Morton, R. L., & Franklin, J. M. (1988). Physical volcanology of the footwall rocks near the Mattabi massive sulphide deposit, Sturgeon Lake, Ontario. Canadian Journal of Earth Sciences, 25(2), 280-291. https://doi.org/10.1139/e88-030

Groves, D. I., Phillips, G. N., Ho, S. E., Houstoun, S. M., & Standing, C. A. (1987). Craton-scale distribution of Archean greenstone gold deposits; predictive capacity of the metamorphic model. Economic Geology, 82(8), 2045-2058. https://doi.org/10.2113/gsecongeo.82.8.2045

Gysi, A. P., & Stefánsson, A. (2012). Mineralogical aspects of $CO_2$ sequestration during hydrothermal basalt alteration—An experimental study at 75 to 250°C and elevated $pCO_2$. Chemical Geology, 306-307, 146-159. https://doi.org/10.1016/j.chemgeo.2012.03.006

Haase, F. J., Vessey, C. J., Sekine, R., Doriean, N. J. C., Welsh, D., Otte, J. A., Hamilton, J., Canfield, D. E., Wang, Y., Lombi, E., & Bennett, W. W. (2024). Reductive sorption of vanadium by iron monosulfide in seawater. Chemical Geology, 121983. https://doi.org/10.1016/j.chemgeo.2024.121983

Haley, B. A., Klinkhammer, G. P., & McManus, J. (2004). Rare earth elements in pore waters of marine sediments. Geochimica et Cosmochimica Acta, 68(6), 1265-1279. https://doi.org/10.1016/j.gca.2003.09.012

Hannington, M. D., Santaguida, F., Kjarsgaard, I. M., & Cathles, L. M. (2003). Regional-scale hydrothermal alteration in the Central Blake River Group, western Abitibi subprovince, Canada : Implications for VMS prospectivity. Mineralium Deposita, 38(4), 393-422. https://doi.org/10.1007/s00126-002-0298-z

Hein, J. R., & Scholl, D. W. (1978). Diagenesis and distribution of late Cenozoic volcanic sediment in the southern Bering Sea. Geological Society of America Bulletin, 89(2), 197. https://doi.org/10.1130/0016-7606(1978)89<197:DADOLC>2.0.CO;2

Herrmann, W., & Hill, A. P. (2001). The Origin of Chlorite-Tremolite-Carbonate Rocks Associated with the Thalanga Volcanic-Hosted Massive Sulfide Deposit, North Queensland, Australia.

Hofmann, H. J., & Masson, M. (1994). Archean stromatolites from Abitibi greenstone belt, Quebec, Canada. Geological Society of America Bulletin, 106(3), 424-429. https://doi.org/10.1130/0016-7606(1994)106<0424:ASFAGB>2.3.CO;2

Huston, D. L., Sie, S. H., Suter, G. F., Cooke, D. R., & Both, R. A. (1995). Trace elements in sulfide minerals from eastern Australian volcanic-hosted massive sulfide deposits; Part I, Proton microprobe analyses of pyrite, chalcopyrite, and sphalerite, and Part II, Selenium levels in pyrite; comparison with delta 34 S values and implications for the source of sulfur in volcanogenic hydrothermal systems. Economic Geology, 90(5), 1167-1196. https://doi.org/10.2113/gsecongeo.90.5.1167

Ishikawa Y., Sawagushi T., Iwaya S., & Horiuchi M. (1976). Delineation of prospecting targets for Kuroko deposits based on modes of volcanism of underlying dacite and alteration halos. Mining Geology, 26, 105-117. https://doi.org/10.11456/shigenchishitsu1951.26.105

Kamber, B. S., Bolhar, R., & Webb, G. E. (2004). Geochemistry of late Archaean stromatolites from Zimbabwe : Evidence for microbial life in restricted epicontinental seas. Precambrian Research, 132(4), 379-399. https://doi.org/10.1016/j.precamres.2004.03.006

Kamber, B. S., Greig, A., & Collerson, K. D. (2005). A new estimate for the composition of weathered young upper continental crust from alluvial sediments, Queensland, Australia. Geochimica et Cosmochimica Acta, 69(4), 1041-1058. https://doi.org/10.1016/j.gca.2004.08.020

Kendrick, M. A., Plümper, O., Zhao, J.-X., Feng, Y., Defliese, W. F., Müller, I. A., & Ziegler, M. (2022). Exhumation and carbonation of the Atlantis Bank core complex constrained by in situ U-Pb dating and Δ47 thermometry of calcite veins, SW Indian Ridge. *Earth and Planetary Science Letters*, *584*, 117474. https://doi.org/10.1016/j.epsl.2022.117474

Keith, M., Häckel, F., Haase, K. M., Schwarz-Schampera, U., & Klemd, R. (2016). Trace element systematics of pyrite from submarine hydrothermal vents. Ore Geology Reviews, 72, 728-745. https://doi.org/10.1016/j.oregeorev.2015.07.012

Khelen, A. C., Manikyamba, C., Subramanyam, K. S. V., Santosh, M., Ganguly, S., Kalpana, M. S., & Subba Rao, D. V. (2019). Archean seawater composition and depositional environment – Geochemical and isotopic signatures from the stromatolitic carbonates of Dharwar Craton, India. Precambrian Research, 330, 35-57. https://doi.org/10.1016/j.precamres.2019.04.020

Kim, J.-H., Torres, M. E., Haley, B. A., Kastner, M., Pohlman, J. W., Riedel, M., & Lee, Y.-J. (2012). The effect of diagenesis and fluid migration on rare earth element distribution in pore fluids of the northern Cascadia accretionary margin. Chemical Geology, 291, 152-165. https://doi.org/10.1016/j.chemgeo.2011.10.010

Klinkhammer, G. P., Elderfield, H., Edmond, J. M., & Mitra, A. (1994). Geochemical implications of rare earth element patterns in hydrothermal fluids from mid-ocean ridges. Geochimica et Cosmochimica Acta, 58(23), 5105-5113. https://doi.org/10.1016/0016-7037(94)90297-6

Kontak, D. J., & Jackson, S. (1995). Laser-Ablation ICP-MS micro-analysis of calcite cement from a Mississippi-Valley-Type Zn-Pb deposit, Nova Scotia : Dramatic variability in REE content on macro and micro-scales. The Canadian Mineralogist, 33, 445-467.

Koopman, E. R., Hannington, M. D., Santaguida, F., & Cameron, B. I. (1999). Petrology and Geochemistry of Proximal Hydrothermal Alteration in the Mine Rhyolite at Kidd Creek*. In The Giant Kidd Creek Volcanogenic Massive Sulfide Deposit, Western Abitibi Subprovince, Canada. Society of Economic Geologists. https://doi.org/10.5382/Mono.10.09

Krushnisky, A., Mercier-Langevin, P., Ross, P.-S., Goutier, J., McNicoll, V., Moore, L., Monecke, T., Jackson, S. E., Yang, Z., Petts, D. C., & Pilote, C. (2023). Geology and Controls on Gold Enrichment at the Horne 5 Deposit and Implications for the Architecture of the Gold-Rich Horne Volcanogenic Massive Sulfide Complex, Abitibi Greenstone Belt, Canada. Economic Geology, 118(2), 285-318. https://doi.org/10.5382/econgeo.4978

Kumar, A., Shrivastava, J. P., & Pathak, V. (2017). Mineral carbonation reactions under water-saturated, hydrothermal-like conditions and numerical simulations of $CO_2$ sequestration in tholeiitic basalt of the Eastern Deccan Volcanic Province, India. Applied Geochemistry, 84, 87-104. https://doi.org/10.1016/j.apgeochem.2017.05.021

Lacroix, S. (1994). Géologie de la partie Ouest du sillon Harricana-Turgeon, Abitibi (MB 94-54; p. 29). Ministère des Ressources naturelles - Québec.

Lafrance, B. (2003). Reconstruction d'un environnement de sulfures massifs volcanogènes déformé : Exemple archéen de Normétal, Abitibi [PhD Thesis]. Université du Québec à Chicoutimi.

Lafrance, B. (2008). Carbonatation phase 3 : Caractérisation de la carbonatation en environnements volcanogène et orogénique (Projet 2008-08). CONSOREM.

Lafrance, B., Mueller, W. U., Daigneault, R., & Dupras, N. (2000). Evolution of a submerged composite arc volcano : Volcanology and geochemistry of the Normétal volcanic complex, Abitibi greenstone belt, Québec, Canada. Precambrian Research, 101(2-4), 277-311. https://doi.org/10.1016/S0301-9268(99)00092-3

Large, R. R. (1992). Australian volcanic-hosted massive sulfide deposits; features, styles, and genetic models. Economic Geology, 87(3), 471-510. https://doi.org/10.2113/gsecongeo.87.3.471

Large, R. R., Allen, R. L., Blake, M. D., & Herrmann, W. (2001). Hydrothermal Alteration and Volatile Element Halos for the Rosebery K Lens Volcanic-Hosted Massive Sulfide Deposit, Western Tasmania. Economic Geology, 96, 1055-1072.

Large, R. R., Maslennikov, V. V., Robert, F., Danyushevsky, L. V., & Chang, Z. (2007). Multistage Sedimentary and Metamorphic Origin of Pyrite and Gold in the Giant Sukhoi Log Deposit, Lena Gold Province, Russia. Economic Geology, 102(7), 1233-1267. https://doi.org/10.2113/gsecongeo.102.7.1233

Large, R. R., Mcphie, J., Gemmell, J. B., Herrmann, W., & Davidson, G. J. (2001). The Spectrum of Ore Deposit Types, Volcanic Environments, Alteration Halos, and Related Exploration Vectors in Submarine Volcanic Successions : Some Examples from Australia. Economic Geology, 96, 913-938.

Larson, J. E., & Hutchinson, R. W. (1993). The Selbaie Zn-Cu-Ag deposits, Quebec, Canada; an example of evolution from subaqueous to subaerial volcanism and mineralization in an Archean caldera environment. Economic Geology, 88(6), 1460-1482. https://doi.org/10.2113/gsecongeo.88.6.1460

Layton-Matthews, D., Peter, J. M., Scott, S. D., & Leybourne, M. I. (2008). Distribution, Mineralogy, and Geochemistry of Selenium in Felsic Volcanic-Hosted Massive Sulfide Deposits of the Finlayson Lake District, Yukon Territory, Canada. *Economic Geology*, *103*(1), 61–88. https://doi.org/10.2113/gsecongeo.103.1.61

Lewis, A. J., Palmer, M. R., Sturchio, N. C., & Kemp, A. J. (1997). The rare earth element geochemistry of acid-sulphate and acid-sulphate-chloride geothermal systems from Yellowstone National Park, Wyoming, USA. Geochimica et Cosmochimica Acta, 61(4), 695-706. https://doi.org/10.1016/S0016-7037(96)00384-5

Mao, Q., Wang, J., Xiao, W., Windley, B. F., Schulmann, K., Yu, M., Fang, T., & Li, Y. (2019). Mineralization of an intra-oceanic arc in an accretionary orogen : Insights from the Early Silurian Honghai volcanogenic massive sulfide Cu-Zn deposit and associated adakites of the Eastern Tianshan (NW China). GSA Bulletin, 131(5-6), 803-830. https://doi.org/10.1130/B31986.1

Marshall, B., & Gilligan, L. B. (1989). Durchbewegung structure, piercement cusps, and piercement veins in massive sulfide deposits; formation and interpretation. Economic Geology, 84(8), 2311-2319. https://doi.org/10.2113/gsecongeo.84.8.2311

Maslennikov, V. V., Ayupova, N. R., Herrington, R. J., Danyushevskiy, L. V., & Large, R. R. (2012). Ferruginous and manganiferous haloes around massive sulphide deposits of the Urals. Ore Geology Reviews, 47, 5-41. https://doi.org/10.1016/j.oregeorev.2012.03.008

Maslennikov, V. V., Maslennikova, S. P., Large, R. R., & Danyushevsky, L. V. (2009). Study of Trace Element Zonation in Vent Chimneys from the Silurian Yaman-Kasy Volcanic-Hosted Massive Sulfide Deposit (Southern Urals, Russia) Using Laser Ablation-Inductively Coupled Plasma Mass Spectrometry (LA-ICPMS). Economic Geology, 104(8), 1111-1141. https://doi.org/10.2113/gsecongeo.104.8.1111

Maslennikov, V. V., Maslennikova, S. P., Large, R. R., Danyushevsky, L. V., Herrington, R. J., Ayupova, N. R., Zaykov, V. V., Lein, A. Yu., Tseluyko, A. S., Melekestseva, I. Yu., &

Tessalina, S. G. (2017). Chimneys in Paleozoic massive sulfide mounds of the Urals VMS deposits : Mineral and trace element comparison with modern black, grey, white and clear smokers. Ore Geology Reviews, 85, 64-106. https://doi.org/10.1016/j.oregeorev.2016.09.012

Michard, A., & Albarède, F. (1986). The REE content of some hydrothermal fluids. Chemical Geology, 55(1-2), 51-60. https://doi.org/10.1016/0009-2541(86)90127-0

Michard, A., Michard, G., Stüben, D., Stoffers, P., Cheminée, J.-L., & Binard, N. (1993). Submarine thermal springs associated with young volcanoes : The Teahitia vents, Society Islands, Pacific Ocean. Geochimica et Cosmochimica Acta, 57(21-22), 4977-4986. https://doi.org/10.1016/S0016-7037(05)80003-1

Mills, R. A., & Elderfield, H. (1995). Rare earth element geochemistry of hydrothermal deposits from the active TAG Mound, 26°N Mid-Atlantic Ridge. Geochimica et Cosmochimica Acta, 59(17), 3511-3524. https://doi.org/10.1016/0016-7037(95)00224-N

Mitra, A., Elderfield, H., & Greaves, M. J. (1994). Rare earth elements in submarine hydrothermal fluids and plumes from the Mid-Atlantic Ridge. Marine Chemistry, 46(3), 217-235. https://doi.org/10.1016/0304-4203(94)90079-5

Möller, P., Dulski, P., Savascin, Y., & Conrad, M. (2004). Rare earth elements, yttrium and Pb isotope ratios in thermal spring and well waters of West Anatolia, Turkey : A hydrochemical study of their origin. Chemical Geology, 206(1-2), 97-118. https://doi.org/10.1016/j.chemgeo.2004.01.009

Morton, R. L., & Franklin, J. M. (1987). Two-fold classification of Archean volcanic-associated massive sulfide deposits. Economic Geology, 82(4), 1057-1063. https://doi.org/10.2113/gsecongeo.82.4.1057

Mueller, W. U., Stix, J. B., White, J. D. L., Corcoran, P. L., Lafrance, B., & Daigneault, R. (2008). Characterisation of Archean Subaqueous Calderas in Canada : Physical Volcanology, Carbonate-Rich Hydrothermal Alteration and a New Exploration Model. In Caldera Volcanism : Analysis, Modelling and Response (First Edition, Vol. 10, p. 181-232). Elsevier. https://doi.org/10.1016/S1871-644X(07)00005-8

Mueller, W. U., Stix, J., Corcoran, P. L., & Daigneault, R. (2009). Subaqueous calderas in the Archean Abitibi greenstone belt : An overview and new ideas. Ore Geology Reviews, 35(1), 4-46. https://doi.org/10.1016/j.oregeorev.2008.12.003

Nance, W. B., & Taylor, S. R. (1976). Rare earth element patterns and crustal evolution—I. Australian post-Archean sedimentary rocks. Geochimica et Cosmochimica Acta, 40(12), 1539-1551. https://doi.org/10.1016/0016-7037(76)90093-4

Natural Resources Canada. (2022). The Canadian critical minerals strategy, from exploration to recycling: Powering the green and digital economy for Canada and the world. Natural Resources Canada.

Nozaki, Y., Zhang, J., & Amakawa, H. (1997). The fractionation between Y and Ho in the marine environment. Earth and Planetary Science Letters, 148(1-2), 329-340. https://doi.org/10.1016/S0012-821X(97)00034-4

Paton, C., Hellstrom, J., Paul, B., Woodhead, J., & Hergt, J. (2011). Iolite : Freeware for the visualisation and processing of mass spectrometric data. Journal of Analytical Atomic Spectrometry, 26(12), 2508. https://doi.org/10.1039/c1ja10172b

Paul, B., Petrus, J., Savard, D., Woodhead, J., Hergt, J., Greig, A., Paton, C., & Rayner, P. (2023). Time resolved trace element calibration strategies for LA-ICP-MS. Journal of Analytical Atomic Spectrometry. https://doi.org/10.1039/D3JA00037K

Paulick, H., Herrmann, W., & Gemmell, J. B. (2001). Alteration of Felsic Volcanics Hosting the Thalanga Massive Sulfide Deposit (Northern Queensland, Australia) and Geochemical Proximity Indicators to Ore. Economic Geology, 96, 1175-1200.

Piché, M., & Jébrak, M. (2004). Normative minerals and alteration indices developed for mineral exploration. Journal of Geochemical Exploration, 82(1), 59-77. https://doi.org/10.1016/j.gexplo.2003.10.001

Piché, M., & Jébrak, M. (2006). Determination of alteration facies using the normative mineral alteration index : Selbaie Cu–Zn deposit, northern Abitibi greenstone belt, Canada. Canadian Journal of Earth Sciences, 43(12), 1877-1885. https://doi.org/10.1139/e06-097

Pichler, T., & Dix, G. R. (1996). Hydrothermal venting within a coral reef ecosystem, Ambitle Island, Papua New Guinea. Geology, 24(5), 435. https://doi.org/10.1130/0091-7613(1996)024<0435:HVWACR>2.3.CO;2

Pichler, T., & Veizer, J. (2004). The precipitation of aragonite from shallow-water hydrothermal fluids in a coral reef, Tutum Bay, Ambitle Island, Papua New Guinea. Chemical Geology, 207(1-2), 31-45. https://doi.org/10.1016/j.chemgeo.2004.02.002

Planavsky, N., Bekker, A., Rouxel, O. J., Kamber, B., Hofmann, A., Knudsen, A., & Lyons, T. W. (2010). Rare Earth Element and yttrium compositions of Archean and Paleoproterozoic Fe formations revisited : New perspectives on the significance and mechanisms of deposition. Geochimica et Cosmochimica Acta, 74(22), 6387-6405. https://doi.org/10.1016/j.gca.2010.07.021

Raiswell, R., & Plant, J. (1980). The incorporation of trace elements into pyrite during diagenesis of black shales, Yorkshire, England. Economic Geology, 75(5), 684-699. https://doi.org/10.2113/gsecongeo.75.5.684

Reeder, R. J. (1983). Crystal chemistry of the rhombohedral carbonates. In Carbonates : Mineralogy and chemistry (Mineralogical society of America, Vol. 11).

Reich, M., Deditius, A., Chryssoulis, S., Li, J.-W., Ma, C.-Q., Parada, M. A., Barra, F., & Mittermayr, F. (2013). Pyrite as a record of hydrothermal fluid evolution in a porphyry copper system : A SIMS/EMPA trace element study. Geochimica et Cosmochimica Acta, 104, 42-62. https://doi.org/10.1016/j.gca.2012.11.006

Revan, M. K., Genç, Y., Maslennikov, V. V., Maslennikova, S. P., Large, R. R., & Danyushevsky, L. V. (2014). Mineralogy and trace-element geochemistry of sulfide minerals in hydrothermal chimneys from the Upper-Cretaceous VMS deposits of the eastern Pontide orogenic belt (NE Turkey). Ore Geology Reviews, 63, 129-149. https://doi.org/10.1016/j.oregeorev.2014.05.006

Rieger, P., Magnall, J. M., Gleeson, S. A., Oelze, M., Wilke, F. D. H., & Lilly, R. (2022). Differentiating between hydrothermal and diagenetic carbonate using rare earth element and yttrium (REE+Y) geochemistry : A case study from the Paleoproterozoic George Fisher massive sulfide Zn deposit, Mount Isa, Australia. Mineralium Deposita, 57(2), 187-206. https://doi.org/10.1007/s00126-021-01056-1

Rouchon, V., Orberger, B., Hofmann, A., & Pinti, D. L. (2009). Diagenetic Fe-carbonates in Paleoarchean felsic sedimentary rocks (Hooggenoeg Formation, Barberton greenstone belt, South Africa) : Implications for $CO_2$ sequestration and the chemical budget of seawater. Precambrian Research, 172(3-4), 255-278. https://doi.org/10.1016/j.precamres.2009.04.010

Sakellaris, G. A. (2007). Petrology, Geochemistry, Stable and Radiogenic Isotopy of the Guelb Moghrein Iron oxide-Copper-Gold-Cobalt Deposit, Mauritania [PhD Thesis]. RWTH Aachen University.

Savard, D., Bouchard-Boivin, B., Barnes, S., & Garbe-Schönberg, D. (2018). UQAC-FeS: A new series of base metal sulfide quality control reference material for LA-ICP-MS analysis. Proceedings of the 10th International Conference on the Analysis of Geological and Environmental Materials, Sydney, Australia, 8–13.

Savard, D., Dare, S., Bédard, L. P., & Barnes, S. (2023). A New Mapping Protocol for Laser Ablation (with Fast Funnel) Coupled to a Time-of-Flight Mass Spectrometer (LA-FF-ICP-ToF-MS) for the Rapid, Simultaneous Quantification of Multiple Minerals. Geostandards and Geoanalytical Research, 47(2), 243-265. https://doi.org/10.1111/ggr.12482

Schandl, E. S., & Bleeker, W. (1999). Hydrothermal and metamorphic fluids of the Kidd Creek Volcanogenic Massive Sulfide deposit: Preliminary evidence from Fluids inclusions. In The giant Kidd Creek Volcanogenic Massive Sulfide deposit, Western Abitibi Subprovince, Canada (Mark D. Hannington and Tucker Barrie).

Schandl, E. S., & Wicks, F. J. (1993). Carbonate and associated alteration of ultramafic and rhyolitic rocks at the Hemingway Property, Kidd Creek volcanic complex, Timmins, Ontario. Economic Geology, 88(6), 1615-1635. https://doi.org/10.2113/gsecongeo.88.6.1615

Schardt, C., & Large, R. R. (2009). New insights into the genesis of volcanic-hosted massive sulfide deposits on the seafloor from numerical modeling studies. Ore Geology Reviews, 35(3-4), 333-351. https://doi.org/10.1016/j.oregeorev.2008.11.008

Shannon, R. D. (1976). Revised effective ionic radii and systematic studies of interatomic distances in halides and chalcogenides. Acta Crystallographica Section A, 32(5), 751-767. https://doi.org/10.1107/S0567739476001551

Sharman, E. R., Taylor, B. E., Minarik, W. G., Dubé, B., & Wing, B. A. (2015). Sulfur isotope and trace element data from ore sulfides in the Noranda district (Abitibi, Canada) : Implications for volcanogenic massive sulfide deposit genesis. Mineralium Deposita, 50(5), 591-606. https://doi.org/10.1007/s00126-014-0559-7

Shikazono, N., Nakata, M., & Tokuyama, E. (1994). Pyrite with high Mn content from the Nankai Trough formed from subduction-induced cold seepage. Marine Geology, 118(3-4), 303-313. https://doi.org/10.1016/0025-3227(94)90090-6

Sinclair, I. G. L. (1977). Primary dispersion patterns associated with the Detour Zinc-Copper-Silver deposit at Lac Brouillan, Province of Québec, Canada. Journal of Geochemical Exploration, 8, 139-151.

Smrzka, D., Zwicker, J., Bach, W., Feng, D., Himmler, T., Chen, D., & Peckmann, J. (2019). The behavior of trace elements in seawater, sedimentary pore water, and their incorporation into carbonate minerals : A review. Facies, 65(4), 41. https://doi.org/10.1007/s10347-019-0581-4

Soltani Dehnavi, A., McFarlane, C., Lentz, D., McClenaghan, S., & Walker, J. (2019). Chlorite-White Mica Pairs' Composition as a Micro-Chemical Guide to Fingerprint Massive Sulfide Deposits of the Bathurst Mining Camp, Canada. Minerals, 9(2), 125. https://doi.org/10.3390/min9020125

Soltani Dehnavi, A., McFarlane, C. R. M., Lentz, D. R., & Walker, J. A. (2018). Assessment of pyrite composition by LA-ICP-MS techniques from massive sulfide deposits of the Bathurst Mining Camp, Canada : From textural and chemical evolution to its application as a vectoring tool for the exploration of VMS deposits. Ore Geology Reviews, 92, 656-671. https://doi.org/10.1016/j.oregeorev.2017.10.010

Speer, J. A. (1983). Crystal chemistry and phase relations of orthorhombic carbonates. In Carbonates : Mineralogy and chemistry (Mineralogical society of America, Vol. 11).

Spitz, G., & Darling, R. (1978). Major and minor element lithogeochemical anomalies surrounding the Louvem copper deposit, Val d'Or, Quebec. Canadian Journal of Earth Sciences, 15(7), 1161-1169. https://doi.org/10.1139/e78-122

Spooner, E. T. C. (1993). Magmatic sulphide/volatile interaction as a mechanism for producing chalcophile element enriched, Archean Au-quartz, epithermal Au-Ag and Au skarn hydrothermal ore fluids. Ore Geology Reviews, 7(5), 359-379. https://doi.org/10.1016/0169-1368(93)90001-F

Steadman, J. A., Large, R. R., Olin, P. H., Danyushevsky, L. V., Meffre, S., Huston, D., Fabris, A., Lisitsin, V., & Wells, T. (2021). Pyrite trace element behavior in magmatic-hydrothermal environments : An LA-ICPMS imaging study. Ore Geology Reviews, 128, 103878. https://doi.org/10.1016/j.oregeorev.2020.103878

Sun, S. -s., & McDonough, W. F. (1989). Chemical and isotopic systematics of oceanic basalts : Implications for mantle composition and processes. Geological Society, London, Special Publications, 42(1), 313-345. https://doi.org/10.1144/GSL.SP.1989.042.01.19

Sverjensky, D. A. (1984). Europium redox equilibria in aqueous solution. Earth and Planetary Science Letters, 67(1), 70-78. https://doi.org/10.1016/0012-821X(84)90039-6

Taner, M. F. (2000). The Geology of the Volcanic-associated Polymetallic (Zn, Cu, Ag and Au) Selbaie Deposits, Abitibi, Quebec, Canada. Exploration and Mining Geology, 9(3-4), 189-214. https://doi.org/10.2113/0090189

Thomas, H. V., Large, R. R., Bull, S. W., Maslennikov, V., Berry, R. F., Fraser, R., Froud, S., & Moye, R. (2011). Pyrite and Pyrrhotite Textures and Composition in Sediments, Laminated Quartz Veins, and Reefs at Bendigo Gold Mine, Australia : Insights for Ore Genesis. Economic Geology, 106(1), 1-31. https://doi.org/10.2113/econgeo.106.1.1

Trépanier, S. (2013). Norme LithoModeleur (Projet 2011-04; p. 101). CONSOREM.

Trépanier, S., Mathieu, L., & Daigneault, R. (2015). CONSONORM_LG : New Normative Minerals and Alteration Indexes for Low-Grade Metamorphic Rocks. Economic Geology, 110(8), 2127-2138. https://doi.org/10.2113/econgeo.110.8.2127

Van Kranendonk, M. J., Webb, G. E., & Kamber, B. S. (2003). Geological and trace element evidence for a marine sedimentary environment of deposition and biogenicity of 3.45 Ga stromatolitic carbonates in the Pilbara Craton, and support for a reducing Archaean ocean. Geobiology, 1(2), 91-108. https://doi.org/10.1046/j.1472-4669.2003.00014.x

Veizer, J. (1983). Trace elements and isotopes in sedimentary carbonates. In Carbonates : Mineralogy and chemistry (Mineralogical society of America, Vol. 11).

Veizer, J., Clayton, R. N., Hlnton, R. W., Von Brunn, V., Mason, T. R., Buck, S. G., & Hoefs, J. (1990). Geochemistry of Precambrian carbonates : 3-shelf seas and non-marine environments of the Archean. Geochimica et Cosmochimica Acta, 54(10), 2717-2729. https://doi.org/10.1016/0016-7037(90)90007-8

Veizer, J., Hoefs, J., Lowe, D. R., & Thurston, P. C. (1989). Geochemistry of Precambrian carbonates: II. Archean greenstone belts and Archean seawater. Geochimica et Cosmochimica Acta, 53(4), 859-871. https://doi.org/10.1016/0016-7037(89)90031-8

Veizer, J., Hoefs, J., Ridler, R. H., Jensen, L. S., & Lowe, D. R. (1989). Geochemistry of Precambrian carbonates: I. Archean hydrothermal systems. Geochimica et Cosmochimica Acta, 53(4), 845-857. https://doi.org/10.1016/0016-7037(89)90030-6

Wagner, T., Klemd, R., Wenzel, T., & Mattsson, B. (2007). Gold upgrading in metamorphosed massive sulfide ore deposits: Direct evidence from laser-ablation–inductively coupled plasma–mass spectrometry analysis of invisible gold. Geology, 35(9), 775. https://doi.org/10.1130/G23739A.1

Wheat, C. G., Mottl, M. J., & Rudnicki, M. (2002). Trace element and REE composition of a low-temperature ridge-flank hydrothermal spring. Geochimica et Cosmochimica Acta, 66(21), 3693-3705. https://doi.org/10.1016/S0016-7037(02)00894-3

Winchester, J. A., & Floyd, P. A. (1977). Geochemical discrimination of different magma series and their differentiation products using immobile elements. Chemical Geology, 20, 325-343. https://doi.org/10.1016/0009-2541(77)90057-2

**ANNEXES**

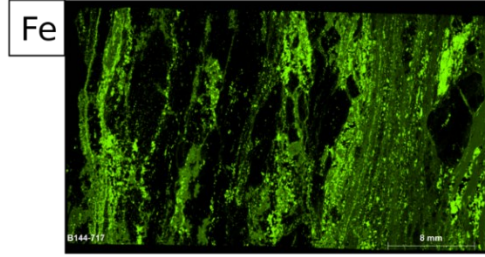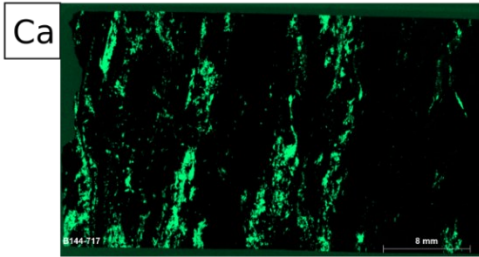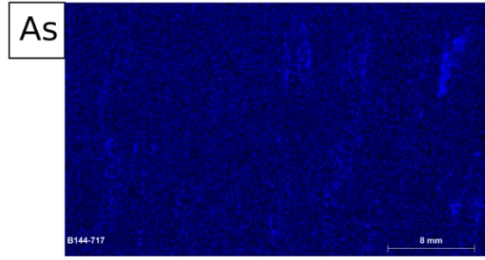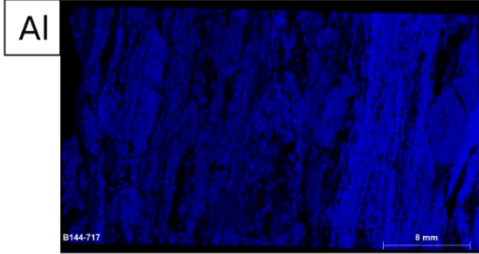**ANNEX 1:** Map of normative carbonate (ALT_CARBS) in the Selbaie caldera (Faure, 2012). Black lines represent interpreted faults and shear zones
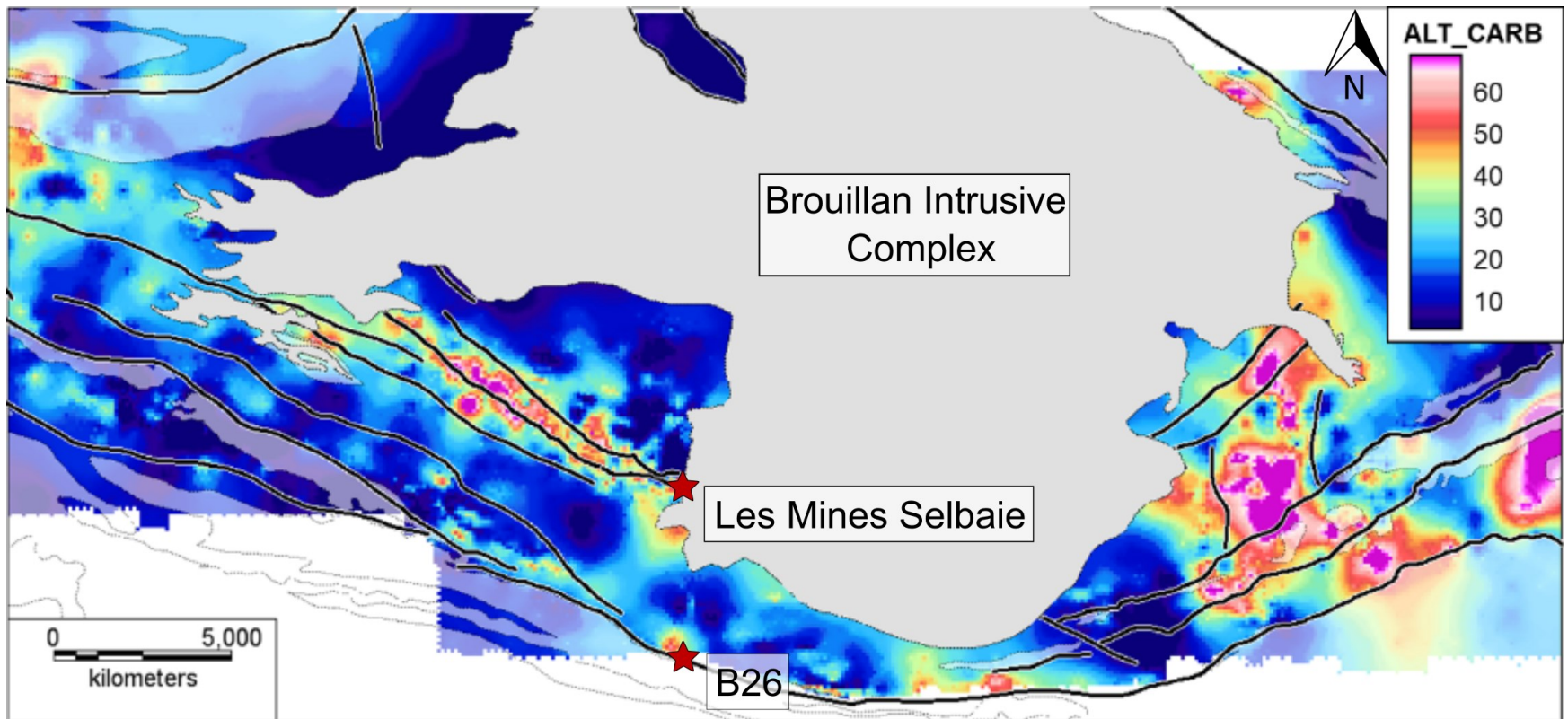
**ANNEX 2:** Micro-XRF maps of selected trace elements for 3 polished thin sections. A. 259-462.3A; B. B144-790.3 ; C. B236-1308

B

**C**

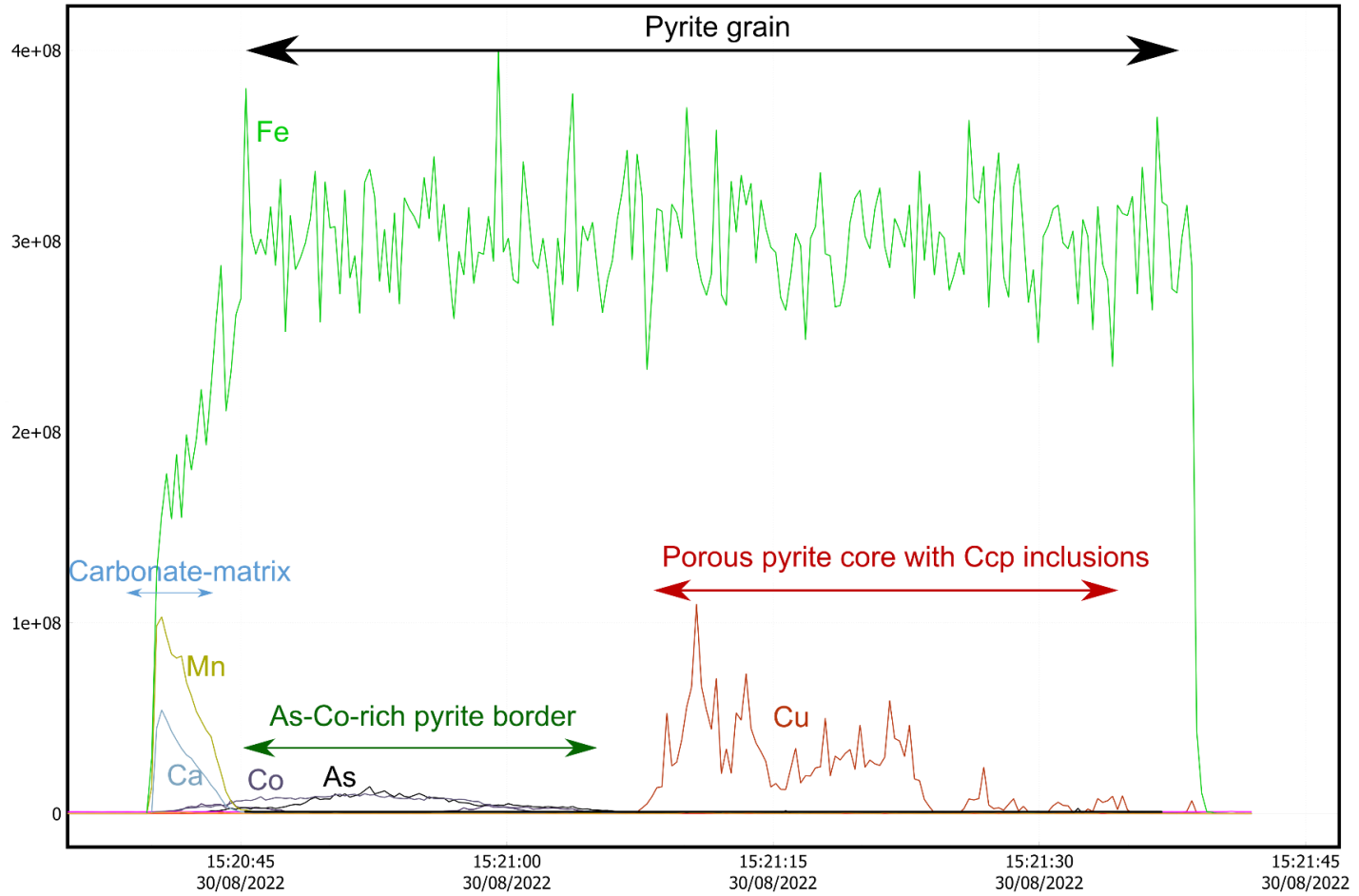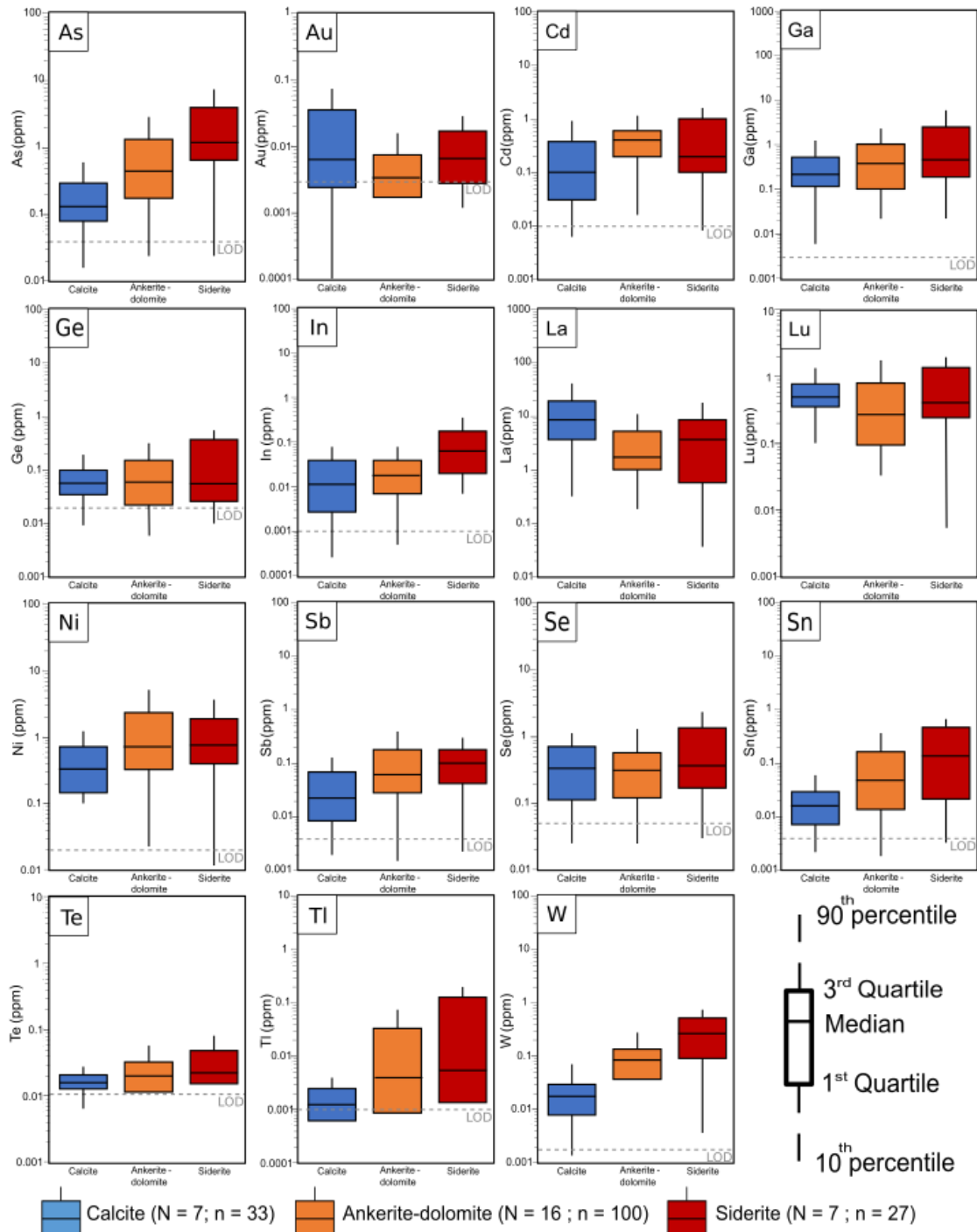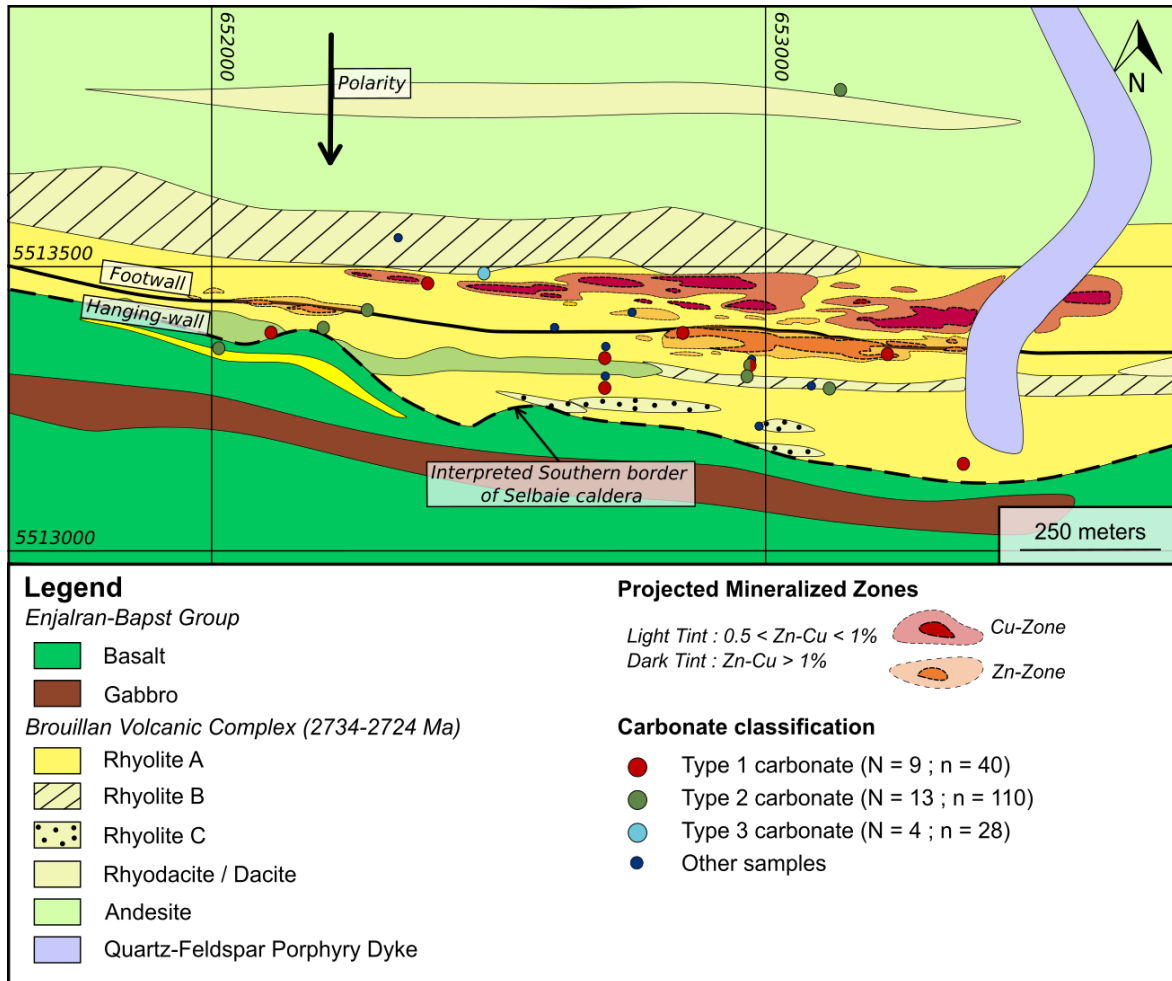Al · As · Ca · Fe · K · Mg · Mn · P · S · Si · Ti · Zn
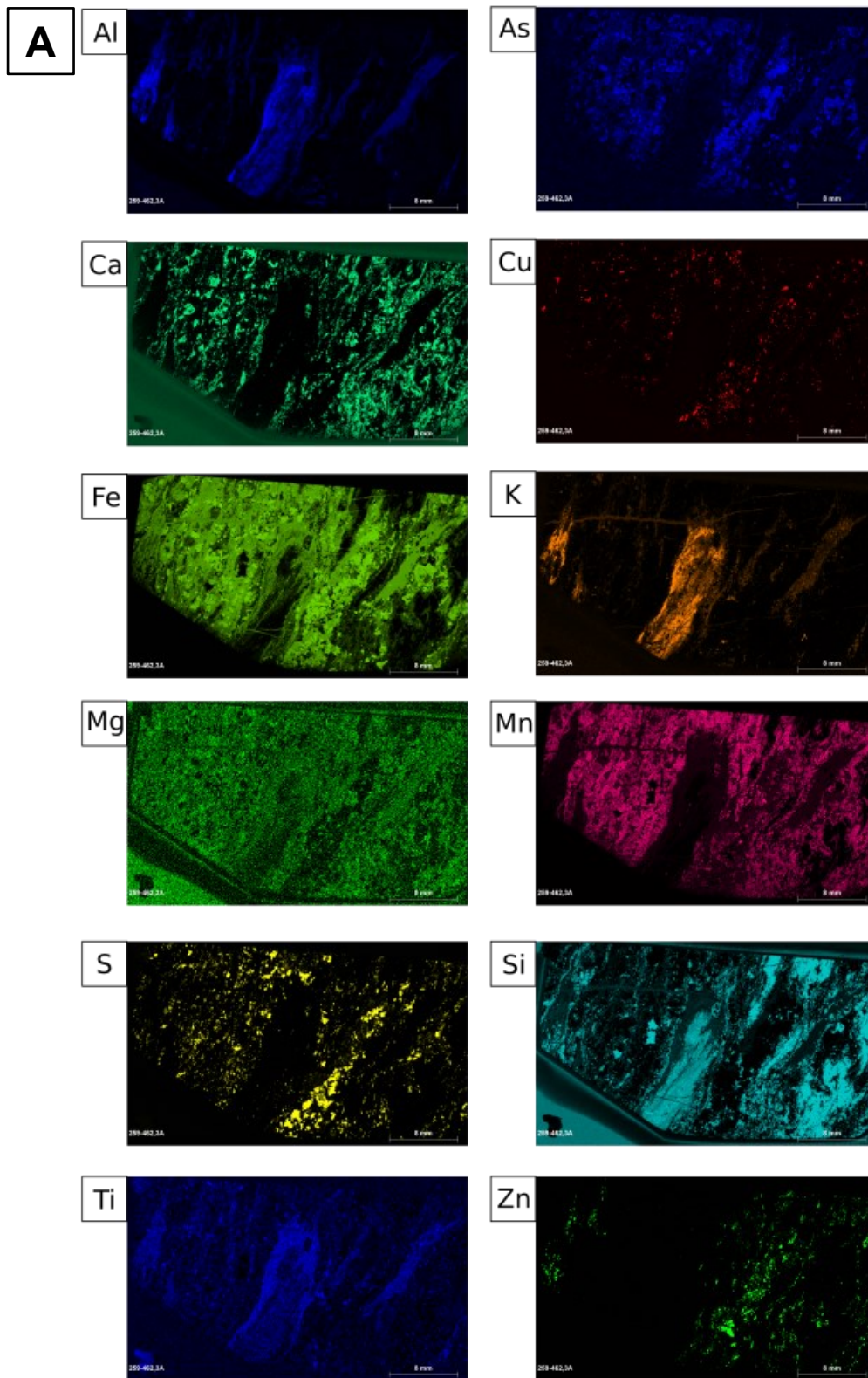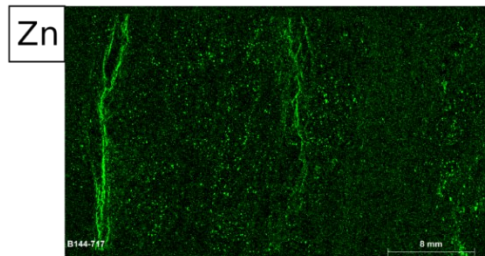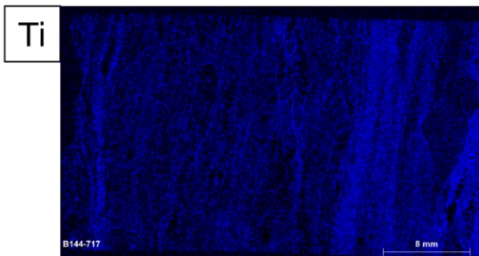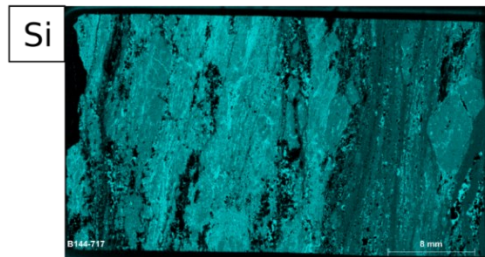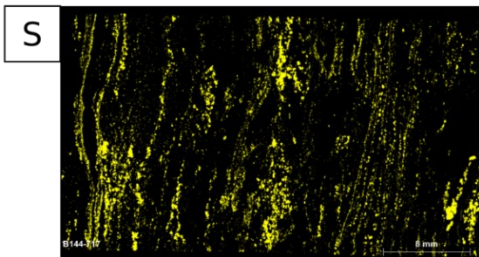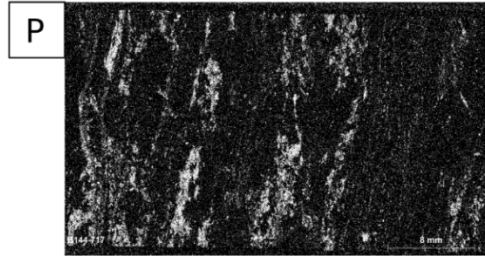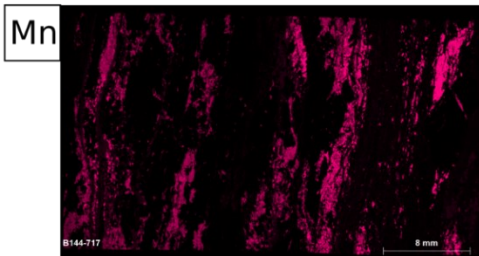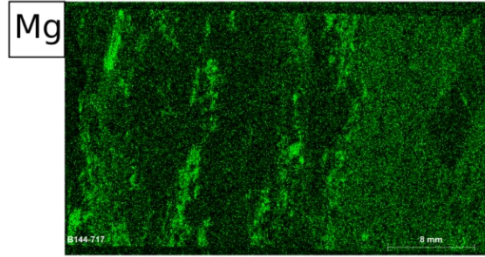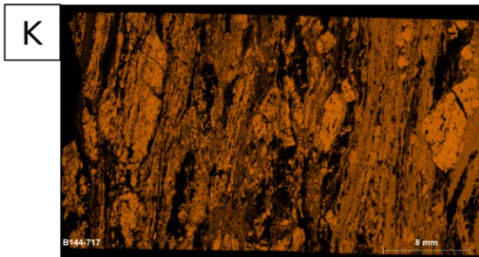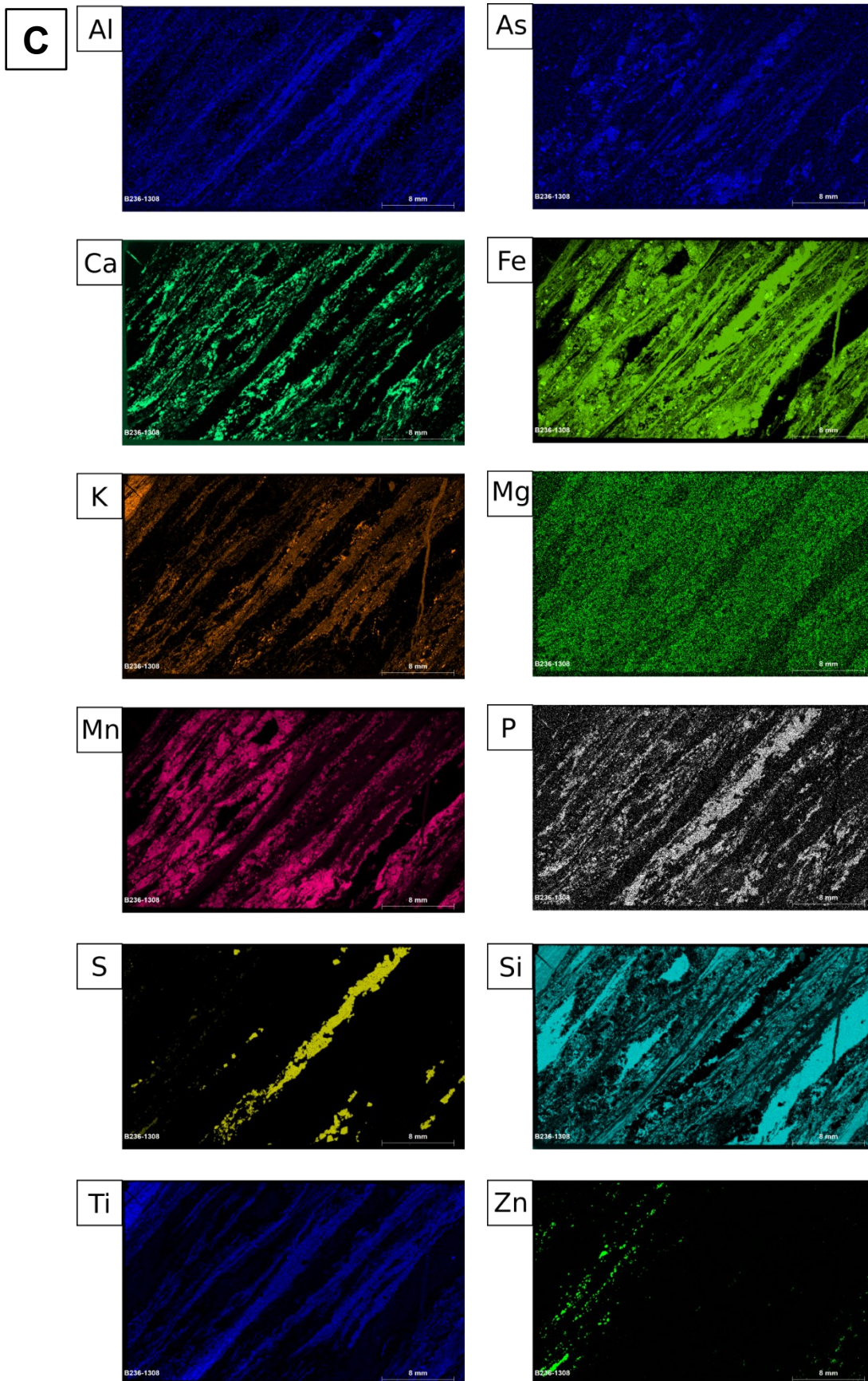
**ANNEX 3:** Time-resolved signal of LA-ICP-MS analysis of a zoned pyrite with a porous core and a clear Co-As-rich border (Pyrite B288-250.1-01)

**ANNEX 4:** Box plot diagrams of trace elements in carbonates (supplementary elements to Figure 4.5)

**ANNEX 5:** Geological map of the B26 transect showing the spatial distribution of each type of carbonate. Geological map modified from Fayard (2020)



**Legend**

*Enjalran-Bapst Group*

- Basalt
- Gabbro

*Brouillan Volcanic Complex (2734-2724 Ma)*

- Rhyolite A
- Rhyolite B
- Rhyolite C
- Rhyodacite / Dacite
- Andesite
- Quartz-Feldspar Porphyry Dyke

**Projected Mineralized Zones**

*Light Tint : 0.5 < Zn-Cu < 1%*
*Dark Tint : Zn-Cu > 1%*

- Cu-Zone
- Zn-Zone

**Carbonate classification**

- Type 1 carbonate (N = 9 ; n = 40)
- Type 2 carbonate (N = 13 ; n = 110)
- Type 3 carbonate (N = 4 ; n = 28)
- Other samples

**ANNEX 6:** Geological map of the B26 transect showing the spatial distribution of each type of pyrite. Geological map modified from Fayard (2020)



## Legend

*Enjalran-Bapst Group*

- **Basalt**
- **Gabbro**

*Brouillan Volcanic Complex (2734-2724 Ma)*

- **Rhyolite A**
- **Rhyolite B**
- **Rhyolite C**
- **Rhyodacite / Dacite**
- **Andesite**
- **Quartz-Feldspar Porphyry Dyke**

## Projected Mineralized Zones

*Light Tint : 0.5 < Zn-Cu < 1%*
*Dark Tint : Zn-Cu > 1%*

- Cu-Zone
- Zn-Zone

## Pyrite classification

- Pyrites from the mineralization (N = 9 ; n = 53)
- Pyrites from the proximal carbonate halo (N = 7 ; n = 43)
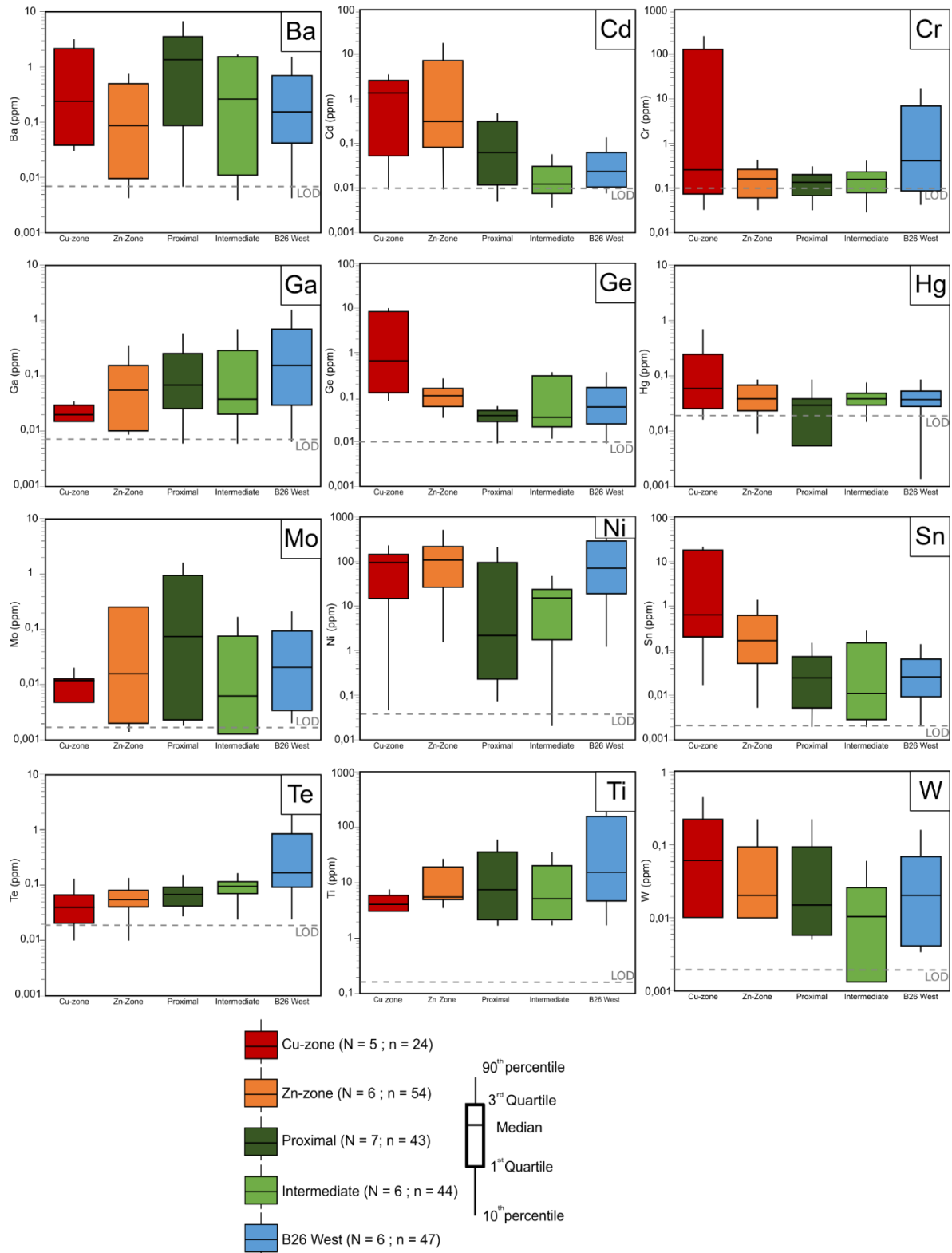- Pyrites from the intermediate carbonate halo (N = 6 ; n = 44)
- Other samples

**ANNEX 7:** Box plot diagrams of trace elements in pyrite (supplementary elements to Figure 4.8)



Legend:
- Cu-zone (N = 5 ; n = 24)
- Zn-zone (N = 6 ; n = 54)
- Proximal (N = 7; n = 43)
- Intermediate (N = 6 ; n = 44)
- B26 West (N = 6 ; n = 47)

90th percentile
3rd Quartile
Median
1st Quartile
10th percentile

**ANNEX 8:** Evolution of the Se, Ag and As content in whole-rock geochemistry with distance to B26 mineralization. Limit of detection (LOD) is represented by a light gray dash line; if it is not present, the detection limit is below the limits of the diagram.